

THE NIELS BOHR INSTITUTE

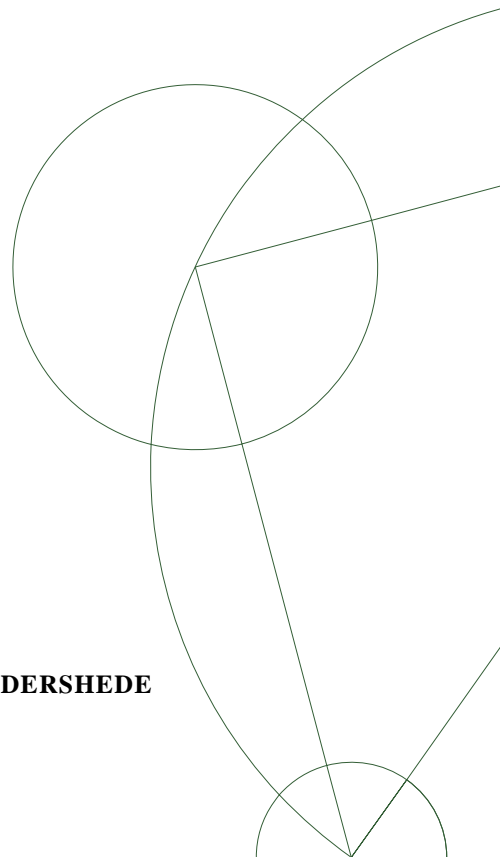
FACULTY OF SCIENCE
UNIVERSITY OF COPENHAGEN



PhD thesis

LISELOTTE JAUFFRED

**OPTICAL MANIPULATION AND BIOLOGICAL
APPLICATIONS OF QUANTUM DOTS**



ACADEMIC SUPERVISOR : LENE ODDERSHEDE

Submitted: 23th of April 2010

Abstract

This thesis is concerned with optical manipulation of small particles. This includes dielectric spheres in a standing wave evanescent field and, in particular, quantum dots in the optical trap. The forces acting on the small particles in the optical fields are characterized and quantized. Ultimately to use the particles as force transducers on the pN scale. This is desirable for many biophysical applications.

Calculations of optical forces in a plane wave evanescent field are presented. The forces acting on a sphere in the field is decomposed and the gradient force and the scattering force are calculated individually. The trapping potential and trapping strength is considered and a possible comparison to the observed diffusive behavior of a bead in the field is sketched.

Optical trapping of colloidal quantum dots is reported. The properties of quantum dots as force transducers are characterized. We measure the trapping strength of different sizes of quantum dots and estimate the polarizabilities. Furthermore, we report two-photon excitation in the optical trap.

This thesis is also concerned with the traffic of RNA polymerases on the DNA and how this regulates the gene in living cell. The *lac* operon is a well-known system of genes where one transcription factor regulates two feedback loops. In addition to this, the transcription factor binds to a site on its own gene and hinders the RNA polymerase to produce a transcript. A model to explore the consequences of auto-regulation is presented and the cells response to different environments is investigated.

Finally, another application of quantum dots is considered. The use of quantum dots for tracking individual polymerases on the DNA. This includes the attachment of a quantum dot to an RNA polymerase and the activity of this complex is measured. Furthermore, different appropriate geometries to follow this complex is discussed. In relation to this, we present the use of quantum dots as tracker particles in a geometry where DNA is anchored to the surface.

Preface

The research of this work was carried out in the Optical Tweezers laboratory in the Bio-Complexity group at the Niels Bohr Institute. I was enrolled as a Ph.D. student from September 2006 to April 2010; including a maternity leave. The work was supervised by Associate Professor Lene Oddershede.

During my work I have benefited from the knowledge and guidance of several people. Firstly, I would like to thank Lene Oddershede; she always took active part in advising as well as supporting me. During my work she always encouraged me to try more and aim higher.

Secondly, I would like to thank Andrew Richardson and Nader Reihani for experimental guidance. As I would like to thank Sandeep Krishna and Szabolcs Semsey to let me participate in the work on the model of the lac operon. I enjoyed it.

Thirdly, I would like to thank Szabolcs Semsey for his patience when I was disturbing his laboratory at ELTE, Budapest and for sharing some of his knowledge on microbiology with me. In addition to this, I should mention Marit Sletmoen and Mette Eriksen for all the time they invested in trying to attach quantum dots to polymerases.

I would also like to thank Alexander Rorhback for hosting me at IMTEK, Freiburg. I will always keep a good memory of my time in his group.

In addition, I would like to thank the Optical Tweezers Group, in particular Fabian Czerwinsky, Andrew Richardson, and Marie Domange for fruitful discussions and pleasant company in the laboratory.

Finally, special thanks goes to Marie Domange and Sandeep Krishna for their patience and cheerful company and, of course, to my little family for being my little family.

List of Publications

Publications in peer-reviewed journals:

Liselotte Jauffred and Lene B. Oddershede: *Two-photon quantum dot excitation during optical trapping*, Nano Letters **10**:1927-1930 (2010).

Liselotte Jauffred, Andrew C. Richardson, and Lene B. Oddershede: *Three-dimensional optical control of individual quantum dots*, Nano Letters **8**:3376-3380 (2008).

Liselotte Jauffred , Thomas Hønger Callisen and Lene Broeng Oddershede: *Visco-elastic membrane tethers extracted from Escherichia coli by optical tweezers*, Biophysical Journal **93**:4068 (2007).

Preprints:

Liselotte Jauffred, Szabolcs Semsey, and Sandeep Krishna: *Auto-regulation in the Lac operon*, in preparation.

Liselotte Jauffred and Lene Oddershede: *Quantum dots as handles for optical manipulation*, Proceeding of SPIE, in preparation.

List of abbreviations

1D	one-dimensional
2D	two-dimensional
3D	three-dimensional
bp	base pair
CW	constant wave
DNA	deoxyribonucleic acid
EC	elongating complex
NA	numerical aperture
QD	quantum dot
RNA	ribonucleic acid
RNAP	RNA polymerase
SDC	sitting-duck complex
SEM	standard error of mean
S/N	signal to noise ratio
STD	standard deviation
SW	standing wave
TEM	transmission electron microscopy
TIRF	total internal reflection

Contents

1	Introduction	1
1.1	Genetic regulation	1
1.2	Polymerase traffic on DNA	5
1.3	Optical manipulation	7
1.4	Quantum dots	9
1.5	Summary	13
2	Auto-regulation in the lac operon	15
2.1	Introduction	15
2.2	Methods	19
2.3	Results	23
2.3.1	Experimental results	23
2.3.2	Theoretical results	24
2.4	Discussion	28
2.5	Conclusion	29
3	Forces in the standing wave evanescent field	31
3.1	Introduction	31
3.2	Standing wave evanescent field	33
3.2.1	Intensity	33
3.2.2	Force decomposition	35
3.2.3	Gradient force	36
3.2.4	Scattering force	38
3.3	Trapping efficiencies and trapping strength	44
3.4	Experiments	47
3.5	Conclusion	50
4	Optical trapping of quantum dots	51
4.1	Introduction	51
4.2	Combining fluorescence microscopy and optical tweezing	52

4.3	Three-dimensional optical control of individual quantum dots	55
4.3.1	Methods	55
4.3.2	Results	56
4.3.3	Discussion	61
4.4	Dependence of trapping efficiency on quantum dot size	61
4.4.1	Methods	63
4.4.2	Results	63
4.4.3	Discussion	65
4.5	Two-photon quantum dot excitation in the optical trap	66
4.5.1	Methods	67
4.5.2	Results	67
4.5.3	Discussion	71
4.6	Conclusion	71
5	RNA polymerase traffic on DNA	73
5.1	Introduction	73
5.2	Simulation of polymerase traffic	77
5.2.1	Methods	79
5.2.2	Results	80
5.2.3	Discussion	81
5.3	Conformations of DNA extended between two beads	82
5.3.1	Methods	82
5.3.2	Results	83
5.3.3	Discussion	85
5.4	Construction of quantum dot labeled polymerases	87
5.4.1	Methods	88
5.4.2	Results	90
5.4.3	Discussion	92
5.5	Tethered particle method with quantum dots	93
5.5.1	Methods	94
5.5.2	Results	95
5.5.3	Discussion	95
5.6	Conclusion	98
6	Summary and outlook	99
6.1	Summary	99
6.2	Outlook	100
A	Evanescent field of a single plane wave	103

B Setup	107
B.1 Simultaneous fluorescence microscopy and optical trapping . .	107
B.2 Things to be aware of when using the EMCCD	109
C Preparation of DNA and T7 polymerase	111
C.1 DNA	111
C.2 <i>In vivo</i> biotinylation of T7 polymerase	114
C.3 <i>In vitro</i> biotinylation of T7 polymerase	118
D Sample preparations	123
D.1 Optical trapping of quantum dots	123
D.2 Stretching DNA	125
D.3 Activity of T7 polymerase attached with quantum dots	126
D.4 Tethered particle method with quantum dots	128

CHAPTER 1

Introduction

In this introductory chapter the genome is presented. Furthermore, I introduce three of the main subjects in the research behind this thesis: Polymerase traffic on DNA, optical manipulation, and last but certainly not least quantum dots.

1.1 Genetic regulation

Gregor Mendel (1822-1884) noticed, from his well-known studies in pea plants, that biological variations are inherited from parent organisms as specific discrete traits. Living organisms inherit traits from their ancestors through genes and, therefore, the gene is the basic unit of heredity. All living things depend on genes and genes hold the information to build and maintain an organism's cells and pass genetic traits to offspring.

The genome

The holder of the genetic code of all proteins is a long chain of deoxyribonucleic acid (DNA). This polynucleotide is often in the form of a double helix. It encodes sequences of amino acid residues used to build up the proteins of a living organism. Chemically, DNA consists of two long polymers with backbones made of sugars and phosphate groups joined by ester bonds. These two strands run in opposite directions to each other and are therefore anti-parallel. Because of this chemical directionality, the ends of single strands of nucleic acid are termed 5' end and a 3' end (the number of C atoms in the ribose). Convention is that upstream is towards the 5' end and downstream is towards the 3' end. Attached to each sugar is one of four types of molecules called nucleobases or nucleotide triphosphates: C (cytosine), T (thymine), A

(adenine), and G (guanine). These nucleotides can only pair as A to T and C to G. It is the sequence of these four bases along the backbone that encodes information. This genetic code specifies the sequences of amino acids within the proteins of the cell.

Replication

DNA is organized into long structures called chromosomes. These chromosomes are duplicated, in a process called DNA replication, e.g., prior to cell division. In this case, a 1:1 copy of the DNA is produced by an enzyme designated DNA polymerase. The DNA polymerase attaches to and cleaves the DNA, reads along the code, and pairs both parental strands to two new strands. In short, during replication $\text{DNA} \rightarrow 2 \times \text{DNA}$. A complicated proof-reading machinery ensures a high perfection of replication. However, errors occur and give rise to, so called, mutations. These mutations drive the evolution.

Transcription

The code is read by copying stretches of DNA into a related nucleic acid, in a process called transcription. This is necessary for protein expression.

The transcription product is the slightly different ribonucleic acid (RNA) where in the nucleotides of RNA the base T is interchanged with the base U (uracil). G can pair with both C and U and RNA has an additional OH group, which makes RNA more flexible than DNA [1]. Moreover, RNA is often found as a single strand. Hence, RNA can form more elaborate structures like hairpins, loops and pseudo-knots [2, 3]. In short, transcription takes care of the first part of the following pathway:



Transcription is much more selective than replication where the entire chromosome often is copied. In contrast, some parts of the DNA strand are never transcribed. Moreover, the error-rate of transcription is much higher than for replication. The penalty for a mistake in transcription is one incomplete protein whereas a replication error causes a gene mutation. Only one strand is needed for transcription. This strand is complementary to the transcription product. RNA is synthesized from the 5' to the 3' end.

RNA polymerase (RNAP) is, like the DNA polymerase, a large enzyme that has the form of a hand holding the DNA in the palm and some cramps to keep it to the DNA. The RNA:DNA hybrid is believed to span over 8-10 bp and here individual nucleotides are synthesized from the 5' end to 3' end of RNA. Therefore, the polymerase is believed to have a channel to enter the nucleotides and one to exit the ready-made RNA.

The transcription is guided by a DNA sequence, termed a promoter, that specifies the beginning of a gene. The speed of the transcription is some tens of bp/s. Furthermore, the transcription can be divided into: initiation, elongation, and termination. This will be described in more detail in section 1.2.

Three nucleotides form a codon that codes for one of the 20 possible amino acids. Because, $4^3 \gg 20$ several codons code for the same amino acid. This is convenient since it adds robustness to the system by lowering the error rate.

Translation

Another large protein, the ribosome, translates codons to amino acids and builds the proteins. The translation speed is 6-22 codons/s and each RNA is translated 1-40 times before degradation [2].

To summarize, the RNAP takes care of the transcription (first part of the pathway), and the ribosome of the translation (second part of the pathway):



All instances of the gene's expression is under regulation of other mechanisms. The gene, the proteins, and all intermediate states can be modified. In other words, decisions are made regarding which proteins should be expressed and to what extent; this is genetic regulation. Some examples of gene regulating mechanisms are chemical and structural modifications of DNA, proteins enhance or repress binding of RNAP to the DNA, proteins binding to the RNA transcript, antisense RNA binding and even some modifications of the newly made proteins occur.

Gene regulation is essential for viruses, prokaryotes, and eukaryotes (including all multi-cellular organisms) to adapt to the environment; allowing the cell to express a specific protein when needed.

Evolution

The society of bacteria plays a large role in Earth's eco-system where human seems to fill out an extremely small part. So we are unimportant periferic creatures in the external world of a prokaryote.

An example of one of these prokaryotes, that outnumber us, is the rod-shaped Gram-negative bacterium *Escherichia coli* (*E. coli*). This is often found in the intestines of animals, e.g., humans. This well-characterized bacterium is an ideal model organism for many purposes. As a consequence, *E. coli* are often genetically modulated to investigate an effect of a certain genetic change, e.g knock-out or insertion of an additional gene. This gives rise

to a sub-group within the specie with unique characteristics that distinguish it from other *E. coli* sub-species. The differences are often detectable only on the molecular level; however, they may result in changes to the physiology, or phenotype, of the bacterium.

New sub-groups of *E. coli* evolve through the natural selection of mutations. However, not all evolution results in an fit phenotype that survives less fit strains. Instead much evolution relies on random genetic drift, where neutral mutations often prevail in small populations by chance. Evolution is a play between the natural selection and genetic drift [4].

The *lac* operon is a well known example of a genetic regulating mechanism. It consists of three structural genes all associated with the sugar metabolism of the *E. coli* bacterium. It is a two-pathways system that controls the metabolism of lactose when there is no glucose available. This enables the bacterium to shift easily between metabolism of glucose and of lactose.

Errors in information transfer from DNA over RNA to proteins are inevitable. As mentioned above errors occurring through replication can be fixed to become permanent mutations. In contrast, changes, occurring during RNA transcription, are called transient because the lifetime of both the RNA and protein is too short to have heritable consequences. However, in chapter 2 I will present a case where a transient transcription change in the *lac* operon of *E. coli*, causes a heritable phenotypic change within genetically identical cells in the same environment.

1.2 Polymerase traffic on DNA

The attractive interaction between DNA and proteins is both electrostatic and entropic; whereas the interaction changes the number of possible configurations of the DNA. For transcription to start the RNAP binds to the DNA. This binding strength, reflected in the binding energies, is very important for the initiation of transcription. Furthermore, proteins or other biomolecules either inhibit or recruit RNAPs to bind at the promoter site. All these elements, together with conformational changes of the DNA, regulates when and how often an RNAP can initiate transcription along the DNA.

During elongation accumulation of RNAPs can cause tandem formations of RNAPs and even collisions. On the terminator site, the binding strength of the DNA all of a sudden weakens enough to make the RNAP disengage from the DNA. So all in all, the RNAP shall balance two things: The stable binding to the DNA to transcribe the whole gene, and the ability to disengage rather fast at the terminations site.

Considering the DNA as a protein highway the traffickers are the RNAPs trying to, first of all, get into the highway and then to find its way around the different obstacles, e.g., road-blocking regulating proteins and other traffickers, before it gets off at the right exit sequence. A ride along this highway will include, among others, the elements described in this section.

Binding and initiation

The RNAP seeks for promoters, or a highway entry, on the DNA by sliding and jumping along the DNA until it reaches a sequence that is energetically favorable for attachment. This sequence can be blocked by a repressor protein or another RNAP that disables attachments. However, a recruiting protein can also happen to be placed upstream from the promoter to further encourage the RNAP to attach by lowering the binding energy. After the attachment to the promoter site the RNAP:DNA complex forms a closed complex. This is a reversible process and the RNAP can easily detach. In case the RNAP stays bound to the DNA, an open complex is formed by use of the binding energy. In an open complex the DNA is melted; i.e., unwinding of about 12-18 bp of double stranded DNA to form an open bubble. This is necessary for RNAP to initiate transcription [5, 6, 7, 8, 9, 10].

Elongation, backtracking, pauses, and arrests

Elongation involves moving with bp steps away from the promoter while the new RNA strand pairs temporarily with the DNA template at a regime of about 8 bp. Then the RNA peels of and the DNA duplex is reformed [11, 12, 13, 14].

The RNAP motor is powerful and can exert forces in the range of 15-25 pN [15, 16, 17, 18, 19, 20]. So RNAP moves with single bp steps along the DNA, while transcribing, but in some events it pauses, stalls, and even moves backwards without producing any transcript [13, 21, 22, 23, 24, 25, 26, 27].

As mentioned above, the transcribing RNAP must satisfy opposing constraints: it must form a highly stable elongating complex that can move progressively over distances of several thousand bp and must dissociate short after receiving the signal to terminate.

Termination

The ability of the elongating complex to sustain large force loads on the nascent RNA reflects a very tight binding of the RNA transcript in the DNA:RNAP:RNA complex [14, 28]. This is of importance for termination.

Terminators are situated in the end of the genes before the beginning of other genes, to prevent reading of downstream genes. Transcription termination often occurs at sequences that code for a slippery sequence. In the sense that RNA shears in the RNA:DNA hybrid. Hence, RNA and DNA gets out of register thereby affecting the termination efficiency [28].

Genetic regulation

In this thesis regulating phenomenons on the transcriptional level in *E. coli* will be investigated. In chapter 2 the effect of a protein road-blocking its own gene will be modeled.

Furthermore, the requirements for an experimental setup that allows to follow accumulation of RNAPs on the DNA is discussed in 5. Such a system would be ideal to investigate both the protein dynamics and the regulation aspects of RNAP traffic.

1.3 Optical manipulation

As known from Einstein's theory of special relativity, each light photon carries a momentum p

$$p = \frac{E}{c} = \frac{h}{\lambda} \quad (1.3)$$

where c is the speed of light, h is Planck's constant, and $E = h\nu$ is the energy of a photon with frequency ν and wavelength λ . When a photon interacts with an object, momentum is transferred and the object is pushed forward in the direction of propagation, this is the radiation pressure and it is proportional to the light intensity.

An optical trap is formed by a laser beam that is tightly focused by an objective lens of high numerical aperture (NA). Particles are trapped as a result of the optical force exerted on them [29, 30]. This resulting optical force has traditionally been decomposed into two components: a scattering force in the direction of propagation and a gradient force in the direction of the spatial light gradient. The scattering force tends to push the object along the beam axis and the gradient force to push into the focus of the laser beam. However, this decomposition is only for means of simplicity because the two components result from the very same physics [31]. Optical tweezers manipulate objects with sizes from a few nanometers to several microns. Furthermore, the force exerted by the tweezers on the trapped particle can be measured precisely and is typically in the range from 1 to 200 pN [29, 30, 32].

With a very focused laser the spatial gradient intensity is steep and induces dipoles in the dielectric material of the trapped particle. The gradient force arises from the interaction between the fluctuating dipoles and the inhomogeneous electric field. Hence, the force is proportional to both the ability to polarize the trapped particle and the intensity gradient near the focus [31, 33].

Often the forward scattered laser light is used to register the position of the trapped particle on a quadrant photodiode. The knowledge about the positions together with the equation of motion is used to calibrate the trapping strength of the optical tweezers. This will be explained in more detail in chapter 4 where trapping of a semiconductor crystal, or quantum dot, is reported.

Optical tweezers are a classical tool for measuring the force applied by molecular motors (5-20 pN). For instance, the force exerted by an immobilized RNAP is found through the correspondence to the force, with which it drags a handle bead in the trap (~ 15 pN) [23, 34]. This method can also be used to detect many other transcription occurrences such as RNAP

attachment to DNA, elongation along DNA, pauses and so forth.

Almost all applications rely on the use of handle particles. Firstly, due to laser damage of biological specimens [35, 36]. Secondly, because forces are easier to calculate for a spherical particle of known radius. For this reason, most optical tweezers assays measures forces in *in vitro* systems in liquid media. However, organelles of *in vivo* systems have been trapped [37, 38, 39] and a procedure for calibration in viscoelastic media exists [40].

Another method of optical manipulation is introduced in chapter 3: evanescent optical fields. In chapter 3, forces exerted on small particles (0.1 - 0.5 μm) are calculated to investigate if plastic beads in an evanescent force field can be used as force transducers. This is an alternative way of combining microscopy and optical manipulation.

For all kinds of light microscopy the resolution (measured as a distance in the sample) has a lower limit; given by the Rayleigh criterion [41]:

$$\frac{1.22 \cdot \lambda}{2 \cdot \text{NA}_{obj}} \quad (1.4)$$

where λ is the wavelength of the illuminating light and NA_{obj} is the numerical aperture of the objective. For visual light the resolution limit is ~ 200 nm. Hence, tracker particles, investigated in ordinary bright-field, should be of the size of hundreds of nanometers. This is about ten times the size of a protein like RNAP. Fluorescence microscopy is one way to circumvent this resolution limit. Fluorescence is used to visualize a single molecule, single cells, tissues abundant of a specific molecule, and so forth. In some cases the intensity from auto-fluorescence is enough for imaging. However, in most cases imaging requires the attachment of a fluorescent protein, e.g., green fluorescent protein or a quantum dot. Fluorescence microscopy is an appropriate choice for a high signal to noise ratio when it is desired to track very small bio-molecules. Despite this, the signal from a single fluorophore is often difficult to track and it is of great importance to lower the noise the most possible.

Many approaches aims at combining optical manipulation and fluorescence visualization and this thesis includes work done to approach this synthesis through a semiconductor crystal as described in chapters 4 and 5.

1.4 Quantum dots

Colloidal quantum dots (QDs) are nanosized fluorescent semiconductor crystals [42, 43]. They are bright and photostable with a broad excitation spectrum and a narrow emission spectrum, normally distributed around a specific wavelength. Spectra of the QDs used for this thesis work are shown in figure 1.1.

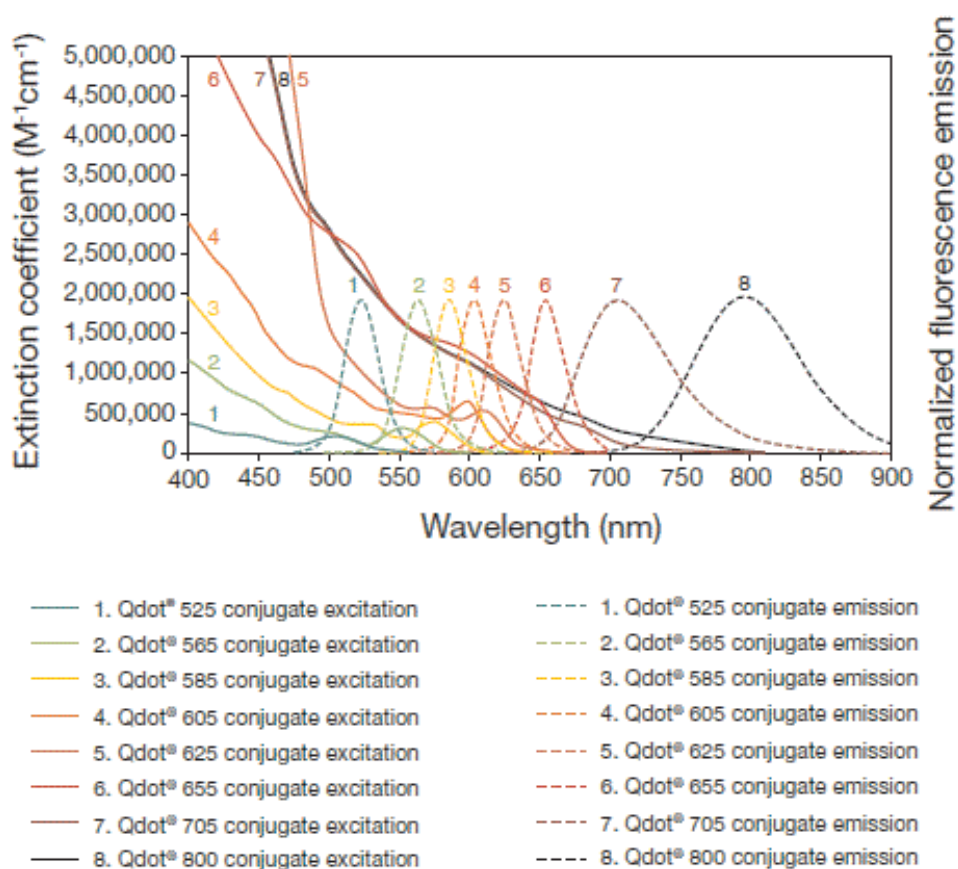


Figure 1.1: Absorption spectra (full line) and emission spectra (punctuated line) for colloidal QDs from Invitrogen. They have a CdSe or CdSeTe cores and a ZnS shell. Information provided from <http://www.invitrogen.com/Qdot>.

Semiconducting crystal

Due to the translational invariance of a crystalline lattice, electrons in a crystal structure are only allowed energies within certain bands between the energy of the ground state and the energy required for an electron to escape the material [44].

In a semiconductor material, ignoring thermal excitations, all electronic states are occupied up to a certain band called the valence band. Above the valence band all states are unoccupied, where the first band is denoted the conduction band. The conduction band and the valence band are separated by a forbidden region, termed the energy bandgap. Hence, it is the energy required to free an outer shell electron from its orbit around the nucleus to become a mobile charge carrier within the material. This is the electron-hole pair excitation. The bandgap between the valence band and the conduction band is what defines the material to be either a conductor (no bandgap), a semiconductor (bandgap $< 3\text{-}4\text{ eV}$), and an insulator ($3\text{-}4\text{ eV} < \text{bandgap}$).

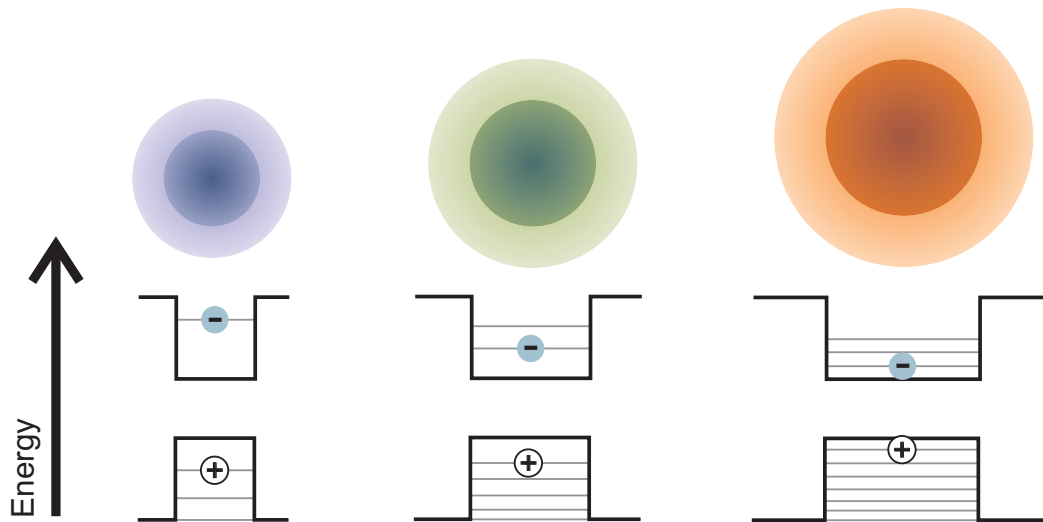


Figure 1.2: Cross sections of QDs of three different sizes. The Black line signifies the bandgap of the semiconducting materials and the gray lines are the discrete energy states. Note that the bandgap of the shell always is larger than the bandgap of the core. (-) and (+) are the electron-hole pairs of excited QDs. There are less states for the smaller QD and more energy is needed to excite the QD. Hence, the emitted light have lower wavelengths when the electrons are more confined.

The properties changes when the size of a semiconducting crystal becomes of the order of nanometers. When electron-hole pairs are squeezed into a small volume the repulsion becomes dominant. The energy of electrons in a QD resembles the classical problem of adding particles to a box [44]. Thus,

the energy states are discrete with energies that depends on the size of the confining potential, i.e., smaller potential leads to larger quantized energies. Absorption of photons causes the formation of an electron-hole pair and when they recombine, a photon is emitted. This is sketched in figure 1.2.

The fluorescent blinking of nanocrystal QDs is the result of a bistability between an emitting state where the QD is described as *on* and the non-emitting *off* state [45]. The intermittent fluorescence is believed to be the result of multi-excitation ionization processes. This covers, in short, the case where an excited QD absorbs a second photon and the outcome is a donation of either the electron or the hole to the surroundings. Hence, applying an optical field to the QD makes it radiate again, due to the re-uptake of the charge [42]. The blinking reduces the overall quantum yield; which is the ratio of emitted to absorbed photons. A shell of some mono-layers of another semiconducting material, with a larger bandgap, on the QD core overcomes some of these surface effects [46].

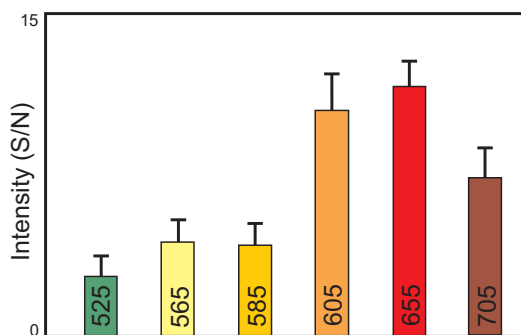


Figure 1.3: Intensity comparison of streptavidin QDs (Invitrogen) adsorbed on glass. Average signal to noise ratio (S/N) of individual QDs. Background subtracted image of 525 nm, 565 nm, 585 nm, 605 nm, 655 nm and 705 nm QDs. Histograms of integrated intensity of representative single 605 nm, 655 nm and 705 nm QDs. Results from Lagerholm and co-workers [47]. For more information of the calculations of S/N, see appendix D.1

Colloidal QDs are often used as fluorophores in the studies of biological systems because of their high quantum yield and large photostability [42, 46, 48, 49]. Among these different applications are single-particle tracking of individual receptors in a cell membrane [50] and in vivo imaging [51]. In this thesis it is shown that individual colloidal QDs can be optically trapped and manipulated in 3D by near-infrared optical tweezers operated at low laser intensities. This makes possible utilizing QDs not only for visualization but also for manipulation. Moreover, quantitative information about the

magnitude of forces applied on a single QD is provided. Furthermore, the polarizability is estimated and two-photon excitation in the optical trap is reported. All this is presented in chapter 4.

Tracker particles

Single molecule methods often rely on the attachment of labels to the molecule of interest, which either scatter light (micron-sized beads) or emit it (QDs or fluorophores), to allow visualization of molecular motion.

It is desirable to use a QD as a fluorescent marker on biological specimen or nano-scale materials. As explained above QDs come in all colors and sizes and, therefore, one must consider which color is appropriate for a specific assay. To this end, Chris Lagerholm and Eva Arnspang Christensen, Memphis, University of Southern Denmark, investigated the intensity and blinking properties of different colors of QDs. This is shown in figure 1.3 and figure 1.4.

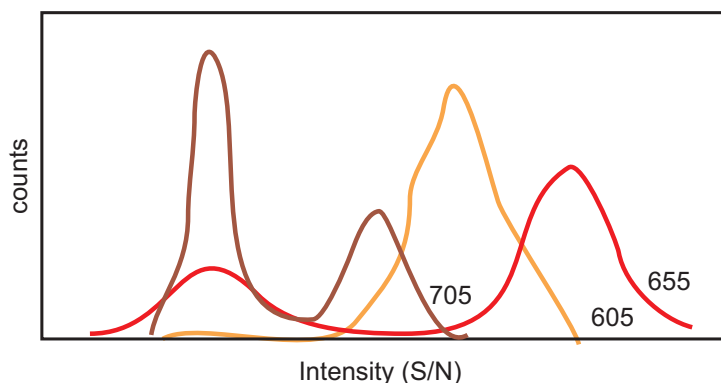


Figure 1.4: Intensity (S/N) comparison of streptavidin QDs (Invitrogen) adsorbed on glass. Histograms of integrated intensity of representative single 605 nm, 655 nm and 705 nm QDs. Results from Lagerholm and co-workers [47]. The intensity distributions show characteristics of emission intermittencies, where the peak at lower intensity corresponds to an *off* state and the other peaks to *on* states. Note that the 605 QD is mostly emitting and, therefore, is seldom in the *off* state.

These results are important for choosing the colloidal QDs appropriate for a specific assay. Together with the results from chapter 4 this provides a good basis knowledge when preparing an assay with QDs as tracker particles and force transducers.

1.5 Summary

Gene expression is summarized in:



In this project only the first part of this pathway will be considered. The transcription is regulated by a large range of very complex mechanism and the sum of these decides to which extension a particular gene is expressed.

The movement and force generation of a single RNAP have often been investigated; either by marking the proteins and following it or by pushing and pulling different parts of the DNA:RNAP:RNA complex. For this purpose, often optical tweezers are used.

3D optical trapping is possible when a force gradient is created by a tightly focused laser beam. The resulting trapping potential depends on the volume and polarizability of the trapped object. The position of the trapped particle can be found by interferometric detection techniques. This knowledge about the positions together with the equations of motion, can be used to calibrate the force exerted by the optical trap on a particle.

A QD is a semiconductor whose excitons are confined in 3D. As a result, they have properties that are between those of bulk semiconductors and those of discrete molecules. The wavelength of the fluorescent light is inversely proportional to the size of the QD. Larger QDs have more energy levels than smaller QDs. This allows the large QD to absorb photons of lower energy, i.e., longer wavelength. Optical trapping of individual QDs provides a perfect force transducer with pN-sensitivity ideal for biophysical experiments.

CHAPTER 2

Auto-regulation in the lac operon

The *lac* operon is a well-known model system for gene regulation. Therefore, there are a large variety of mathematical models of this system. However, none of these models consider the fact that the transcription factor represses itself. Szabolcs Semsey and Sandeep Krishna from Cmol at the Niels Bohr Institute set out to investigate this further and I participated in their inquiry.

2.1 Introduction

Bacteria sense a wide array of signals, e.g. minerals, nutrients, stress signals, etc. Many of these signals are small molecules that induce a response from the cell. Many cellular response systems regulate the flux and concentration of small molecules by controlling transport and metabolism pathways via two feedback loops connected by a common transcription factor. This transcription factor senses the intracellular concentration of the small molecule [52]. In fact, almost half of the transcription factors in *E. coli* are directly regulated by a small molecule [53]. The prototypic example of such systems controls expression of the *lac* operon in *E. coli*.

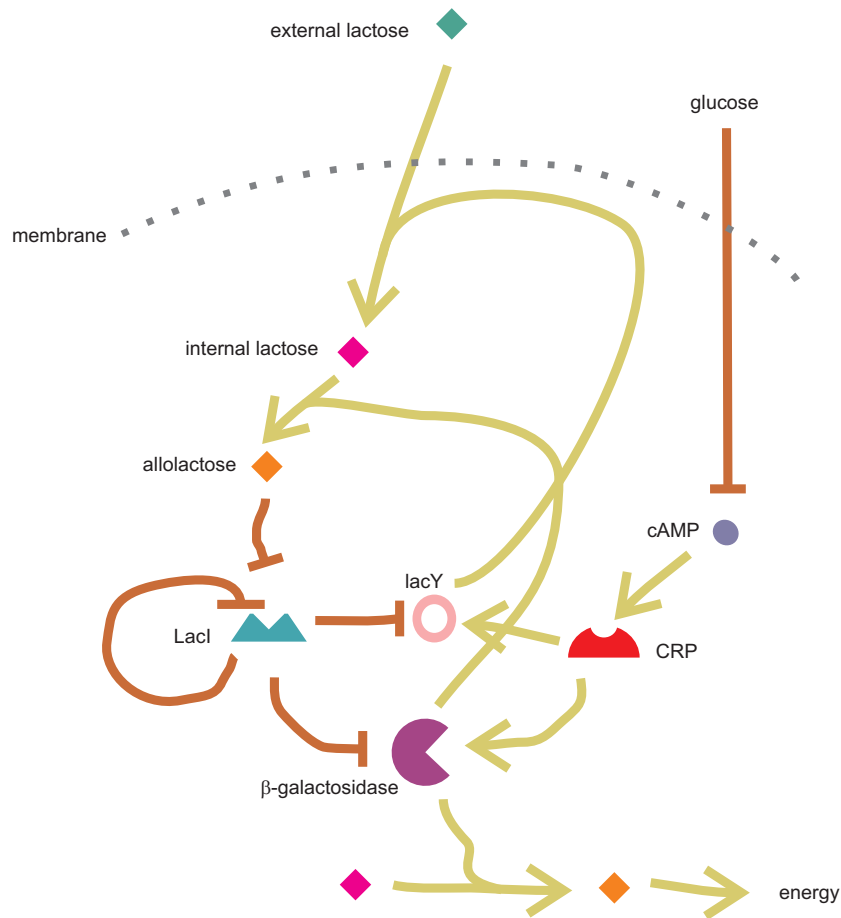


Figure 2.1: A sketch of the input system of the *lac* operon. Arrows denotes activation and barred arrows denotes repression. The right pathway: abundance of external glucose results in a repression of the lactose degrading enzyme β -galactosidase and the membrane protein; the lactose pump. This hinders the transport and metabolism of lactose. The left pathway: external lactose is pumped into the cell and degraded to allolactose, which inactivates LacI. The consequence is that LacI no longer represses β -galactosidase and the pump. Hence, the cell can uptake more lactose and metabolize it. The transcription factor LacI regulates these two loops. In addition, LacI is regulated by the small molecule allolactose which is a degradation product of lactose. Note that the repressor LacI regulates its own production.

The *lac* operon

The *lac* operon consists of three genes, a promoter, a terminator, and operator sites for the two transcription factors, see figure 2.2. The three genes are *lacZ*, *lacY*, and *lacA* where only the first two are of importance for the

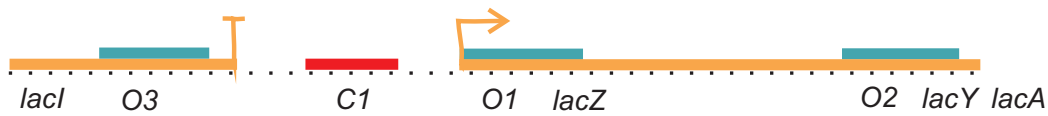


Figure 2.2: Schematic structure of the *lac* genes (*lacZYA*) and control regions for the repressor LacI (*O1, O2, O3*) and the recruiting CAP (*C1*).

pathway: *lacZ* encodes for β -galactosidase (LacZ); an intracellular enzyme that degrades lactose into allolactose, glucose, and galactose. *lacY* encodes β -galactoside permease (LacY), which is a membrane-bound transport protein that pumps external lactose into the cell. The *lacI* gene is present just upstream of the *lac* operon, as shown in figure 2.2. This gene encodes for the transcription factor LacI.

The *lac* operon is a two-pathway system that controls the metabolism of lactose for the *E. coli* bacterium, as sketched in figure 2.1. First, when there is no lactose available LacI blocks *lacZYA* and thereby represses the production of β -galactosidase and the membrane protein LacY. Secondly, when there is very little glucose available the production of β -galactosidase is activated.

Cyclic adenosine monophosphate (cAMP) is a signal molecule whose prevalence is inversely proportional to that of glucose. The cAMP molecule binds to CRP and form the complexes CAP and CAP₂, where the first has high affinity for specific DNA sites [54]. The binding of the CAP protein is strong and recruits RNAPs to the promoter. There is one CAP binding site in the operon; C1 [55].

LacI binds as a tetramer and there are three operator sites where the LacI tetramer can bind and affect transcription [56]. LacI first binds to *O1*, the strongest of the three operator sites, and thereby represses transcription of the *lac* operon but leaves the expression of the *lacI* gene unchanged. The binding of LacI to *O1* increases its probability to bind via DNA looping to *O2* or *O3*, which are much weaker operators. When bound to *O1* and *O2*, transcription of the *lac* operon is repressed while LacI continues to be produced. However, when *O1* and *O3* are bound, not only is the *lac* operon repressed, but the production of LacI is also prevented [57]. This is termed auto-regulation and it covers the case where a gene product regulates its own gene. In most cases auto-regulation inhibits transcription initiation; i.e., hinders the RNAP attachment to the DNA by blocking the promoter [58]. However in the *lac* system, transcription is hindered after initiation. LacI binds to *O3* and creates a road-block that stops the RNAP traffic on its own gene. The result is that transcription of *lacI* occurs but only a truncated transcript is produced [57].

In summary, LacI regulates lactose transport and metabolism pathways simultaneously [59]. In this way, the machinery is ready to metabolize lactose as soon as it is available. Furthermore, it enables the bacterium to shift easily between metabolism of glucose, preferentially, and of lactose. In other words, the genes in the *lac* operon are either *on* (lactose uptake) or *off* (no lactose uptake), see figure 2.3.

While there is experimental evidence for LacI autoregulation [57, 60], this feature of the network is ignored by the available mathematical models [55, 61, 62, 63, 64]. However, previous studies suggested that auto-regulation in regulatory networks can significantly increase the speed of response [65].

In this work we measured the effect of auto-regulation on intracellular LacI concentration and built a model of the lactose utilization system to explore the role of LacI auto-regulation. This is evaluated both deterministically and stochastically. The focus in this chapter will be on the deterministic evaluation and the stochastic evaluation will only be discussed briefly. The results of the model will be compared to the experiments of Szabolcs Semsey and co-workers. We compare the real *lac* system with two hypothetical controls, where LacI is produced at a constant low or at a constant high level. We show that the mechanism of LacI auto-regulation does not increase the speed of response. However, we argue that in a fluctuating lactose environment the auto-regulated system performs better than the constitutive systems.

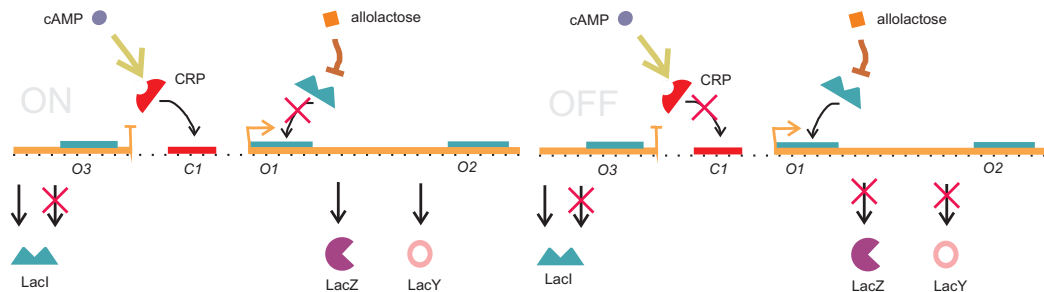


Figure 2.3: To the left is the case where the genes are *on*; i.e., the cell has a lactose uptake. To the right is the case where the genes are *off*; i.e., the cell has no lactose uptake. In both cases the *lacI* gene can either be expressed or auto-regulated dependent on whether the LacI tetramer is bound to *O3* or not. Note that the fact that LacI binds to two operator sites simultaneously, is not covered by this simple drawing.

2.2 Methods

Experimental methods

Szabolcs Semsey did all the experiments that are reported here and in Reference [66] together with Zsolt Csiszovszki from NIH, Bethesda, and János Erdóssy, and Viktor Stéger from ELTE, Budapest. In short, they include studies of the plasmid pSEMJ1 which is constructed as described in detail in Reference [66]. This plasmid allows studies of termination of *lacI* transcription. The mRNA from this plasmid is compared to the wild type *in vitro*. In addition, *in vivo* studies of the LacI tetramer were performed. Here western blotting revealed the levels of LacI both with and without the presence of the sugar IPTG. IPTG is an analog to lactose; it binds to LacI and acts as the small regulator molecule allolactose in figures 2.1 and 2.3. However in contrast, IPTG is not metabolized by β -galactosidase as lactose is. Furthermore, IPTG penetrates the cell more easily than lactose. More details on these assays are found in [66].

Mathematical model

This model of auto-regulation in the *lac* operon was developed by Sandeep Krishna, Szabolcs Semsey, and myself.

The levels of protein expressions are found for different initial conditions of the external environment. This is represented by a state vector \mathbf{s} ; which is a vector of relevant sugar and protein concentrations. The nonlinear equations governing the evolution of the system, the state equations, are the time derivatives of the changing rates of these variables. In the following the LacI tetramer will be referred to as R.

The internal IPTG concentration, [I], depends on the external IPTG level ([IPTG]) as well as the concentration of the permease LacY. In short, IPTG \rightarrow I with the rate:

$$\frac{d[\text{I}]}{dt} = \alpha_A [\text{LacY}] \frac{[\text{IPTG}]}{K + [\text{IPTG}]} - \gamma [\text{I}], \quad (2.1)$$

where γ is the dilution due to cell growth, K is the constant of half saturation for the IPTG uptake, and α_A is the maximum pumping rate of the LacY permease. The first term on the right side of the equality is found experimentally [63]. As α_A is very fast compared to timescales of transcription and translation of the genes, we can regard [I] to be in quasi-equilibrium. Thus, the concentration of inter-cellular IPTG is:

$$[\text{I}] = \alpha_A \frac{[\text{IPTG}]}{\gamma(K + [\text{IPTG}])} [\text{LacY}]. \quad (2.2)$$

Possible states
free
O1
O1O2
O1O3
C1
C1+O1
C1+O1O2
C1+O1O3

Table 2.1: The possible states in our model. The different states are denoted by the occupied sites on the DNA.

I binds to R, with affinity K_I , and prevents R from binding to the DNA. Assuming that the concentration of I is always much larger than the concentration of R, we obtain the concentrations of the active form of the repressor [67]:

$$[R^*] = \frac{[R]}{1 + \frac{[I]^2}{K_I^2}}, \quad (2.3)$$

where the squaring of $[I]/K_I$ comes from the two binding sites on R for IPTG or allolactose.

IPTG and the external glucose concentration defines the environmental conditions of the cell. The state vector is then: $\mathbf{s} = \{\text{IPTG}, \text{cAMP}, \text{R}, \text{LacZ}, \text{LacY}\}$. The level of free RNAPs is abundant so we will assume that the gene will be expressed as soon as the repressor site is free. The four different binding sites (O1, O2, O3, and C1) are either occupied or empty. If R is bound as a loop to O1 and O3 (denoted O1O3) there is no room for an RNAP to bind to the *lacZYA* promoter. As O2 and O3 are considerably weaker bindings, the states O2, and O3 are neglected. With this knowledge and with the experimental results presented in section 2.3.1, we build a model consisting of the eight states in table 2.1.

We assume that the fraction of CAP involved in the regulation of other genes than in the *lac* operon and cAMP bound to other proteins are constant [68]. Furthermore, we assume that all free cAMP binds to CRP; $[\text{cAMP}] \sim [\text{CAP}]$. Only in the free state and the C1 state are RNAPs able to start transcription and produce the whole transcript of the *lacZYA* genes. In the states O1O3 and C1+O1O3, *lacI* is road-blocked and no full transcript can be produced. This means that no R is not expressed.

We make a quasi-steady-state assumption that R and CAP binding reactions are sufficiently rapid, relative to the transcription and translation

rates. Therefore, the probability that a specific protein is expressed, can be calculated, as the sum of the statistical weights of given states normalized with the partition function \mathcal{Z} [69]:

$$P_{protein}(\mathbf{s}) = \frac{\sum_i A_{protein,i} \exp\left(\frac{-\Delta G_i}{k_B T}\right) [\mathbf{R}^*]^{\sigma_i} [\text{CAP}]^{\phi_i}}{\mathcal{Z}}, \quad (2.4)$$

where $A_{protein}$ are the activities given in table 2.2 and the partition function is given as

$$\mathcal{Z} = \sum_i \exp\left(\frac{-\Delta G_i}{k_B T}\right) [\mathbf{R}^*]^{\sigma_i} [\text{CAP}]^{\phi_i}. \quad (2.5)$$

Here ΔG_i represents the energy of the i -th binding state and σ_i and ϕ_i are the numbers of R and CAP molecules bound in that particular state, respectively.

Furthermore, the differential equations describing the evolution of the system can be written as:

$$\frac{d[\mathbf{R}]}{dt} = \alpha_R P_R(\mathbf{s}) - \gamma[\mathbf{R}] \quad (2.6)$$

$$\frac{d[\text{LacZ}]}{dt} = \alpha_Z P_{ZY}(\mathbf{s}) - (\gamma + \zeta_Z)[\text{LacZ}] \quad (2.7)$$

$$\frac{d[\text{LacY}]}{dt} = \alpha_Y P_{ZY}(\mathbf{s}) - (\gamma + \zeta_Y)[\text{LacY}], \quad (2.8)$$

where α_R , α_Z , and α_Y are the maximum production rates of R, LacZ and LacY, respectively. ζ_Z and ζ_Y are degradation rates of LacZ and LacY. Since R and CAP are not actively degraded, decay times are set by dilution during one cell generation, γ . These three ordinary differential equations coupled with equations (2.2) and (2.3) are the state equations of this model. The model is both evaluated deterministically by solving the differential equations for a certain \mathbf{s} and stochastically with a Gillespie algorithm [70]. I did the first and Sandeep Krishna made the Gillespie algorithm.

The experimental results presented in section 2.3.1 shows that the auto-regulation is unaffected by the cAMP level. This gives us that the energies are additive as given in table 2.2. So the binding energy of any one of the eight binding states of the *lac* operon is:

$$\Delta G_i = \varepsilon_{O1,i} + \varepsilon_{O1O2,i} + \varepsilon_{O1O3,i} + \varepsilon_{C,i}. \quad (2.9)$$

This together with the equality deduced below, gives us the values of the individual energies.

Consider the limit where there is no IPTG ($[\text{IPTG}] \sim 0$), then the R production rate is:

$$\frac{d[\mathbf{R}]}{dt} = \alpha_A \frac{1 + [\mathbf{R}^*] \left(\exp\left(\frac{\varepsilon_{O1}}{k_B T}\right) + \exp\left(\frac{\varepsilon_{O1O2}}{k_B T}\right) \right)}{1 + [\mathbf{R}^*] \left(\exp\left(\frac{\varepsilon_{O1}}{k_B T}\right) + \exp\left(\frac{\varepsilon_{O1O2}}{k_B T}\right) + \exp\left(\frac{\varepsilon_{O1O3}}{k_B T}\right) \right)} - \gamma[\mathbf{R}]. \quad (2.10)$$

<i>States</i>	ΔG	A_R	A_{ZY}	σ	ϕ
free	0	1	0.0025	0	0
O1	$-\varepsilon_{O1}$	1	0	1	0
O1O2	$-\varepsilon_{O1O2}$	1	0	1	0
O1O3	$-\varepsilon_{O1O3}$	0	0	1	0
C1	$-\varepsilon_C$	1	1	0	1
C1+O1	$-\varepsilon_C - \varepsilon_{O1}$	1	0	1	1
C1+O1O2	$-\varepsilon_C - \varepsilon_{O1O2}$	1	0	1	1
C1+O1O3	$-\varepsilon_C - \varepsilon_{O1O3}$	0	0	1	1

Table 2.2: The possible states (first column), their energies (second column), the activities of the genes *lacI* (third column), and *lacZYA* (fourth column). The fifth and sixth column are the occupancies of R or CAP, respectively.

The experimental results presented in section 2.3.1 shows that the ratio between the auto-regulated and the fully expressed levels of R is 1/3. Therefore, for the first term on the right hand side of equation (2.10), the ratio between the weights of the states with no auto-regulation (numerator) and the states with auto-regulation (denominator) is 1/3. Furthermore, we conclude that the binding energy of the state O1O2 is very strong and $[R^*] \left(\exp\left(\frac{\varepsilon_{O1}}{k_B T}\right) + \exp\left(\frac{\varepsilon_{O1O2}}{k_B T}\right) \right) \gg 1$. From this we have that equation (2.10) reduces to:

$$\frac{[R^*] \left(\exp\left(\frac{\varepsilon_{O1}}{k_B T}\right) + \exp\left(\frac{\varepsilon_{O1O2}}{k_B T}\right) \right)}{[R^*] \left(\exp\left(\frac{\varepsilon_{O1}}{k_B T}\right) + \exp\left(\frac{\varepsilon_{O1O2}}{k_B T}\right) + \exp\left(\frac{\varepsilon_{O1O3}}{k_B T}\right) \right)} = \frac{1}{3}. \quad (2.11)$$

In this limit no IPTG can bind to R and, therefore, $[R]=[R^*]$ and the steady state value is experimentally found to be $[R] = 0.03$. From Reference [55] we have ε_C and the ratios between ε_{O1O2} and ε_{O1O3} . In combination with equation (2.11), the energies are found to be:

$$\varepsilon_{O1} = \begin{cases} 0, & \text{if the site is empty} \\ 5.4758, & \text{if the site is occupied} \end{cases} \quad (2.12)$$

$$\varepsilon_{O1O2} = \begin{cases} 0, & \text{if the site is empty} \\ 8.4758, & \text{if the site is occupied} \end{cases} \quad (2.13)$$

$$\varepsilon_{O1O3} = \begin{cases} 0, & \text{if the site is empty} \\ 8.9058, & \text{if the site is occupied} \end{cases} \quad (2.14)$$

$$\varepsilon_C = \begin{cases} 0, & \text{if the site is empty} \\ 0.7428, & \text{if the site is occupied} \end{cases} \quad (2.15)$$

The *LacI* production rate, given in table 2.3, is found from the case where IPTG is abundant ($[IPTG] \sim \infty$). In this case only the free and the C1 states

Parameter	Value	Description
α_R	$10^{-3} \mu\text{M min}^{-1}$	LacI production rate, equation (2.17).
α_Z	$1 \mu\text{M min}^{-1}$	LacZ production rate [67].
α_Y	$1 \mu\text{M min}^{-1}$	LacY production rate [67].
γ	0.0116 min^{-1}	Dilution rate [68]
α_A	2000 min^{-1}	LacY pumping rate.
ζ_Z	$8.33 \times 10^{-4} \text{ min}^{-1}$	LacZ degradation rate [71].
ζ_Y	0.65 min^{-1}	LacY degradation rate [68].
K_I	$1 \mu\text{M}$	R-IPTG affinity [72, 73].
K	$680 \mu\text{M}$	Constant for the IPTG uptake [74].

Table 2.3: Parameter values used for simulation. Some of the parameters are taken with the exact values from the reference and others have been changed a little to be consistent with the experiments.

are possible. Hence, the LacI production rate is:

$$\frac{d[\text{R}]}{dt} = \alpha_A - \gamma[\text{R}]. \quad (2.16)$$

As the steady state value is experimentally found to be $[\text{R}] = 0.09 \mu\text{M}$, see section 2.3.1, we have that:

$$\alpha_R = \gamma[\text{R}] = 0.001 \mu\text{M}/\text{min}. \quad (2.17)$$

2.3 Results

2.3.1 Experimental results

From the *in vitro* investigations described in detail in Reference [66] it is shown that R first binds to *O1* and secondly to either *O2* or *O3*. Therefore, the states *O2* and *O3* are discarded in the model, see table 2.2. In addition, it is experimentally shown that the auto-regulation is independent of cAMP level which gives us additive energies.

Furthermore, the effect of auto-regulation on *in vivo* LacI levels is measured. Most of the current models assume that cells contain about 10 LacI tetramers, based on the estimate of Gilbert and co-workers [75]. We measured the average LacI content of cells in the presence and absence of IPTG, corresponding to fully expressed and auto-regulated levels, respectively. This was done with western blotting of a known amount of cells, see figure 2.4.

IPTG	cAMP	LacI	LacZ
0	low	0.03 μM	low
0	∞	0.03 μM	low
∞	low	0.09 μM	low
∞	∞	0.09 μM	0.2 μM

Table 2.4: Result of the deterministic model. The first two columns state the input conditions and the two last are the steady state values after simulation; as shown in figure 2.5. These results mimic exactly the experimental results shown in figure 2.4.

Based on the experiment we estimate that there are about 360 monomers on average per cell in the presence of IPTG, while only 120 monomers per cell can be found in the absence of IPTG. As R is a LacI tetramer and 1 monomer ~ 1 nM [2], the fully expressed level is 0.09 μM and the auto-regulated is 0.03 μM . The latter agrees with the theoretical calculation of 0.030 μM R by Santillan and Mackey [55].

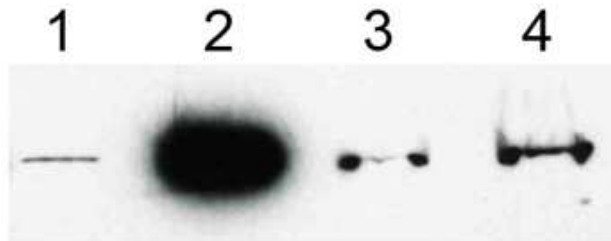


Figure 2.4: The effect of auto-regulation on *in vivo* LacI levels. Proteins collected from MG1655 *E. coli* cells were separated by SDS-PAGE and analyzed by western blotting using an anti-LacI antibody [66]. The original amount of cells were $3 \cdot 10^8$ (lane 3) and $1.5 \cdot 10^8$ (lane 4). Cells were grown in the absence (lane 3) and in the presence (lane 4) of 1 mM IPTG 10^{10} (lane 1) and 10^{11} (lane 2) LacI repressor molecules were loaded as controls. The amount of LacI in cells was determined by quantifying the signals obtained.

2.3.2 Theoretical results

Figure 2.5 mimics the actual protein dynamics shown in figure 2.4. When no IPTG is available the R level is low (0.03 μM) and when IPTG is abundant the R level is high (0.09 μM). These results are summarized in table 2.4. In addition, it is shown that the auto-regulation is independent of the cAMP level as argued here and in Reference [66]. These results are compared to

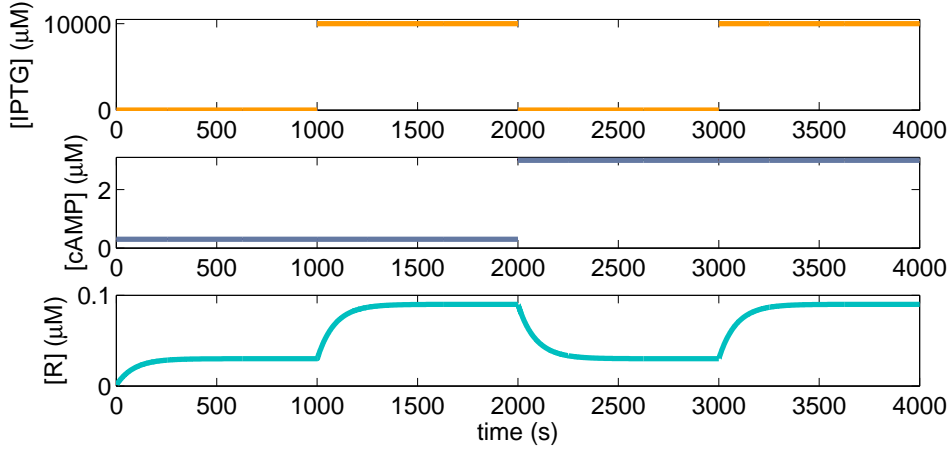


Figure 2.5: Protein dynamics for given concentrations of IPTG and cAMP (two upper panels). The concentration of R is auto-regulated at the low level ($R = 0.03 \mu\text{M}$) and fully expressed at the high level ($0.09 \mu\text{M}$).

two control models; one with a constant low expression of R (control 1) and one with a constant high expression of R (control 2). For control 1, equation (2.6) is replaced by:

$$\frac{d[R]}{dt} = \gamma \cdot 0.03 \mu\text{M} - \gamma [R]. \quad (2.18)$$

and for control 2:

$$\frac{d[R]}{dt} = \gamma \cdot 0.09 \mu\text{M} - \gamma [R], \quad (2.19)$$

These two controls are evaluated and compared to the auto-regulated model in figure 2.6. Here it is seen that control 1 has a fast response to IPTG levels like the auto-regulated model; even in the situation where the glucose is abundant (low cAMP). In other words, the response to even small lactose pulses is to turn *on* the lactose uptake. Furthermore, this shows that the auto-regulation does not give rise to a faster response than control 1 as suggested by Reference [65].

Figure 2.7 shows the nullclines of the 2D system of differential equations of $d[R]/dt$ and $d[\text{LacY}]/dt$. In a phase portrait the nullclines are the curves along which the vector field is either completely horizontal or vertical. A nullcline is a boundary between regions where $d[R]/dt$ or $d[\text{LacY}]/dt$ switch signs [76]. The intersections between R and LacY nullclines are equilibrium points. Hence, two stable points for a specific system signifies bistability. In other words, for the cells under the same environmental conditions the cell can be either *on* or *off* as shown in figure 2.3. This kind of bistable

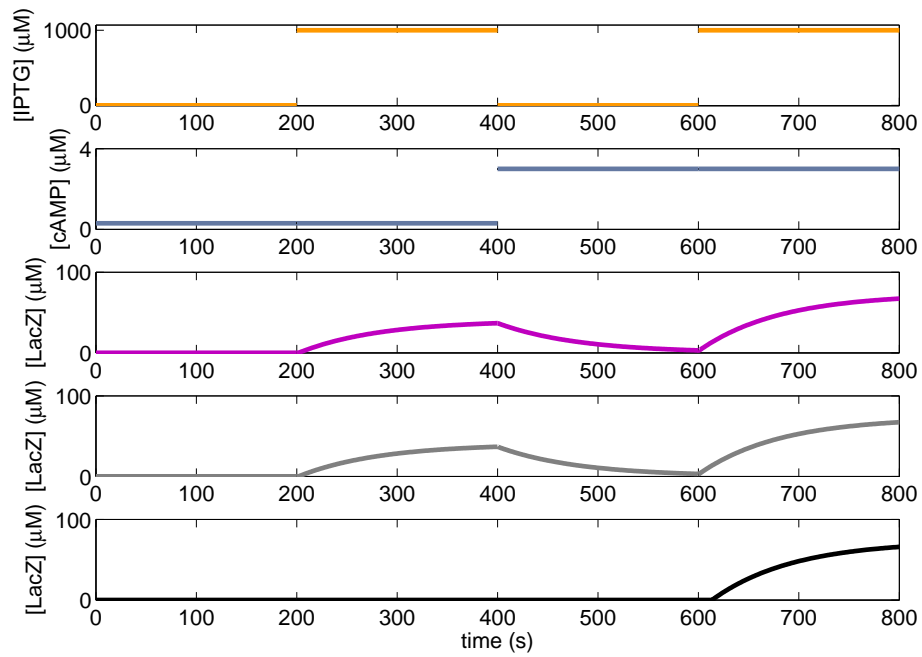


Figure 2.6: Protein dynamics for given concentrations of IPTG and cAMP (two upper panels). The concentration of LacZ with auto-regulation of R (purple curve), control 1 (gray curve), and control 2 (black curve). Note that the auto-regulation model and control 1 responds to high IPTG even in the presence of glucose (low cAMP).

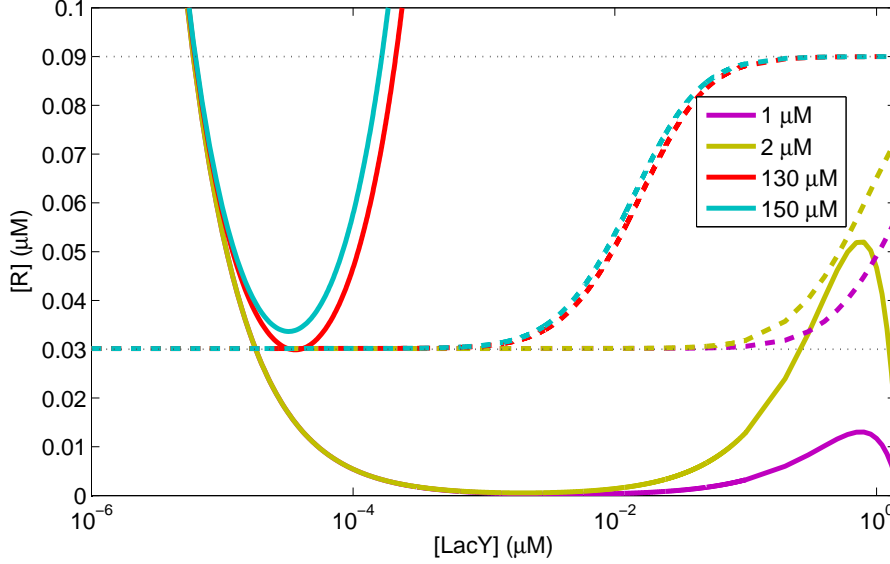


Figure 2.7: The phase portrait for different concentrations of IPTG. The solid lines denote the curves $d[\text{LacY}]/dt = 0$ and the punctuated lines denote $d[\text{R}]/dt = 0$. The black dotted lines show the minimum and maximum levels of R.

switch is termed an epigenetic switch as described briefly in section 1.1. This epigenetic switch of the *lac* operon is well established both experimentally and theoretically. Therefore, this simple model is tested against this well-characterized switch for completeness.

The nullclines are found analytically by considering the rate functions. From equation (2.6) and $d[\text{R}]/dt = 0$ we have:

$$[\text{R}] = 0.015 - 1.79 \cdot 10^{-7}([\text{I}]^2 + \sqrt{7.13 \cdot 10^9 + [\text{I}]^2(8.39 \cdot 10^5 + [\text{I}]^2)}) \quad (2.20)$$

and we know from equation (2.2) that $[\text{I}]$ depends on both $[\text{IPTG}]$ and $[\text{LacY}]$. Likewise, from (2.8) and $d[\text{LacY}]/dt = 0$ we have:

$$[\text{R}] = \frac{(1.5 [\text{LacY}]^{-1}) - 1)(1 + [\text{I}]^2)}{2.8 \cdot 10^6}. \quad (2.21)$$

These are the nullclines shown in figure 2.7 for different values of IPTG. There are two stable points for $\text{IPTG} \geq 2 \mu\text{M}$ and again there is only one stable point for $\text{IPTG} \geq 145 \mu\text{M}$. So these limits define the extent of the bistability region. This is exactly what is shown, for a single cell simulation, in figure 2.8. However, the deterministic evaluation of the model overestimates the extent of the bistability region compared to what is seen experimentally ($3 \mu\text{M} - 20 \mu\text{M}$) [77]. This is accounted for by the stochastic evaluation of

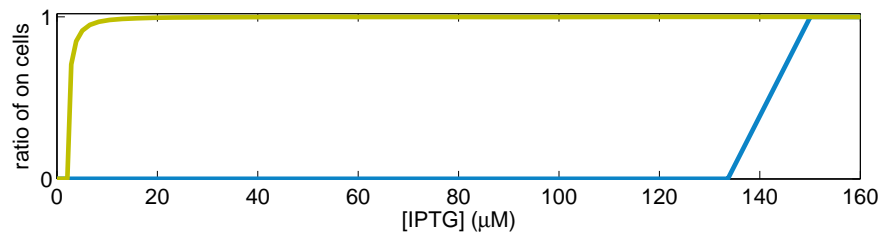


Figure 2.8: The ratio of cells that are *on*, as sketched in figure 2.3, under different concentrations of IPTG. The blue curve shows the ratio of *on* cells, in different IPTG concentrations, for cells that were initially *off*. The green curve is for the cells that were initially *on*. This is the bistability of the *lac* operon.

the model which shows that even small perturbations in the expression of R make the system shift from *off* to *on* much faster [66]. Thus, the extent of the bistability region is lowered drastically compared to the deterministic evaluation of the model discussed here.

2.4 Discussion

The auto-regulation model, described in this chapter, mimics the experimental results presented here and in [66]. In contrast, none of the two control models succeeds in simulating both the epigenetic switch or the fast response in expression of the *lacZYA*. We showed that the cells respond to lactose pulses even when glucose is abundant. This is a way to probe the sugars available for the cell. Hence, the cells have high adaptability to the environment and can change from uptake of glucose to uptake of lactose even when there is glucose in the media.

The individual cells prefer glucose to lactose, so the advantage of this fast response is on the population level. If some cells are willing to empty a pool of lactose, there will be more glucose for other cells. In other words, the resources are allocated to a few instead of being shared among the many.

In this system, the traffic is jammed after initiation and the RNAP produces a truncated transcript. This road-blocking is very effective but it is also a rather costly way to regulate the gene. None of the results given in this chapter or in Reference [66] explain why the cell should choose this strategy compared to one that hinders initiation.

2.5 Conclusion

None of the many mathematical models built so far to study the dynamics of this system considered the fact that the Lac repressor R regulates its own transcription by forming a transcriptional road-block of its own gene. Here the effect of auto-regulation on intracellular LacI levels was measured. Furthermore, it was shown that cAMP-CRP binding does not affect the efficiency of auto-regulation. We built a mathematical model to study the role of LacI auto-regulation in the lactose utilization system. Previously, it has been argued that negative auto-regulation can increase the speed of response. We show that this is not the case for this particular molecular mechanism, a transcriptional road-block used to stop RNAP traffic. Instead, we suggest that LacI auto-regulation increases the system's sensitivity to small amounts of lactose to optimize the usage of small lactose pools to gain an advantage on a population level.

CHAPTER 3

Forces in the standing wave evanescent field

This chapter covers the work I did during my visit in the laboratory of Alexander Rohrbach at IMTEK, Freiburg. The initial experiments reported in the last section of this chapter were done together with Philipp von Olshausen.

3.1 Introduction

It is attractive to develop high spatial resolution techniques with high imaging speeds. This is possible with a technique based on wide-field imaging in contrast to techniques that rely on scans of a sample. The resolution is improved in standing-wave (SW) illumination compared to bright-field imaging.

A plane wave enters the sample with an incident angle of θ_i and for angles above a critical angle θ_c total internal reflection occurs. When the medium at the interface has a lower refractive index than glass an evanescent field is produced. This is used for total internal reflection fluorescence (TIRF) microscopy. In addition, two plane waves, that are totally internally reflected, interfere and create a standing wave evanescent field (SW-TIRF). Since the image resolution is proportional to the excitation wavelength, SW-TIRF provides extended resolution by utilizing that the standing evanescent wave has an effective wavelength of $\lambda/2n_{glass} \sin \theta_i$, where λ is the wavelength of the laser beam in vacuum, and n_{glass} is the index of refraction of glass [79]. Hence this is a way to pass the resolution limit; given by the Rayleigh criterion in equation (1.4). For visual light the resolution limit is ~ 200 nm and with

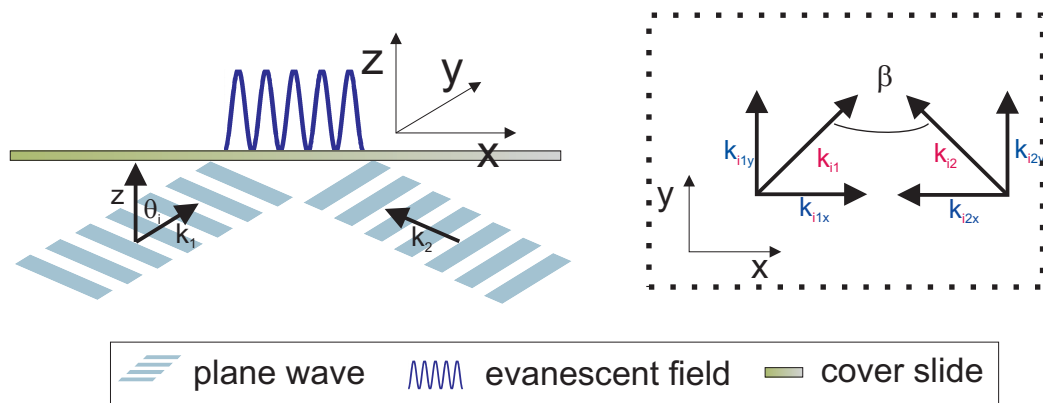


Figure 3.1: A sketch of the setup of a standing wave evanescent field as it is produced in the laboratory of Alexander Rohrbach. Two Gaussian beams enter the sample with an angle of θ_i . The wavelengths in vacuum of the incoming plane waves are 488 nm. The setup is described in detail in reference [78]. The inset shows the vector decomposition in the surface plane of the incoming waves. The angle between the vectors is denoted β .

structured illumination it is possible to lower this limit with a factor of two [80]. This high resolution microscopy requires investigation of the interference patterns of Moiré fringes as described by the groups of Gustafsson and Soe [79, 80, 81, 82]

In short, a single plane wave produces an evanescent field as known for TIRF microscopy and two interfering plane waves gives a structured illumination. With an appropriate tuning of the parameters SW-TIRF is obtained. The aim of the study presented in this chapter, is to quantify the trapping properties of SW-TIRF.

In this chapter the forces acting on a sphere in this evanescent field will be investigated. The force components of the gradient forces and the scattering forces will be considered individually in sections 3.2.3 and 3.2.4, respectively. In section 3.3 the trapping potential and trapping strength will be considered and a possible comparison to the diffusive behavior of a bead in SW-TIRF will be sketched. All these calculations rely on the knowledge of the forces in a single plane wave as exhaustively calculated in Reference [83]. At last, in section 3.4 some initial experiments will be reported.

The groups of Pavel Zemánek and Kishan Dholokia have successfully trapped polystyrene particles in evanescent fields and showed the active movements of these particles by modulating the SW to create a conveyor belt [84, 85, 86]. However, these results were achieved by use of high laser powers and are not applicable for active rheology in living cells or for other

biological assays. That is why we set out to do the following investigation.

3.2 Standing wave evanescent field

The intensity of the evanescent wave in the direction perpendicular to the surface, z , is given as:

$$I(z) = I_0 \cdot \exp(-z/d), \quad (3.1)$$

where $I_0 = I|_{z=0}$ for the intensity of the incoming light and the penetration depth d is defined as the distance from the surface where the intensity falls by $1/e$:

$$d = \frac{\lambda}{4\pi \sqrt{n_{glass}^2 \sin^2 \theta_i - n_m^2}}, \quad (3.2)$$

where n_m is the refractive index of the medium. The angle θ_i must be larger than the critical angle θ_c for total internal reflection to occur [78]. This angle is defined as:

$$\theta_c = \arcsin \left(\frac{\sin \theta_c \cdot n_{glass}}{n_m} \right) \quad (3.3)$$

Two plane waves, with wave vectors \mathbf{k}_1 and \mathbf{k}_2 , are both totally internal reflected. As it is the case for all electromagnetic waves, the plane evanescent waves interfere when overlaid and an SW is created as illustrated in figure 3.1. The structured SW-TIRF illumination created above the interface has the period:

$$P_{ev} = \frac{\lambda}{\sin(\theta_i) \cdot n_{glass}}. \quad (3.4)$$

3.2.1 Intensity

The intensity in the x, y plane of the SW is given as:

$$I(x, y) \propto |E_1(x, y)^2 + E_2(x, y)^2|^2 \quad (3.5)$$

$$\propto |E_1(x, y)|^2 + |E_2(x, y)|^2 + 2\text{Re}(E_1(x, y)^* E_2(x, y)). \quad (3.6)$$

The two incoming waves have the energies E_1 and E_2 and wave vectors \mathbf{k}_1 and \mathbf{k}_2 , drawn in the inset of 3.1, which are defined as

$$\mathbf{k}_1 = (k_{1x}, k_{1y}, 0) \quad (3.7)$$

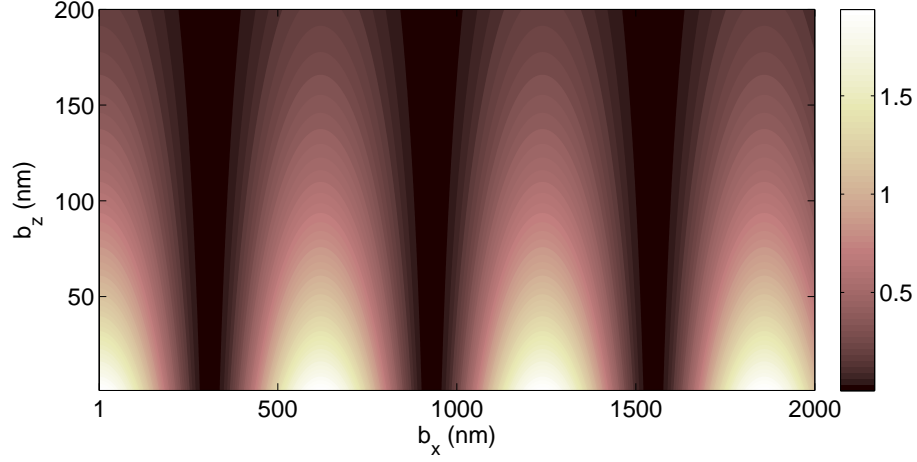


Figure 3.2: A contour plot of the total scalar intensity $I(x, y, z)$ experienced by a sphere at position $\mathbf{b} = (b_x, b_y, b_z)$ in the x, z plane above the surface. The intensity is constant in the y -direction. Parameters from table 3.1 is used for this plot and I is normalized with I_0 .

and

$$\mathbf{k}_2 = (k_{2x}, k_{2y}, 0) \quad (3.8)$$

so that $|\mathbf{k}_1| = |\mathbf{k}_2| = k = 2\pi n_{\text{glass}}/\lambda$. From this we have that the intensity $I(x, y)$ is:

$$I(x, y) = I_1(x, y) + I_2(x, y) + 2\sqrt{I_1(x, y) \cdot I_2(x, y)} \cdot \cos((\mathbf{k}_1 - \mathbf{k}_2)\mathbf{x} + \Delta\gamma), \quad (3.9)$$

where γ is the phase difference between the two plane waves. The difference between these vectors are $\mathbf{k}_1 - \mathbf{k}_2$

$$(\mathbf{k}_1 - \mathbf{k}_2)(\mathbf{r}) = (k_x + k_x, k_y - k_y, 0)(x, y, 0) = 2k_x x \quad (3.10)$$

and the interference of these two plane waves creates an SW in the x -direction, with the wave number $|\mathbf{k}_1 - \mathbf{k}_2| = 2k_x$. Combining the intensity in the x, y , and z directions gives the intensity:

$$I(x, y, z) = I_0 \exp\left(\frac{-z}{d}\right) (1 + \cos(2k_x x + \Delta\gamma)) \quad (3.11)$$

The total intensity is found from integration over the particle volume as a function of the radius a and the position in the evanescent field denoted by the vector $\mathbf{b} = (b_x, b_y, b_z)$.

$$I(a, \mathbf{b}) = \int_V I(x, y, z) dV. \quad (3.12)$$

We consider the case where there is no phase difference between the two waves, i.e., $\Delta\gamma$ is set to zero. The total intensity in Cartesian coordinates is

$$I(a, \mathbf{b}) = \int_{-a}^a \int_{-\sqrt{a^2-x^2}}^{\sqrt{a^2-x^2}} \int_{-\sqrt{a^2-x^2-y^2}}^{\sqrt{a^2-x^2-y^2}} e^{-\frac{(z+bz)}{d}} \cdot (1 + \cos(2k_x(x + b_x))) dx dy dz. \quad (3.13)$$

This integral is not easily solved but can be reduced to

$$I(a, \mathbf{b}) = I_0 2de^{-\frac{bz}{d}} \int_{-a}^a \int_{-\sqrt{a^2-x^2}}^{\sqrt{a^2-x^2}} (1 + \cos(2k_x(b_x + x))) u dy dx, \quad (3.14)$$

where, for simplicity, the following function is introduced:

$$u(a, x, y) = \sinh\left(\frac{\sqrt{a^2 - x^2 - y^2}}{d}\right) \quad (3.15)$$

The total intensity is numerically calculated, using the parameters from table 3.1, and plotted in figure 3.2.

3.2.2 Force decomposition

The gradient and scattering forces are derived from the Lorentz force as it is described in detail by Alexander Rohrbach and collaborators [87]:

$$\mathbf{F} = q(\mathbf{E} + v \times \mathbf{B}), \quad (3.16)$$

where v is the velocity, q the electrical charge, and \mathbf{B} the magnetic field. The response on the total electrical field is assumed to be: $\mathbf{p} = \alpha\epsilon\mathbf{E}$, where α is the polarizability and $\epsilon = n^2$ is the electric permittivity. Higher polarization orders are neglected here [87, 88, 89] and the polarization α on a volume element is given by the Clausius-Mossotti theorem. More about this theorem and α will be provided in section 4.3.2.

From the Lorentz force we obtain the force on a particle, when absorption is discarded, in an optically induced electromagnetic field [87]. The two components of the force are commonly called the gradient force, resulting from the intensity gradient, and the scattering force. The strength of both forces is dependent of the polarizability of the particle. When integrated over the particle volume [88, 89]:

$$\begin{aligned} \mathbf{F}(\mathbf{b}) &= \int_V \frac{\alpha n_m}{2cV} \nabla I(\mathbf{b}) dV \\ &+ I(\mathbf{b}) \frac{n_m}{kC} \left(C_{ext} \mathbf{k}_i \overline{\cos \theta_i} - C_{sca} \mathbf{k}_s \overline{\cos \theta_s} \right) \end{aligned} \quad (3.17)$$

where C_{ext} and C_{sca} are the extinction and scattering cross sections. The terms $\cos \theta_i$ and $\cos \theta_s$ are the asymmetry factors of the incoming field and the scattered field, respectively.

The space variant gradient ∇I of the incident intensity $I = c\epsilon/2 \cdot |E_i|^2$ is averaged over the particle in real space. This is the first order Born approximation; which is defined below. With this elaborate calculations of the electric fields on the surface or of the exact internal fields is avoided [87, 88, 89].

In the following I will focus on the force components individually and specifically for spherical particles in the electric field induced by a evanescent standing wave. This is the Rayleigh-Gans regime, also called the Born approximation. Conditions that defines this regime are [90]:

- The complex refractive index relative to the surrounding medium is close to 1: $|\frac{n_{bead}}{n_m}| \approx 1 + \sigma, \sigma \ll 1$
- The scatterer only induces a small phase shift of the incoming wave: $2ka|\frac{n_{bead}}{n_m}| \ll 2\pi$. This restriction on the size is more relaxed than for an ordinary Rayleigh scatter where $a \ll \lambda$.
- As a consequence, the efficiency factor Q_{ext} , which will be defined in section 3.2.4, is $\ll 1$.

The physical basis can be described in the following way: each volume element contributes to the Rayleigh scattering individually of the other volume elements. The waves scattered in a given direction by these individual elements interfere due to the volume elements different positions in space. To calculate the interference effects, all scattered waves are referred to a common origin and the complex amplitudes are added [90].

3.2.3 Gradient force

It is assumed that the gradient forces of the evanescent field are unaffected by the scattering intensity. Reconsidering equations (3.17) and (3.14) the gradient force in Cartesian coordinates is

$$\mathbf{F}_{grad}(a, \mathbf{b}) = \frac{\alpha n_m}{2cV} \int_{-a}^a \int_{-\sqrt{a^2-x^2}}^{\sqrt{a^2-x^2}} \int_{-\sqrt{a^2-x^2-y^2}}^{\sqrt{a^2-x^2-y^2}} \nabla I(a, \mathbf{b}) dx dy dz \quad (3.18)$$

where the intensity as a function of the position \mathbf{b} is given as

$$I(a, \mathbf{b}) = I_0 e^{-(z+b_z)/d} \cdot (1 + \cos(2k_x(b_x + x))). \quad (3.19)$$

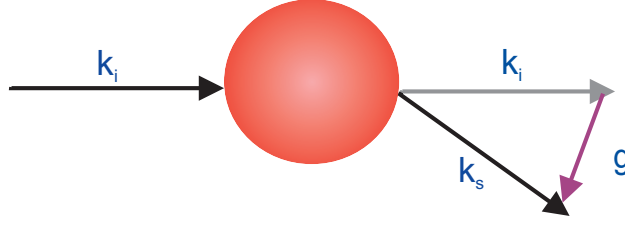


Figure 3.3: The wave vector \mathbf{k}_i of the incoming wave is scattered by the particle and the resulting scattered wave has the wave vector \mathbf{k}_s . The difference between these two vectors, $\mathbf{k}_s - \mathbf{k}_i = \mathbf{g}$, is the momentum transfer. This is a top view of the illustration shown in figure 3.1.

The gradient vector field of the scalar intensity is

$$\nabla I(a, \mathbf{b}) = \left\{ \frac{\partial I}{\partial x}, \frac{\partial I}{\partial y}, \frac{\partial I}{\partial z} \right\} \quad (3.20)$$

$$= I_0 \left\{ -e^{-\frac{(z+b_z)}{d}} 2k_x \sin(2k_x(b_x + x)), 0, -\frac{e^{-\frac{(z+b_z)}{d}} (1 + \cos(2k_x(b_x + x)))}{d} \right\}$$

We can reduce this gradient field exactly to obtain the gradient force

$$\mathbf{F}_{grad}(a, \mathbf{b}) = -I_0 \frac{\alpha n_m}{cV} e^{-\frac{b_z}{d}} \quad (3.21)$$

$$\left\{ d 2k_x \int_{-a}^a \int_{\sqrt{a^2-x^2}}^{\sqrt{a^2-x^2}} \sin(2k_x(b_x + x)) u \, dy dx, \right.$$

$$0,$$

$$\left. \int_{-a}^a \int_{-\sqrt{a^2-x^2}}^{\sqrt{a^2-x^2}} (1 + \cos(2k_x(b_x + x))) u \, dy dx \right\}$$

The gradient force field has a component in the x and z directions; i.e., perpendicular to the wave front and perpendicular to the surface. The x components is sinusoidal and alters between an attractive and a repulsive force. In contrast, the force component in the z -direction changes as $1 + \cos$ and the sign is constant; pulling the particle towards the surface.

3.2.4 Scattering force

Now the scattering force term from equation (3.17) is reconsidered.

$$\mathbf{F}_{scat}(\mathbf{b}) = I(x, y, z) \frac{n_m}{kC} \left(C_{ext} \mathbf{k}_i \overline{\cos \theta_i} - C_{sca} \mathbf{k}_s \overline{\cos \theta_s} \right) \quad (3.22)$$

The extinction cross section C_{ext} is what is taken out of the propagating beam due to the momentum change when encountering the scatterer; here a spherical particle. The extinction cross section is: $C_{ext} = C_{abs} + C_{sca}$. In a plane wave, when absorption is discarded, $C_{ext} = C_{sca} = Q_{sca} \pi a^2$; the product of the scattering efficiency Q_{sca} and the geometrical cross section of the sphere. In the case of a standing wave evanescent field, the factor in the parentheses is summed over the two incoming plane waves with wave vectors \mathbf{k}_1 and \mathbf{k}_2 :

$$\begin{aligned} & C_{ext} \mathbf{k}_i \overline{\cos \theta_i} - C_{sca} \mathbf{k}_s \overline{\cos \theta_s} = \\ & C_{ext,1} \mathbf{k}_{i1} (1 - \overline{\cos \theta_{s1}}) + C_{ext,2} \mathbf{k}_{i2} (1 - \overline{\cos \theta_{s2}}). \end{aligned} \quad (3.23)$$

Here some approximations are made to simplify the calculations in the following:

First, the scattering cross section $C_{ext,12} \sim C_{ext,1} = C_{ext,2}$ which is denoted as C_{ext}' in the proceeding. The exact scattering cross section is the integral of the resulting electric field over the entire Fourier space, given by equation (37) in [87].

Secondly, a similar approximation of the symmetry factor is made $\overline{\cos \theta_{i12}} \sim \overline{\cos \theta_{i1}} = \overline{\cos \theta_{i2}}$. The exact asymmetry factor is given as the integral over the Fourier space in equation (39) of [87]. Whether these approximations are reasonable or to which extent will not be discussed further as it requires a comparison to an eventual analytical calculation. However, accepting the approximations and the simplifications $C_{ext,12} = C_{ext}'$ and $\overline{\cos \theta_{s12}} = \overline{\cos \theta_s}$, equation (3.22) can be written as

$$\begin{aligned} \mathbf{F}_{scat} &= I(x, y, z) \frac{n_m}{kC} C'_{sca} (1 - \overline{\cos \theta_s}) (\mathbf{k}_1 + \mathbf{k}_2) \\ &= I(x, y, z) \frac{n_m}{kC} C'_{sca} (1 - \overline{\cos \theta_s}) (k_x - k_x, k_y + k_y, 0 + 0) \\ &= I(x, y, z) \frac{n_m}{kC} C'_{sca} (1 - \overline{\cos \theta_s}) 2k_y y \end{aligned} \quad (3.24)$$

From this it is seen that the scattering force only has a component along the y-axis, i.e. the direction of the lines in the light grid.

In the case of a standing wave evanescent field the scattering cross section C'_{sca} depends on the position in the field. To find C'_{sca} we first have to consider

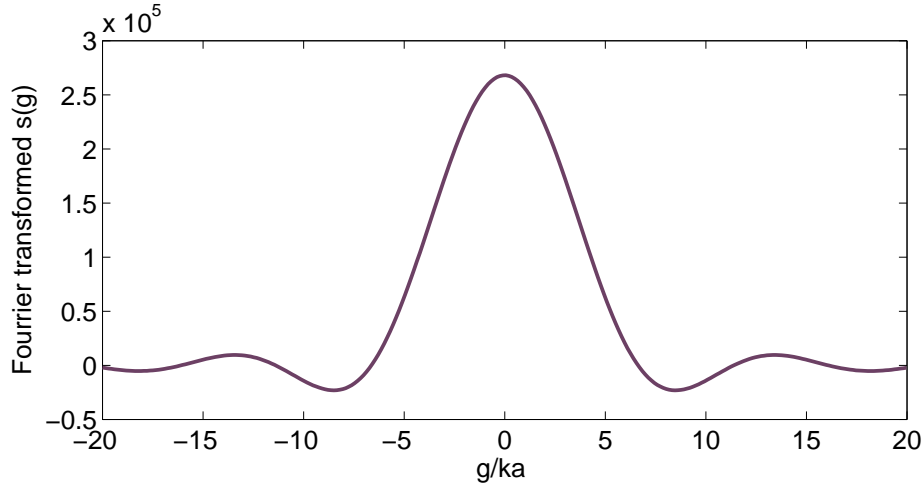


Figure 3.4: The fourier transform of the form factor $\tilde{s}(\mathbf{g})$ given in equation (3.25). Parameters from table 3.1 are used for this plot.

the scattering efficiency. Then, this is multiplied by the area A' which is the area hit by the photons of the SW. The fraction A' over the geometrical cross section πa^2 is smaller than or equal to 1.

Amplitude scattering matrix for a plane wave

The linearity of the boundary conditions imposed by the Maxwell equations, allows the relationship between incident and scattered electric field to be expressed concisely in matrix form as the S-matrix [90]. The S-matrix is the operator that combines the incoming photons to the scattered photons; known as the scattering amplitude. The matrix equation will be valid for all distances, as long as they are sufficiently far from the origin of the scatterer, i.e. more than some wavelengths.

For the Rayleigh-Gans regime the S-matrix is given as the S-matrix of a homogeneous Rayleigh scatterer multiplied by the Fourier transform of the form factor $\tilde{s}(\mathbf{g})$. \mathbf{g} is the difference between the incoming plane wave and the scattered wave vectors: $\mathbf{k}_s - \mathbf{k}_i$, as shown in figure 3.3. The form factor is independent of the polarization and the polarization of the scattered light is the same as for Rayleigh scattering [90]. Furthermore, the form factor is a heavy side step function with a width of the particle ($2a$) [87]. The Fourier transform of $s(\mathbf{g})$ is given as

$$\tilde{s}(\mathbf{g}) = \frac{3}{\mathbf{g}^3} \cdot V \cdot (\sin \mathbf{g} - \mathbf{g} \cos \mathbf{g}) \quad (3.25)$$

when $\theta \neq 0$ and else 1. The variable $\mathbf{g} = 2ka \sin(\theta/2)$, where θ is the angle to the optical axis [90]. $\tilde{s}(\mathbf{g})$ is plotted in figure 3.4.

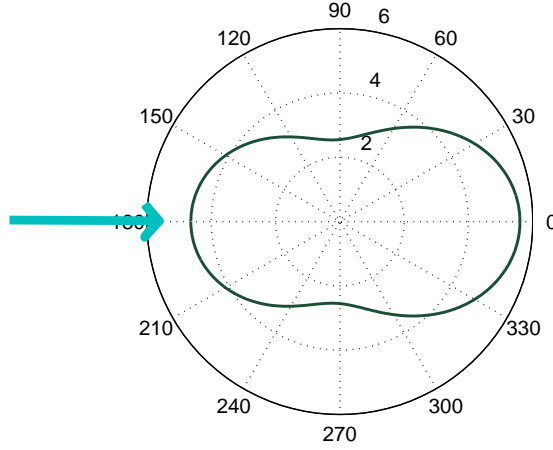


Figure 3.5: A polar plot of the scattering intensity I_{scat} , given by equation (3.28) and normalized with $10^7 I_0$. The x -axis is the optical axis of the incoming plane wave and the direction is denoted by the blue arrow. Parameters from table 3.1 are used for this plot.

Reconsidering the S-matrix, the off-diagonal matrix elements are zero for a spherical scatterer and the diagonal elements are [90]:

$$S1(\theta) = -\frac{ik^3}{4\pi} \cdot \alpha \cdot \tilde{s}(\mathbf{g}) \quad (3.26)$$

$$S2(\theta) = -\frac{ik^3}{4\pi} \cdot \alpha \cdot \tilde{s}(\mathbf{g}) \cdot \cos \theta. \quad (3.27)$$

The scattering intensity of a homogeneous sphere in a plane wave is the intensity for a Rayleigh scatterer, $I_{Rayleigh}$, times the square of the form factor [90]:

$$\begin{aligned} I_{scat}(\theta) &= I_{Rayleigh} \cdot \tilde{s}(\mathbf{g})^2 \\ &= (1 + \cos^2 \theta) k^4 \cdot |\alpha|^2 \tilde{s}(\mathbf{g})^2. \end{aligned} \quad (3.28)$$

This scattering intensity for a single plane wave and a spherical scatterer is plotted in figure 3.5.

Name	Notation	Value
initial intensity	I_0	1 N nm ⁻¹ s ⁻¹
position (b_x, b_y, b_z)	b	(0,20,60) nm
radius of bead	a	40 nm
vacuum wavelength	λ	488 nm
incoming wave	λ/n_{glass}	321 nm
refractive index of bead	n_{bead}	1.57+i 0.03
refractive index of medium	n_m	1.34
refractive index of glass	n_{glass}	1.52
refractive index	$m = n_{bead}/n_m$	1.067 + i 0.002238
volume of bead	$V = \frac{4}{3}\pi a^3$	$\cdot 2.68 \cdot 10^5$ nm ³
velocity of light	c	$3 \cdot 10^{17}$ nm s ⁻¹
incoming angle	θ_i	68°
angle between \mathbf{k}_1 and \mathbf{k}_2	β	$\pi/6$
wave number of \mathbf{k}_1 and \mathbf{k}_2	k	0.0196 nm ⁻¹
wave number \mathbf{k}_x	$k_x = k \sin \beta$	0.00507 nm ⁻¹
wave number \mathbf{k}_y	$k_y = k \cos \beta$	0.0189 nm ⁻¹
penetration depth	d	89 nm
polarizability	$\alpha = 3V \frac{m^2-1}{m^2+2}$	(35574.6 + i 1170.18) nm ³
asymmetry factor	$\frac{1}{\cos \theta_s}$	0.04 [90]

Table 3.1: The parameter values used for all calculations as well as for the plots.

Calculation of the scattering cross section

The scattering cross section for a spherical particle in a plane wave is

$$C_{sca} = \frac{4\pi}{k^2} \operatorname{Re}(S1|_{\theta=0}) \approx \frac{8\pi}{3k^2} \left| -\frac{ik^3}{4\pi} \alpha \tilde{s}(0) \right|^2 \quad (3.29)$$

this is valid for the Born approximation. The scattering efficiency for a single plane wave is

$$Q_{sca} = \frac{C_{sca}}{\pi a^2} \quad (3.30)$$

To obtain the scattering cross section of a sphere in SW-TIRF, given the approximation mentioned above, the effective area A' is found to be

$$\begin{aligned} A' &= \int_{-a}^a \int_{-\sqrt{a^2-x^2}}^{\sqrt{a^2-x^2}} e^{-(z+bz)/d} \cdot (1 + \cos(2k_x(x+b_x))) dz dx \quad (3.31) \\ &= \int_{-a}^a 2de^{-\frac{bz}{d}} \cdot (1 + \cos(k(x+b_x))) \sinh\left(\frac{\sqrt{a^2-x^2}}{d}\right) dx, \end{aligned}$$

where $A' \leq \pi a^2$ and, therefore,

$$C'_{sca} = Q_{sca} \cdot A' \leq C_{sca}. \quad (3.32)$$

The total intensity, the gradient force, and the scattering force components are calculated with parameter values from table 3.1 and shown in figure 3.6. From this figure we get that both force gradient components and the scattering force component changes along the x -direction. $F_{grad,x}$ has its maximum where the intensity gradient is largest. Thus, the bead will be pulled to the most intensive region. $F_{grad,z}$ is most pronounced at the point of maximum intensity. Hence, here the bead is pulled towards the surface. Likewise, it is at the maximum intensity that $F_{scat,y}$ is largest.

For for comparison the evanescent field created by a single plane wave is considered in appendix A. This have been solved analytically in Reference [83].

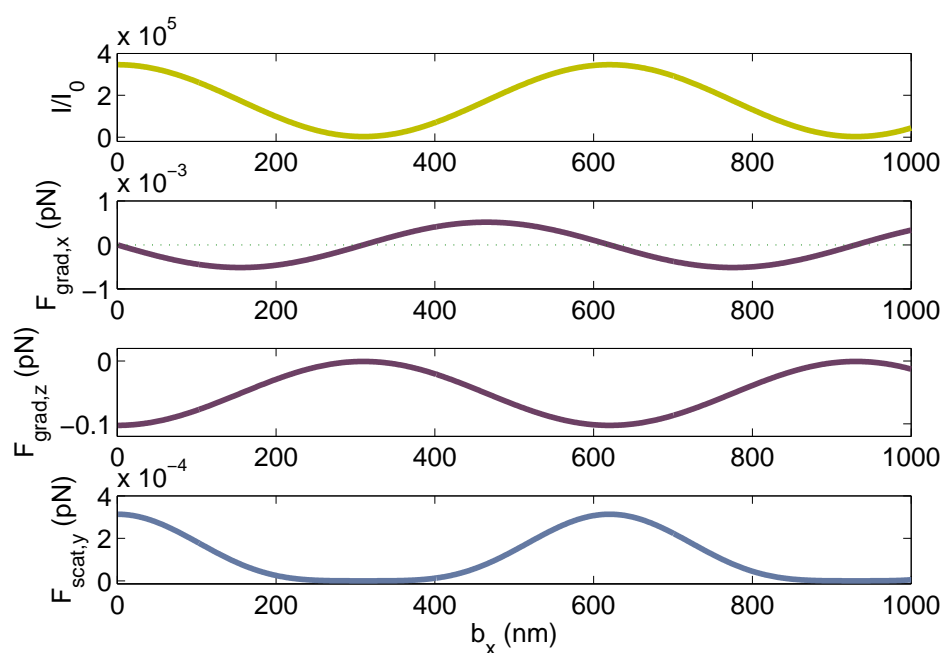


Figure 3.6: A polystyrene sphere in SW-TIRF. The total intensity normalized with I_0 , as given in equation (3.14). The gradient force components and the scattering force. All are numerically calculated as a function of x -positions of the sphere, with parameters from table 3.1. The period of the SW is 600 nm.

3.3 Trapping efficiencies and trapping strength

To investigate the manipulating properties of the SW-TIRF further we calculate the trapping efficiencies [87]. These are dimensionless and denoted by \mathbb{Q} :

$$\mathbb{Q}(r) = \mathbb{Q}_{grad}(r) + \mathbb{Q}_{scat}(r). \quad (3.33)$$

In this section the gradient efficiencies in the x and z -direction will be found separately as well as the scattering efficiencies in the y -direction. To obtain \mathbb{Q} , \mathbf{F}_{grad} and \mathbf{F}_{scat} is normalized with the total force $Pn_m/c \approx I_0 \cdot \pi a^2 n_m/c$, where πa^2 is the geometrical cross section of the sphere and P is the laser power at the sample. From this we get the gradient efficiency in the radial direction r :

$$\begin{aligned} \mathbb{Q}_{grad}(r) = & -\frac{\alpha}{V\pi a^2} e^{-\frac{b_z}{d}} \quad (3.34) \\ & \left\{ d 2k_x \int_{-a}^a \int_{\sqrt{a^2-x^2}}^{\sqrt{a^2-x^2}} \sin(2k_x(b_x+x))u \, dydx, \right. \\ & 0, \\ & \left. \int_{-a}^a \int_{-\sqrt{a^2-x^2}}^{\sqrt{a^2-x^2}} (1 + \cos(2k_x(b_x+x)))u \, dydx \right\}. \end{aligned}$$

Likewise the scattering efficiency is found to be

$$\begin{aligned} \mathbb{Q}_{scat}(r) &= I(x, y, z) \frac{1}{I_0 k\pi a^2} C'_{sca} (1 - \overline{\cos \theta_s}) 2k_y \quad (3.35) \\ &= \frac{e^{(b_z+z)/d}}{k\pi a^2} (1 + \cos(2k_x(b_x+x))) C'_{sca} (1 - \overline{\cos \theta_s}) 2k_y. \end{aligned}$$

The different components of \mathbb{Q} are evaluated with regard to the refractive index n of the trapped particle in figure 3.7 for different incident angles β . From this it is seen that \mathbb{Q}_{grad} grows linearly with n , hence, stabilizing the particle in the x, z plane. However for large n , \mathbb{Q}_{scat} dominates and the particle is pushed in the y -direction. In figure 3.8 \mathbb{Q} is shown as a function of the particle radius. Note that the maximum $\mathbb{Q}_{grad,z}$ overlaps with the maximum $\mathbb{Q}_{grad,x}$. Hence, for the parameter shown in table 3.1 the optimal radius of a dielectric sphere is $a \sim 70$ nm.

From here the natural path to follow is to approximate the potential created at the most intense parts of the pattern by a harmonic well. Then finding the potential by integrating over the entire space

$$V(r) = \int_{-\infty}^r F(r') dr' \quad (3.36)$$

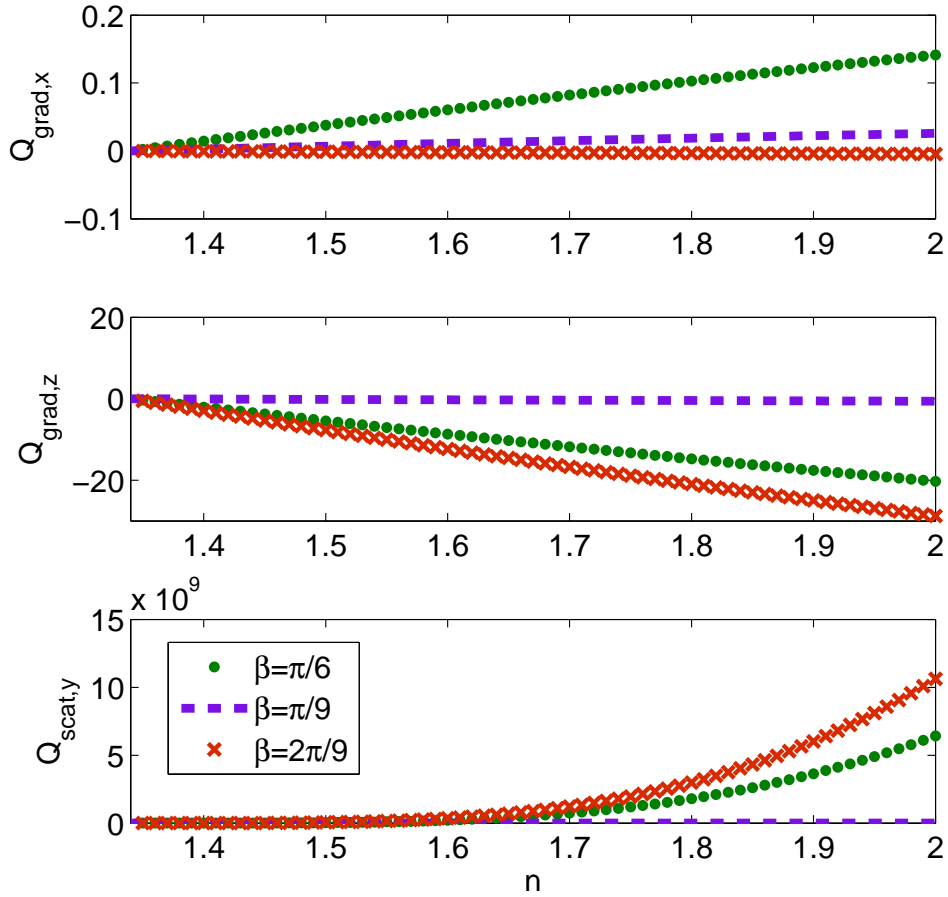


Figure 3.7: Gradient and scattering trapping efficiencies, as given by equations (3.34) and (3.35), versus the refractive index n . The parameters from table 3.1 are used for this plot. However, b_x is set to 500 nm and appropriate changes for other parameters have been done, e.g., b_z is set to a . Furthermore, for plotting $Q(n)$ the asymmetry factor $\cos \theta_s$ is kept constant [90]. The trapping efficiency is plotted for 3 different angles β between the incoming plane waves, see figure 3.1. The period of the SW is 600 nm.

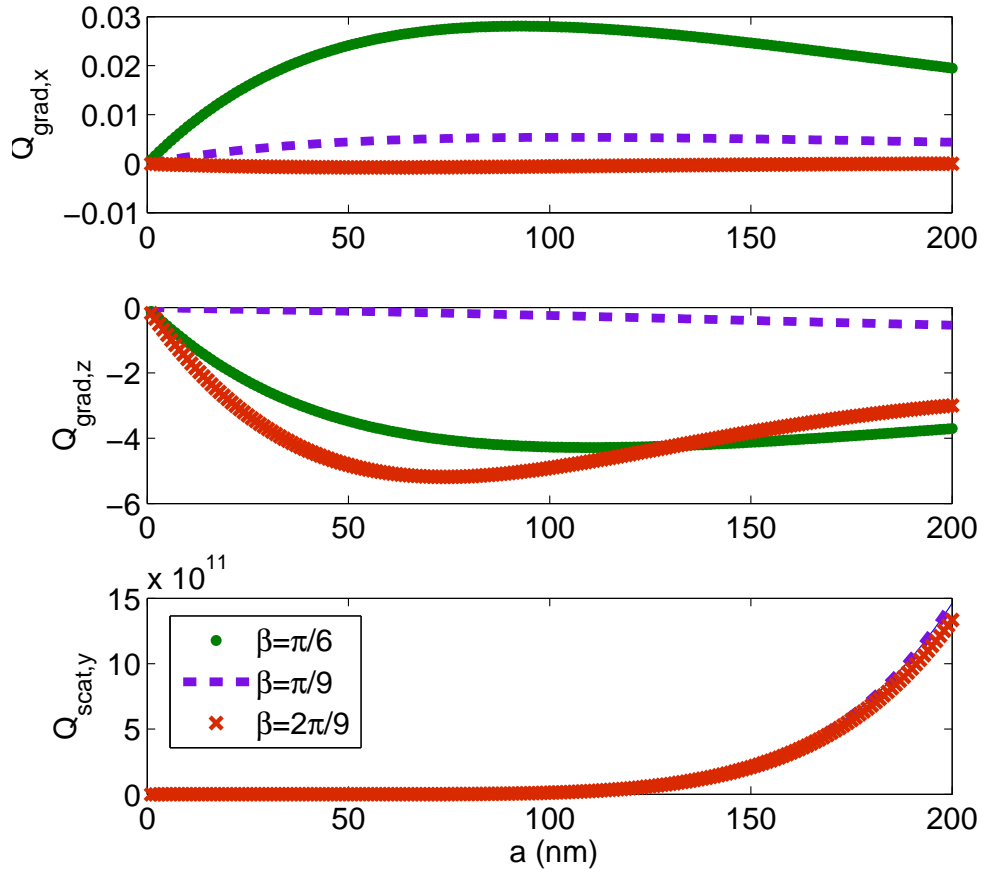


Figure 3.8: Gradient and scattering trapping efficiencies, as given by equations (3.34) and (3.35), versus the radius of the sphere a . The parameters from table 3.1 are used for this plot. However, b_x is set to 500 nm and appropriate changes for other parameters have been done, e.g., b_z is set to a . The trapping efficiency is plotted for 3 different angles β between the incoming plane waves, see figure 3.1. The period of the SW is 600 nm.

and in one direction we get:

$$V(x) = \int_{-\infty}^x F_{grad}(x') dx' \approx \frac{1}{2} \kappa x^2, \quad (3.37)$$

when evaluated in the potential minimum

$$\frac{\partial I}{\partial x} = 0. \quad (3.38)$$

The second derivative of the $V(x)$ is the trapping strength κ :

$$\kappa_x = \partial_x (F_{grad}(x) + F_{scat}(x)). \quad (3.39)$$

As the scattering force has no component in the x -direction, $\partial_x (F_{scat}(x)) = 0$. Hence, this κ is easily found. In the example shown in figure 3.6 we find that $\kappa/I_0 \sim 5 \cdot 10^{-3}$ pN/ μ m at maximum intensity. For this particular example we do not know the value of I_0 and we can not determine the correct value of κ .

However, a theoretical estimate of κ can be compared to measurements since it can be found experimentally from investigations of particles motions. The spring constant κ will be reconsidered in chapter 4.

3.4 Experiments

The diffusion of polystyrene beads in SW-TIRF is investigated, to register the possible effect of the optical forces in the field. In this section the method will be sketched and some initial experiments will be presented as a proof of principle.

Methods

Fluorescent beads ($a=180$ nm) are diluted 1:4000 in water and mixed 1:1 with a fluorescein solution diluted 1:10. A small droplet is placed on a cover slide and a lit of another smaller cover slide confines the beads in the z -direction. This simple sample chamber is sealed with vacuum grease to minimize the drift. Only the diffusion in the x, y plane is investigated. Therefore, the fast Brownian motions in the z -direction limits the time series to about 2 s with a frame rate of 10/s. The motion in the x and y -directions are analyzed separately to find the diffusion. For these analysis the conversion from pixels to metric scale is assumed to be 100 nm/pixel.

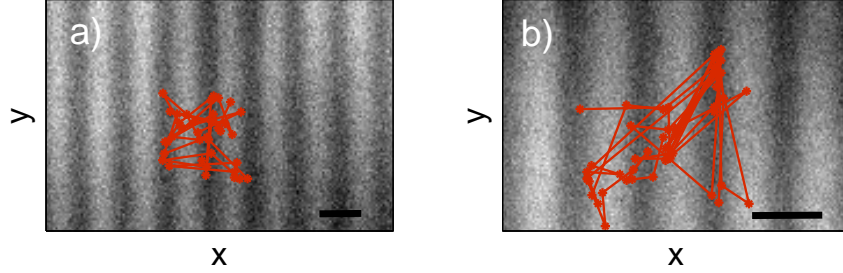


Figure 3.9: a) Intensity image of SW-TIRF with $\beta = \pi/9$ and a period of SW $P_{ev} \sim 2 \mu\text{m}$ (bar). b) $\beta = \pi/15$ and $P_{ev} \sim 3 \mu\text{m}$ (bar). The traces of diffusing spheres ($a=180 \text{ nm}$), projected onto the planes, are overlaid.

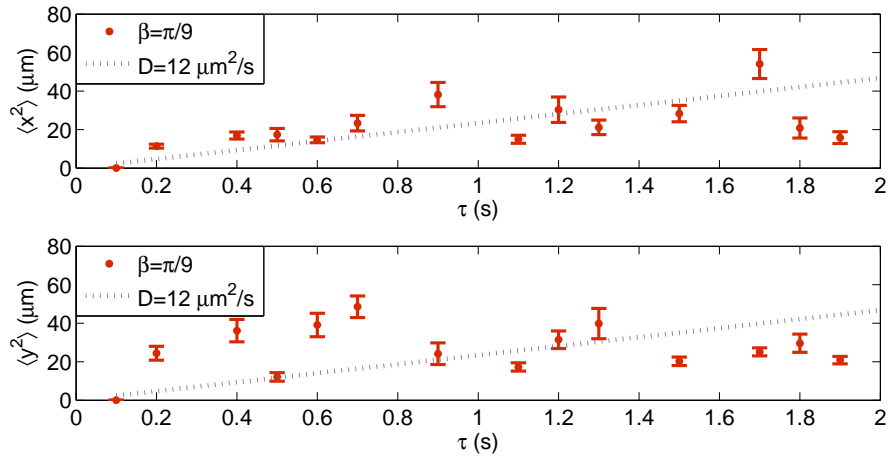


Figure 3.10: The mean square displacements $\langle x^2 \rangle$ and $\langle y^2 \rangle$ of diffusive bead traces near the surface in SW-TIRF ($N=7$). The error bars are SEM and $\beta = \pi/9$. An example of such a trace is shown in figure 3.9a. The dotted line corresponds to free diffusion.

Results

Figure 3.9 shows the two investigated SW-TIRF evanescent fields with different β , i.e., angles between the incoming plane waves. Hence, different periods of SW. Traces of diffusive particles are overlaid the intensity images. Several traces like these are analyzed and the mean square displacements $\langle x^2 \rangle$ and $\langle y^2 \rangle$ are shown in figure 3.10 and figure 3.11 for $\beta = \pi/9$ and $\beta = \pi/15$, respectively.

The mean square displacement in one direction is related to the diffusion

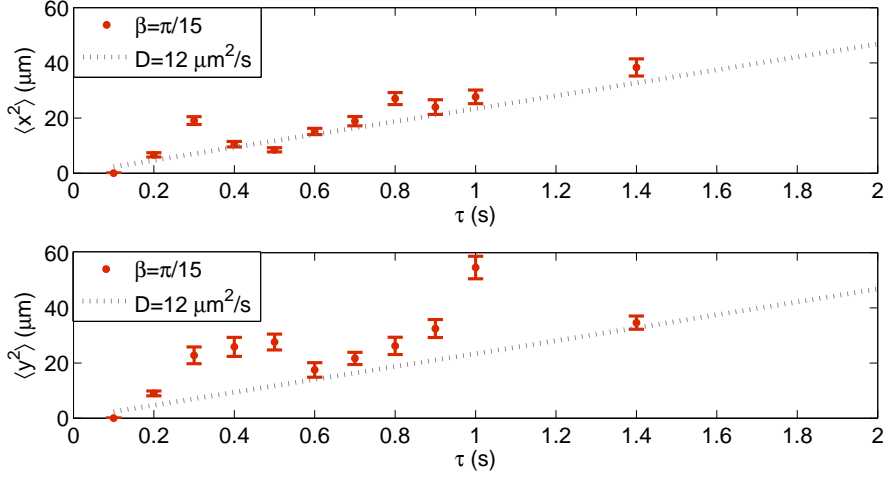


Figure 3.11: The mean square displacements $\langle x^2 \rangle$ and $\langle y^2 \rangle$ of diffusive bead traces near the surface in SW-TIRF ($N=12$). The error bars are SEM and $\beta = \pi/15$. An example of such a trace is shown in figure 3.9b. . The dotted line corresponds to free diffusion.

constant D [91]:

$$\langle x^2 \rangle = 2D\tau \quad (3.40)$$

where τ is the elapsed time. The diffusion of a spherical particle in a viscous medium is:

$$D = 6\pi\eta a \quad (3.41)$$

here η is the dynamic viscosity which is $1.002 \cdot 10^{-4}$ Pa·s for water at 20° C. So for the beads investigated here ($a=180$ nm); $D_{bead}=12 \mu\text{m}^2/\text{s}$. The resulting mean square displacement is calculated from equation (3.40) and shown in figures 3.11 and 3.10 (dotted lines).

From the equipartition function we have that:

$$\frac{1}{2}\kappa\langle x^2 \rangle = \frac{1}{2}k_{\text{B}}T \quad (3.42)$$

where k_{B} is Boltzmann's constant and T is the temperature. This is used to estimate the trapping strength κ in the x -directions, i.e., perpendicular to the wavefront. In the case where a bead would be trapped in the region of high intensity, a typical excursion would be as follows: On short time scales the bead would diffuse freely and at longer timescales it would feel the borders of the confinement. Thus $\langle x^2 \rangle$ would become constant with the value $k_{\text{B}}T/\kappa$. The bead would be most confined in the SW with the smallest period and

the steepest force gradient. Hence, κ should be largest for the results shown in figure 3.10 ($\beta = \pi/9$).

Ideally, the data points of $\langle y^2 \rangle$ would be scattered above the line of free diffusion. This would show that the diffusion in the y -direction; i.e., along the wavefront, would be larger than D_{bead} . In other words, that the bead is pushed in the direction along the wavefront; as argued for theoretically in the previous sections.

The results shown in figures 3.10 and 3.11 can not conclusively determine whether the polystyrene beads are affected by SW-TIRF or not. Therefore, more care must be taken to get experimental results that can detect the possible confinement and super-diffusive behavior of the beads in the evanescent field. While the diffusion of the bead is very fast, a higher time resolution should be acquired. For this purpose an ultrafast camera is needed.

3.5 Conclusion

The intensity of a standing wave evanescent field has been investigated and by integration and decomposition of the force, expressions for the gradient and the scattering forces are found. From the gradient force we predict that there is confinement in the direction perpendicular to the wavefront, as well as, the direction perpendicular to the surface. In addition, we predict that the scattering force results in super-diffusivity along the wavefront.

Numerically the forces have been calculated and trapping efficiencies reported as functions of the refractive index as well as the radius of a dielectric sphere in the evanescent field. From this it is shown that with the right set of experimental parameters, the gradient forces will confine a particle in the most intensive part of the SW-TIRF. At the same time, scattering forces will push the particle along the wavefront. A system, as described here, would be applicable for all kinds of active rheology where spherical particles can be used as force transducers to probe the viscous properties of cells and polymers for instance.

These theoretical results should be compared with experimental data. Therefore, a method for this comparison is sketched. For this purpose some initial experiments are reported and the diffusive behavior discussed. It should, therefore, be straightforward to use this as the basis for a careful comparison of experiments and the theoretical results derived in this chapter.

CHAPTER 4

Optical trapping of quantum dots

In recent years quantum dots have found all kinds of applications both in biophysical assays as well as in quantum optics and quantum photonics. The work presented here characterizes quantum dot's properties as force transducers. Andrew Richardson participated in this project.

4.1 Introduction

As described in section 1.4 optical tweezers are used to trap and manipulate particles and probe and exert forces in the pN range. These particles are most often micron-sized dielectric particles. However, recently a lot of effort has been put into trapping nano-particles [92] and there are several reports on optical trapping of nano-meter sized metallic particles [31, 93, 94, 95], nano-rods [96], and nano-wires [97].

In 2007 Lingyun Pan and co-workers reported 2D optical trapping of colloidal QDs [98]. They used a very focused pulsed laser to form an aggregate of QDs on a glass substrate. However, they claimed that to trap QDs with a continuous wave (CW) laser one would need laser powers on the order of 20 W. Here we report that 3D optical trapping of individual QDs, as sketched in figure 4.1, is possible for laser powers down to 0.1 W. Furthermore, we find the strength of the optical trap and, thus, the magnitude of the optical forces acting on a single QD. Moreover, we discuss the possibilities for establishing a technique that combines force transduction and fluorescence of QDs.

The first part of this chapter, section 4.2, described the technical requirements and necessary changes to the existing optical tweezers setup. In section 4.3 it is shown that we used two independent approaches to render probable

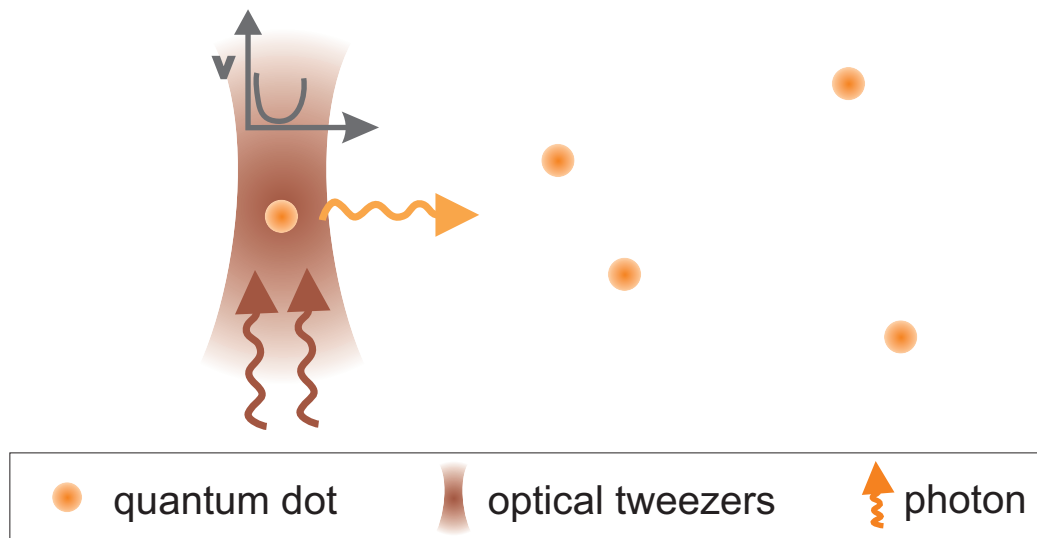


Figure 4.1: A sketch of optical trapping of a QD. The QD absorbs two photons from the near-infrared laser (wavelength of 1064 nm) and emits a photon (wavelength 605 nm).

that we were trapping individual QDs and not aggregates. We measured the trapping strength of different QDs and estimated the polarizabilities; as shown in section 4.4. At last in section 4.5, we report two-photon excitation in the optical trap.

4.2 Combining fluorescence microscopy and optical tweezing

These experiments require an optical tweezer setup that allows for simultaneous trapping and fluorescence microscopy. Therefore, some changes had to be performed on the existing setup (II) in the optical tweezers laboratory at the Niels Bohr Institute. Andrew Richardson and Nader Reihani contributed with very helpful advice.

The setup is based on a Nd:YVO₄ laser (5 W Spectra Physics Millennia, $\lambda = 1064$ nm, TEM₀₀) implemented in an inverted Leica microscope equipped with a mercury (Hg) lamp for QD excitation. Furthermore, a quadrant photodiode (S5981, Hamamatsu), allows for precise position detection with a time resolution of ms [99]. All in all, a setup that resembles the one described in [93, 100, 101].

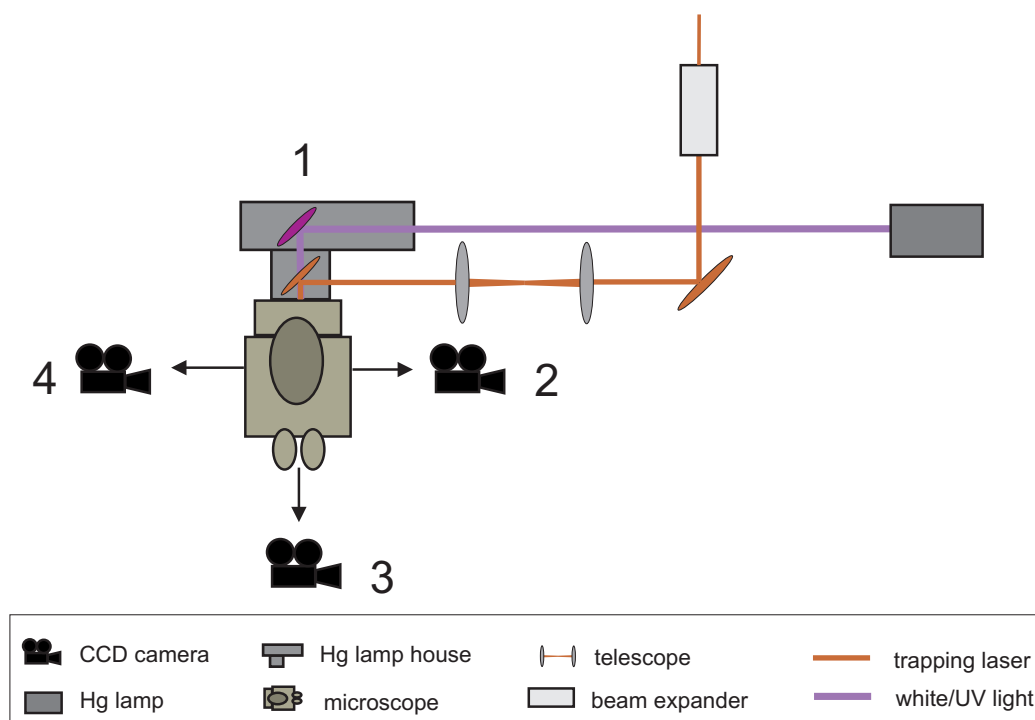


Figure 4.2: The configuration of the setup that enables simultaneous fluorescence microscopy and optical tweezing. Both the laser beam and the fluorescence light enters the microscope from the back (port 1) so that they are reflected to the sample simultaneously. Note that three ports are used for imaging of the sample: Confocal microscopy (TCS SP5, Leica - port 4), ordinary CCD camera (port 2) and a cooled EMCCD camera (Ixon, Andor - port 3). For further information of these setup changes, see appendix B.

Some changes were performed to allow for simultaneous trapping and fluorescence microscopy: The laser beam and the light from the Hg lamp are both entering the microscope from the back, or port 1 in figure 4.2. To enable this, some micro-electronic components had to be removed from the optical path. In addition, a custom made filter cube (Leica HQ420/40x+1064, z440/1065rpc, HQ605/40m-2p) was inserted. This reflects both the trapping beam ($\lambda = 1064$ nm) and an intense part of the Hg spectrum ($\lambda = 420$ nm) and transmits the emitted light of QDs. So both the laser and the fluorescence light enters the sample from the same port.

High sensitivity camera

For visualization and tracking of fluorescent marker particles or proteins high sensitivity cameras are useful. When changing the setup to do fluorescence imaging and trapping at the same time, a cooled electron multiplying charged coupled device (EMCCD) (Ixon, Andor) was inserted in port 3, see figure 4.2. The collected light is either send to the eyepieces or to the high sensitivity EMCCD. The function of this charged coupled devise can be summarized in three steps.

Firstly, the picture is collected in an array of capacitors. In short, the photons collected from the sample causes the array to accumulate charges proportional to the amount of photons hitting the capacitors. Then the charges of each capacitor shifts to the neighboring capacitor and so forth until the charge is sent from the last capacitor in the array to an amplifier.

Secondly, the charge is amplified by electron multiplying the charge in a way similar to an avalanche diode as found in the quadrant photodiode of the setup [102, 103]. This is special for the EMCCD and to minimize the thermal noise from being amplified the CCD chip is cooled to -80 C° .

Thirdly, this charge is converted into a sequence of voltages that, afterward, is digitized to create intensity images.

4.3 Three-dimensional optical control of individual quantum dots

In this section it will be shown that it is possible to optically trap individual QDs. To render probable that indeed there is only one QD in the trap, we use two different approaches. The first, relies on the photo-diode signal and the second on the fluorescence blinking of QDs; described in section 1.4.

An inducible dipole in an inhomogeneous field experiences a force in the direction of the field gradient, the gradient force, \mathbf{F}_{grad} . A particle with an induced dipole moment will be forced toward the laser focus by this 3D restoring force. Hence, the existence of an induced QD dipole moment is essential for optical trapping. Opposing the gradient force are the scattering force, \mathbf{F}_{scat} , and the absorption force, \mathbf{F}_{abs} , which are proportional to the scattering and absorption cross-sections, respectively, as described in chapter 3. We use an infrared laser light, with a wavelength that exceeds the maximum emitted wavelength of the QDs by far for trapping, see figure 1.1. In addition, the QDs are physically very small in comparison to the focus area of the trapping laser light. Thus, the scattering and absorption forces are considerably smaller than the gradient force [104]. We use this knowledge to estimate the polarizability of an individual QD.

4.3.1 Methods

The experiments described in this section were performed with Andrew Richardson.

We used water-soluble cadmium-selenide (CdSe) core zinc-sulfide (ZnS) shell QDs with an emission wavelength of 655 nm (Invitrogen). The QDs were diluted $1/10^5$ in 50 mM Sodium Borate (pH 8.2) with 1% Bovine Serum Albumin (BSA). This solution was filtered to remove aggregates of QDs and BSA and perfused into the chambers. Afterward, the chambers were sealed with vacuum grease. For more details see appendix D.1.

The laser was focused to a diffraction limited spot with an oil immersion objective (HCX, PL, APO, 100 \times , NA = 1.4 oil CS). We only consider the directions perpendicular to the propagating laser and, therefore, do not take the spherical aberrations into account. Moreover, the experiments are done close the cover slip, in a depth of 3 μm , where the aberrations are small. To minimize the aberrations further one can use the technique developed by Reihani and Oddershede [105] as done in section 4.4. While the appropriate oil, in this case, fluoresced we did not use this technique. However, recently

we realized that non-fluorescent oils are available. The laser power was 0.525 W and approximately 20 % of this reached the sample. In order to increase the likelihood of trapping only a single QD at a time we used a very dilute concentration of QDs. Once the experiment was initiated we typically had to wait for ten minutes before a QD would randomly diffuse into the optical trap. The presence of a QD in the trap was clearly visible from reading the voltage signal from the quadrant photodiode collecting the forward scattered laser light. To record and analyze the emission from the QDs we used the EMCCD camera to collect stacks of intensity images; see appendix D.1.

For experiments where the QDs were specifically attached to a biotinylated coverslip, we used similar QDs as described above but with a streptavidin-coating (Invitrogen). The coverslips of the chambers were biotin-coated by incubating the samples overnight with BSA-biotin (Sigma) in 20 mM Na_2HPO_4 , 150 mM NaCl (pH 7).

4.3.2 Results

The positions visited by the QD performing Brownian fluctuations in the optical trap were found as described in References [93, 94, 99]. The histograms of the resulting time-series are shown in figure 4.3, the full lines are Gaussian fits to the position distributions. After approximately 20 minutes the time-series broadened, after an additional 10 minutes it broadened even further, and at later times the broadening continues. Previous experience from trapping gold nanoparticles [94] suggests that the broadening of the time-series is a result of additional particles entering the trap. Hence, in a typical experiment we would have a single QD at least 10 minutes before more QDs entered the trap.

As a second and independent way to render probable that we only had a single QD in the trap we performed an experiment to visualize the blinking of a trapped QD. As earlier described [107], this can be investigated by analyzing intensity image sequences of the fluorescence blinking. However, a QD in the optical trap performs considerable Brownian motion within the trap. This complicates visualization of a trapped QD, and it would be difficult to rule out that an observed blinking is not an effect of the QD leaving and entering the focal volume rather than blinking. Actually, we tried to observe individual QDs in the trap by their fluorescence blinking. However, the light we collected from the trap focus could not be distinguished from scattered laser light in an empty trap. Therefore, we performed an experiment where a streptavidin-coated QD was first trapped and subsequently moved to a biotinylated surface, where it would bind specifically. Figure 4.4a shows a

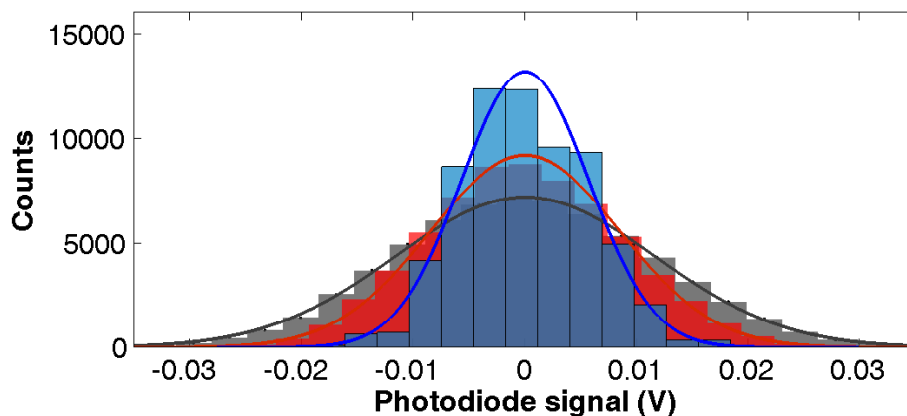


Figure 4.3: A time series of voltages corresponding to positions visited by QDs in the optical trap; measured by the quadrant photodiode. Parts of a long time series is chosen to show the discrete steps. The histogram in the front (blue) is the distribution of voltages or positions of a single QD in the trap. The histogram behind this (red) is the distribution of at least 2 particles and in the back (gray) is the distribution of 4 or more particles in the optical trap. It is seen that the signal broadens as more QDs enter the trap. For simplicity only three time intervals is included in this figure but more intervals are shown in Reference [106].

picture of the cover slide surface before the QD was attached, and figure 4.4b shows the same area after the trap with the QD has been lowered and the QD has attached to the surface. Figure 4.5a shows the corresponding temporal evolution of the intensity from the attached QD. A clear blinking behavior was observed, thus signifying that there was only one QD in the optical trap. Supporting this, figure 4.5b shows the distribution of the intensities with distinct *off* and *on* like in figure 1.4.

For positions visited by an optically trapped particle, it is well established that the optical tweezers exert a harmonic force on the trapped particle: $\mathbf{F} = -\kappa\mathbf{x}$, where κ denotes the trap stiffness and \mathbf{x} is the position of the particle with respect to the center of the trap. To quantify κ and hence find the range of optical forces exertable on a QD we performed a power spectral analysis of the time series using the routines described in Reference [108]. The distance between the QD and the cover slide surface was very large in comparison to the radius of the QD, and we approximated the overall shape of the QD to a sphere. Hence, the drag coefficient, γ , can be found by Stokes law, $\gamma = 6\pi\eta d$, where d is the effective diameter of the QD.

The equation of motion of a particle performing Brownian fluctuations

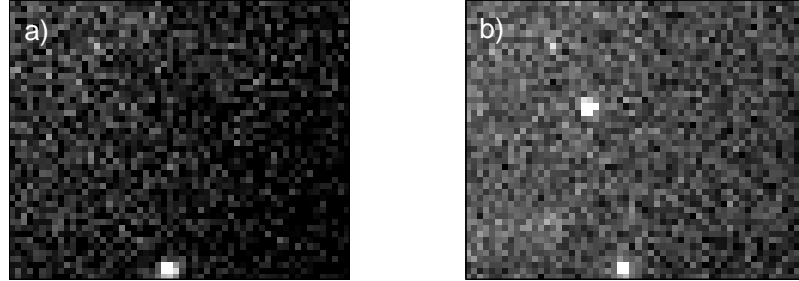


Figure 4.4: Pictures of a biotinylated surface under the optical trap. a) shows the surface before a streptavidin-coated QD is trapped (another QD is attached to the surface). b) shows the same part of the surface after lowering a trapped streptavidin-coated QD until it attaches the surface. The exposure time is 1.8 seconds thus integrating over several *on* states of the QD.

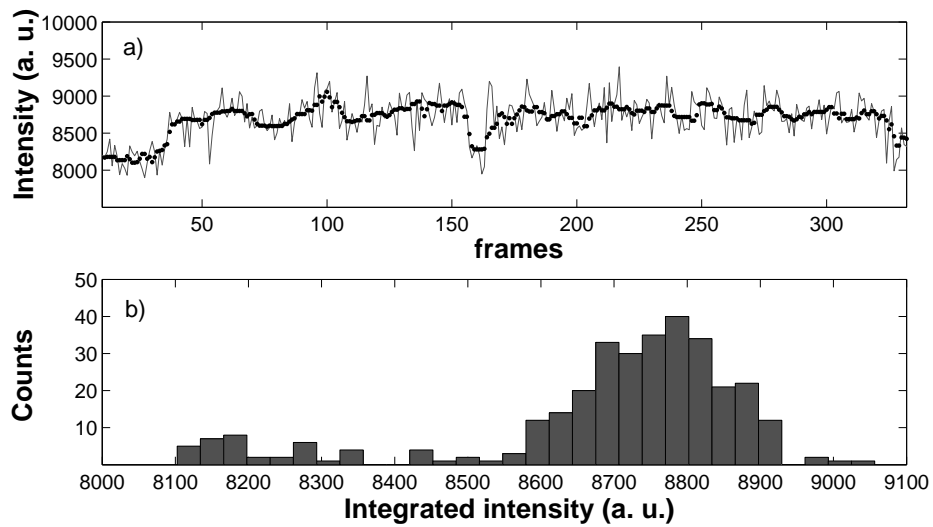


Figure 4.5: The intensity fluctuation of the attached QD shown in figure 4.4. a) Time evolution of the intensity. All data points (continuous line) as well as the average from from a sliding window of 10 data points (dots) are shown. b) The corresponding intensity distribution histogram shows two peaks indicating blinking of the QD.

inside an optical trap is given by the Langevin equation. A Fourier transformation of the Langevin equation gives a positional power spectrum:

$$P(f) = \frac{k_B T}{\gamma(f^2 + f_c^2)}, \quad (4.1)$$

where γ is the drag coefficient. This follows a Lorentzian function. The frequency in the power spectrum which distinguishes the plateau region of slow fluctuations and the slope of -2 which signifies Brownian motion for rapid fluctuations is denoted the corner frequency, f_c . The corner frequency is related to κ and to γ on the QD: $f_c = \frac{\kappa}{2\pi\gamma}$. Figure 4.6 shows an example of the power spectrum of positions visited by a 585 nm QD in one lateral dimension, the full line shows a fit by a Lorentzian function taking into account aliasing and the filtering effects of the quadrant photo-diode system [102, 108]. The inset in figure 4.6 shows that positions visited by the QD inside the optical trap follow a Gaussian distribution (full line).

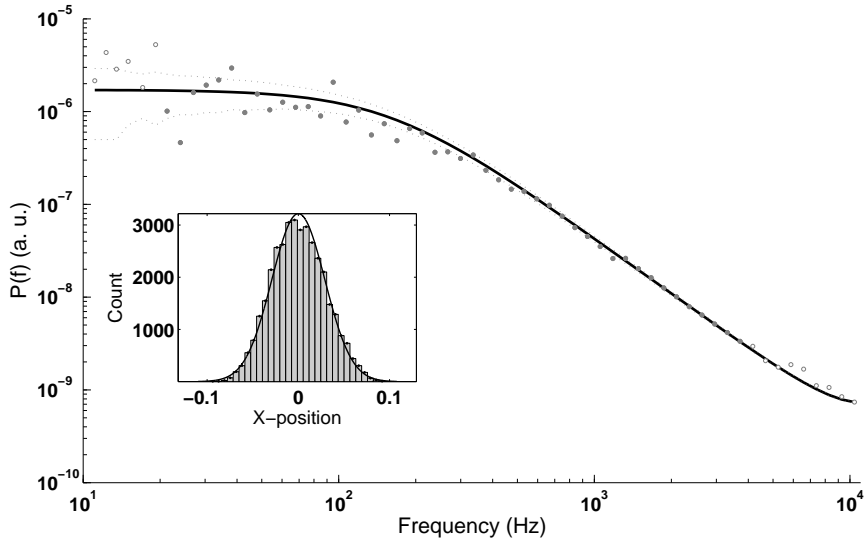


Figure 4.6: Power spectrum of the lateral positions visited by an optically trapped QD (wavelength of 585 nm). Full line is a Lorentzian fit to the data [108], punctuated lines represents STD. The corner frequency f_c of the Lorentzian fit is (159.3 ± 6.5) Hz. The inset shows the distribution of positions visited by the QD in the optical trap for the same time series, full line is a Gaussian fit.

Estimate of the polarizability

As colloidal QDs have only been available for the last 20 years, many properties are still unknown. Simple questions regarding e.g., the absolute magnitude of the dipole of a QD, or regarding index of refraction of a QD still remain unanswered. To estimate the polarizability of a single QD we assumed that the laser beam intensity profile is Gaussian in the two lateral directions and given by σ ; two times the distance from the beam axis where the intensity drops to $1/e^2$ of the maximum intensity. We term it the width of the beam:

$$I = I_0 e^{-(x^2+y^2)/2\sigma^2}. \quad (4.2)$$

The total power, P , delivered by the laser in the sample equals the integrated intensity:

$$P = \int_{-\infty}^{\infty} I dx dy = I_0 2\pi\sigma^2. \quad (4.3)$$

In one dimension the gradient force is [104]

$$\mathbf{F}_{grad} = \frac{\alpha}{2} \nabla(\mathbf{E}^2), \quad (4.4)$$

where α is the polarizability. \mathbf{E} is the electric field, and is related to the intensity by:

$$|\mathbf{E}|^2 = 2I/c\varepsilon, \quad (4.5)$$

where c is the speed of light and ε the electric permittivity of the medium. We used the wavelength dependent permittivity of water for a wavelength of 1064 nm, $\epsilon = 1.32^2$ [109]. Here $\epsilon = \varepsilon/\varepsilon_0$, where ε_0 is the permittivity in vacuum.

As argued for in the preceding, the contributions of \mathbf{F}_{scat} and \mathbf{F}_{abs} are very small in comparison to the contribution of \mathbf{F}_{grad} [104]. Therefore, we approximate $\mathbf{F} = -\kappa\mathbf{x} = \mathbf{F}_{grad}$. However, in section 4.5 this will be discussed in more detail.

From our knowledge of P and κ we can use the above equations to find the polarizability, α , by combining equations (4.2), (4.3), (4.4), and (4.5) and Taylor expanding for small x while comparing equation (4.4) to $\mathbf{F}_{grad} = -\kappa\mathbf{x}$. We obtain:

$$\frac{\alpha}{\varepsilon_0} = \frac{2\pi c \kappa \epsilon}{P} \times \sigma^4 \quad (4.6)$$

Here, σ is approximated by half of the radius of the laser beam at the trap center [104], $\sigma \sim 250$ nm. α is proportional to σ^4 and the resulting polarizability is, therefore, very sensible to the estimate of this parameter.

In contrast, the polarizability of a dielectric sphere can be calculated by the Clausius-Mossotti relation as mentioned in section 3.2.2. For this purpose

we assume the CdSe core of the QD to be approximately spherical with a diameter, d . ϵ is the square of the refractive index and $\epsilon_{CdSe} = 2.56^2$ for CdSe [110]. We have:

$$\frac{\alpha}{\epsilon_0} = 3V \frac{\epsilon_{CdSe} - \epsilon}{\epsilon_{CdSe} + 2\epsilon}. \quad (4.7)$$

Again this value is very sensitive to the choice of d [106]. This will be discussed in more detail in section 4.4.2, where α/ϵ_0 is found for many different sizes of QDs and compared to the values calculated from equation (4.7).

4.3.3 Discussion

It would be more correct to calculate the value of α by adding the contribution of a couple of ZnS-mono-layers and the relevant polymer-coating. However, in figure 4.10 the theoretically found values of α are found by assuming the total volume of the QD to consist of CdSe ($\epsilon = \epsilon_{CdSe}$). Hence, this can be regarded as the upper limit of the value of α ; calculated from the Clausius-Mossotti relation.

All the above calculations build on the assumption that it is reasonable to consider the QD to be a Rayleigh particle. However, in section 4.5 it is reported that the QDs absorb photons in the optical trap through two-photon absorption.

4.4 Dependence of trapping efficiency on quantum dot size

It is important to correctly choose the QD such that it matches the given experimental goals and conditions, e.g., available excitation lasers and filter cubes. Therefore, we set out to investigate whether the optical trapping properties of QDs would vary as a function of emission wavelength or size and hence be a parameter to consider for optical manipulations. Thus, the aim of this section is to quantify the trapping strength κ of individual colloidal QDs with different emission wavelengths λ (from 525 nm to 800 nm) and different physical sizes, with the result that these diverse QDs have almost identical trapping capabilities.

Table 4.1 summarizes the physical characteristics of the QDs used in the present study. All QDs were bought from Invitrogen who also provided the informations shown in table 4.1 [111]. As a check on the external dimensions

and the quality of the stock we also made transmission electron microscopy (TEM) pictures of the QDs, examples are shown in Figure 4.7. In general, we found the size distributions to be reasonably uniform and in agreement with the values stated by Invitrogen. It is noticeable, however, that the 655 nm appears elongated as mentioned above. Furthermore, the polarizability α is estimated for these different QDs as sketched in section 4.3.2.

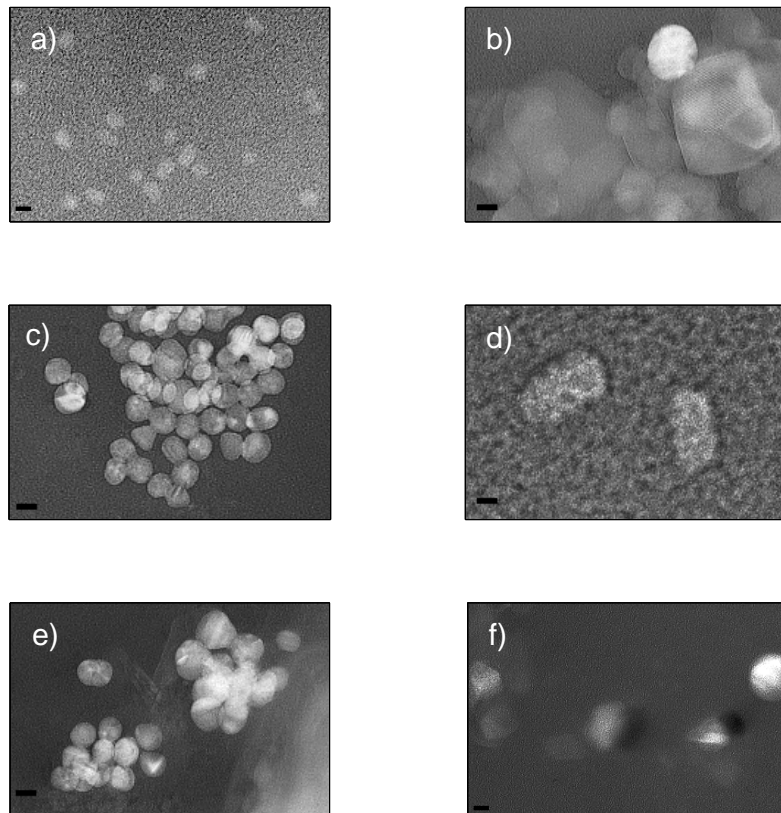


Figure 4.7: TEM pictures of a) 525 nm QDs, b) 585 nm QDs, c) 605 nm QDs, d) 655 nm QDs (note the elongated shape), e) 705 nm QDs, f) 800 nm QDs. The scale bars corresponds to 10 nm.

α	core [nm]	composition	d [nm]	d (TEM) [nm]
525 nm	3-4	CdSe/ZnS	13	10 ± 2
585 nm	5.3	CdSe/ZnS	15	26 ± 12
605 nm	(4×9.4)	CdSe/ZnS	16	13 ± 1
655 nm	(6×12)	CdSe/ZnS	20	$(40 \pm 5) \times (24 \pm 3)$
705 nm	ND	CdSeTe/ZnS	20.5	16 ± 3
800 nm	ND	CdSeTe/ZnS	21	21 ± 3

Table 4.1: Physical characteristics of investigated QDs. First column gives α , second column the size of the core region which is given by the diameter if the QDs are spherical or by the semi-major and semi-minor axes where the QDs are more ellipsoidal, third column states the material composition, and the fourth column gives the diameter d of the core plus shell plus polymer coating [111]. The last column gives the outer diameter d as measured by TEM. ND is not determined.

4.4.1 Methods

A variety of water-soluble streptavidin-coated QDs (Invitrogen) with emission wavelengths 525 nm, 585 nm, 605 nm, 655 nm, 705 nm, and 800 nm were used for the experiments. The QDs are stabilized with an outer layer of polymers and PEG [111]. The polymer layer lowers the toxicity, reduces blinking, and seems to have little effect on the brightness [49]. As described in section 4.3.1, QDs were diluted $1/10^5$ in 50 nM Sodium Borate (pH 8.2) with 1% Bovine Serum Albumin (BSA).

The laser was focused to a diffraction limited spot by an oil immersion objective (HCX PL Apo, 63×, NA=1.32, ∞ , 0.17). To minimize the influence of nearby surfaces the trap was located approximately $5 \mu\text{m}$ from the lower cover slide surface. To maximize the strength of the optical trap in the axial direction when individual QDs were trapped we used an immersion oil with a refractive index of $n=1.54$ (Cargille), which efficiently canceled spherical aberrations at a depth of $5 \mu\text{m}$ [105].

4.4.2 Results

For each type of QD f_c was found for more than 20 different individual QDs, the laser power always at 0.1 W at the sample. Figure 4.8 shows f_c as a function of emission wavelength, one point denotes one measurement in order to demonstrate both the position of the majority of the data points and the outliers. However, there is no apparent correlation between the corner frequency and the emission wavelength.

Figure 4.9 shows the trap stiffness, κ , as a function of d . The value of κ

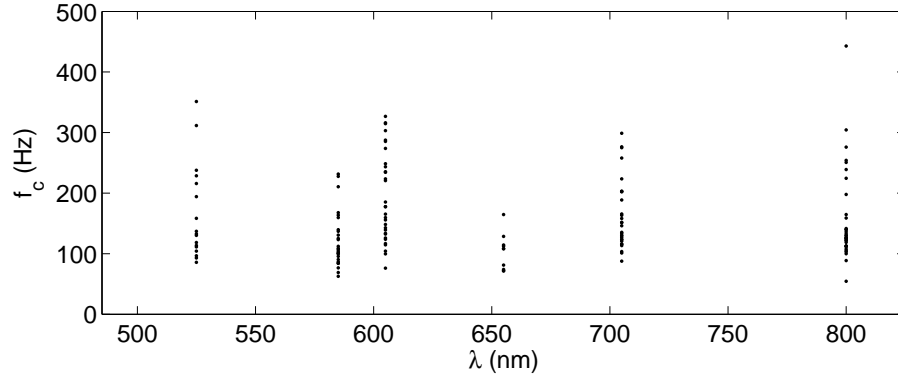


Figure 4.8: Corner frequency versus QD emission wavelength. Each data point denotes the mean of 5 fitted f_c 's of independent time traces for the same trapped QD.

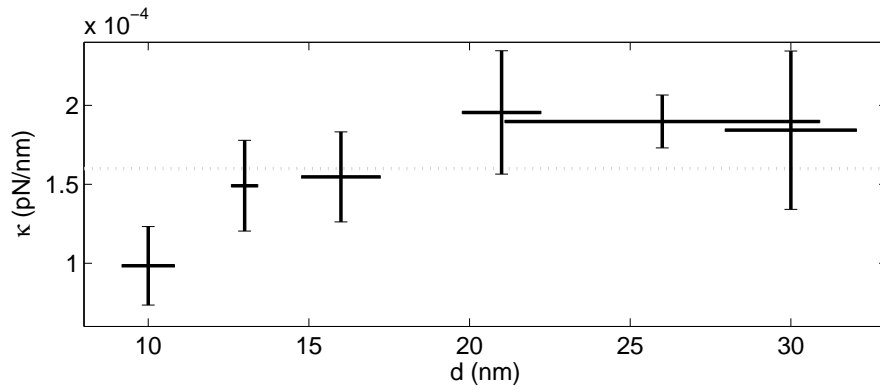


Figure 4.9: Trapping strength dependence on diameters. The points denote the mean of the data points calculated with d as measured by TEM (in the case of the elongated 655 nm QD $d \sim 30$ nm). All error bars denote one SEM and the punctuated line is the mean value of κ .

is calculated from the experimentally found f_c 's and the diameter, d , of the QD as given in table 4.1. For κ as a function of d , given by Invitrogen, see Reference [112].

The trap stiffness is nearly constant within the actual size range, independent of λ and d , with the average value $\kappa = (1.6 \pm 0.4) \times 10^{-4}$ pN/nm (mean \pm STD). This number is the same regardless of whether the Invitrogen or TEM determined values for d are used and it coincides with the value reported for an individual 655 nm QD in Reference [106]. However, figure 4.9 shows that κ is largest for the larger QDs in the investigated range. This is supported by a Students t-test of the κ 's of the smallest and the largest

QD.

From the experimentally found values of d , the polarizability is determined as sketched in section 4.3.2. In figure 4.10 the experimentally estimated values of the polarizability α , from equation (4.6), are compared to the values calculated from equation (4.7). The result is that the experimentally and theoretically found values of α , approaches each other for larger QDs.

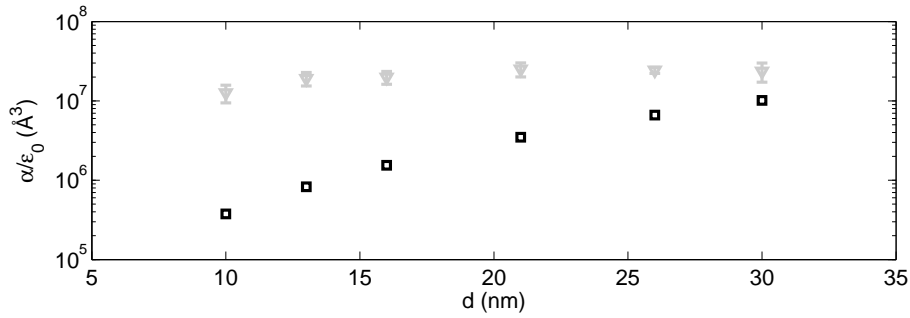


Figure 4.10: Polarizability versus diameter of the QDs. The gray triangles denote the values estimated from our experimentally found κ , equation (4.6), and the error bars denotes one SEM. The black squares are the values calculated from the Clausius-Mossotti relation; equation (4.7).

4.4.3 Discussion

We investigated the optical trapping strength κ as a function of size of the QDs and revealed a small size dependency. This is in accordance with expectations since it resembles what is seen for gold and silver nanoparticles with d in the range from 10-200 nm [93, 94]. Therefore, it could be that this tendency would be more pronounced for larger size ranges of the QDs.

The value of κ obtained for a QD can be compared to that obtained from optical trapping of silver and gold nanoparticles of similar sizes [93, 94]. To this end, κ should be normalized by P (~ 0.1 W), and we find that κ/P resembles the values obtained for gold and silver [93, 94]. Therefore, the induced dipole of a QD is the same as similarly sized metallic nanoparticle.

In literature only little quantitative information regarding polarization of individual QDs is available. However, the polarizability has been measured for considerably smaller CdSe QDs (radius 2 nm) [113] to be on the order of 10^4 \AA^3 and to be strongly dependent on volume, hence, this value could be in accordance with our findings.

4.5 Two-photon quantum dot excitation in the optical trap

Individual colloidal QDs can be optically trapped and manipulated by a single infrared laser beam as shown above and reported in [106]. Here we show that the relatively weak CW trapping laser light can act as a source for two-photon excitation of the trapped QDs, thus eliminating the demand for an excitation light source in addition to the trapping laser beam.

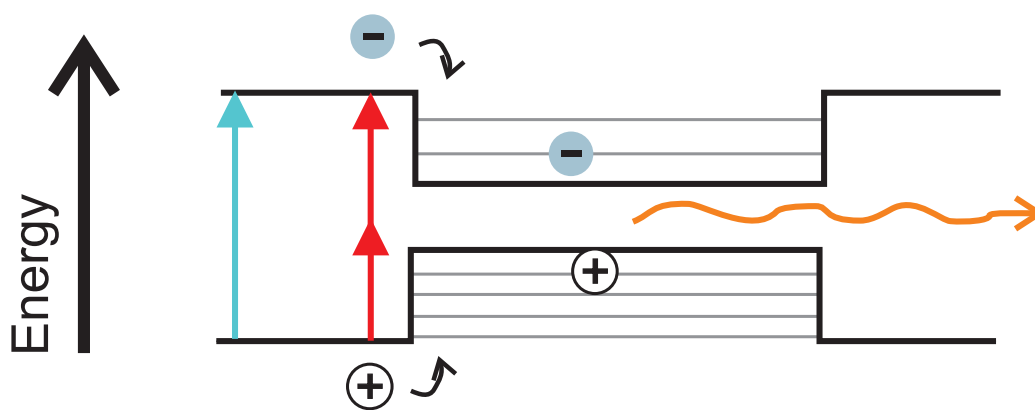


Figure 4.11: Excitation of a QD. The Black line signifies the bandgap of the semiconducting materials and the gray lines are the discrete energy states. (-) and (+) are the electron-hole pair of an excited QD. The QD can be excited by both linearly (blue arrow) and through two-photon absorption (two red arrows).

In general, a fluorescent molecule can become excited if it simultaneously absorbs two photons, and if the energy difference between the ground and excited state of the molecule corresponds to the added value of the energies of the two photons. Two-photon absorption is significantly less likely to occur than absorption of a single photon, the energy of which matches the energy difference between the ground and excited state of the fluorophore. Observations of two-photon absorption by colloidal QDs are relatively sparse, but it has been experimentally shown that QDs have the capability to become excited by a two-photon absorption process [114, 115], with a two-photon absorption cross section which is large in comparison to other fluorophores used in multi-photon microscopy [49, 98, 116, 117].

Here, we report that QDs can be two-photon excited by absorbing photons from the infrared laser; which simultaneously traps the QDs. One important difference between this and earlier work is that previous reports on two-photon absorption of colloidal QDs were performed with pulsed lasers, and

here we show that two-photon absorption can even be accomplished by a relatively weak CW laser. We find that optically trapped QDs excited by the trapping laser light bleach more slowly than if the optically trapped QDs in addition are excited by an Hg lamp. So our results show that only a single laser is necessary to achieve both trapping and fluorescence of QDs.

4.5.1 Methods

For these experiments we trapped aggregates of QDs. We used a (Leica HCX PL APO 100 x NA=1.4 oil CS) objective and the corresponding non-fluorescent immersion oil (Leica with $n=1.518$) as described in section 4.3.1. To trap and simultaneously visualize the 605 nm QD we use the custom made filter cube (Leica HQ420/40x+1064, z440/1065rpc, HQ605/40m-2p) which allows the 420 nm light from the Hg lamp as well as the 1064 nm trapping laser light to be reflected up to the sample, but only allows the emitted 605 nm light to be transmitted to the detection camera; see section 4.2. In contrast to the assays described in sections 4.3.1 and 4.4.1 the QDs are only diluted to 10^{-3} and the solution were not filtered as the presence of QD aggregates were desired.

4.5.2 Results

With the filter cube it was possible to simultaneously trap and visualize QDs ($\lambda = 605$ nm), regardless of whether the excitation source was the Hg lamp or the trapping laser alone. The picture shown in figure 4.12a is the emission from an aggregate of 605 QDs trapped by the 1064 nm laser. The Hg lamp is turned off. As there are no photons available with wavelengths below 605 nm, this picture is the first proof of QD excitation mediated by two-photon absorption of the trapping laser light. Figure 4.12b is another optically trapped QD aggregate, but in this picture the Hg lamp is on. Hence, the emitted signal is a result of both one-photon and two-photon excitation.

Traces of the emission signal to noise ratio (S/N) as a function of time for individual aggregates are shown in figure 4.13. The exact number of QDs in one aggregate was not known, but the total intensity at the beginning of the trace probably reflects this number. Individual curves show a stepwise behavior, each step possibly signifying the bleaching of an individual QD in the aggregate. The pictures were taken at a sampling rate of 10/s, thus integrating over several *on* states of the QDs in each frame. The curves in figure 4.12 shows the average values of the emitted intensity as a function of

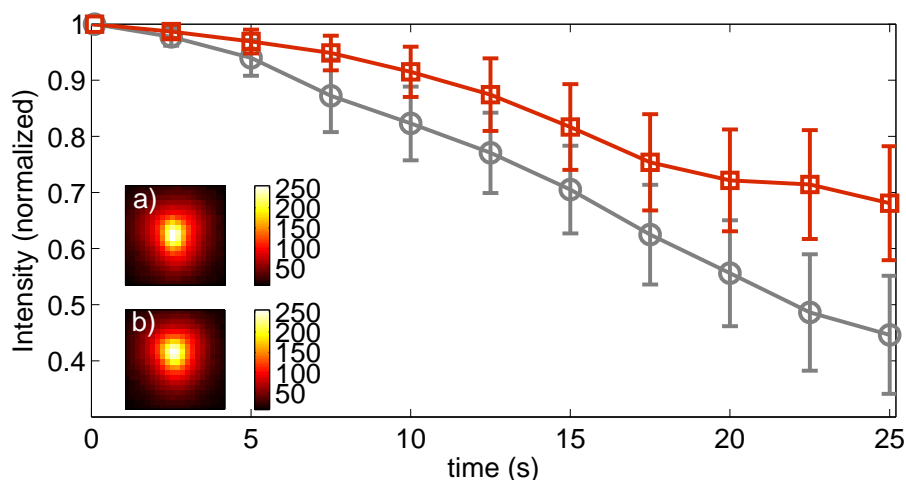


Figure 4.12: Average value of normalized emission from trapped QD aggregates ($\lambda = 605$ nm) as a function of time. Individual traces are shown in figure 4.13. Upper curve (red squares) shows emission with laser on (Hg lamp off). Lower curve (gray circles) shows emission with both laser and Hg lamp on. The intensities are normalized with the initial intensity and error bars denote SEM. Inset a) shows emission from a trapped aggregate (no Hg lamp). Inset b) emission from a trapped aggregate with the Hg lamp on.

time. As the aggregates consisted of a varying number of QDs, the intensity is normalized by the first value. The upper curve (red squares) is the result of two-photon excitation alone (no Hg lamp), the lower curve (gray circles) is the result of both two-photon and one-photon excitation (Hg lamp on). It is clear that the aggregates undergo bleaching over a timescale of 25 s and that bleaching is faster when both two-photon and one-photon excitation takes place.

Interestingly, we did not detect emission from the 525 nm QD while trapped by the 1064 nm laser light (no Hg lamp). This is expected, because two-photon absorption requires the total energy of the photons to be at least equal to the energy, E , corresponding to the emission wavelength, λ , of the QD, $E = \frac{ch}{\lambda}$, where c is the speed of light and h Planck's constant. However, we also did not observe 1064 nm induced emission from a 585 nm QD. This might be because the absorption of this QD is relatively low at 532 nm; as supported by the absorption spectrum of 585 nm QDs shown in figure 1.1. The 605 nm QD and all QDs with $\lambda > 605$ nm have a relatively high absorption of 532 nm light and all exhibit a clear and visible 1064 nm induced two-photon excitation.

To further prove the existence of two-photon-absorption of a QD which

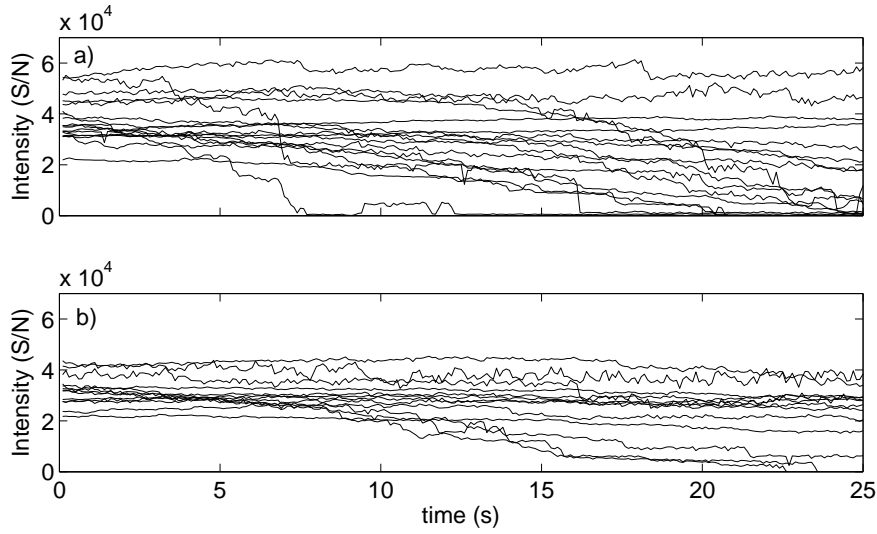


Figure 4.13: Emission intensity from an aggregate of QDs (emission wavelength 605 nm) in an optical trap. a) Emission intensity as a function of time with Hg lamp turned on. b) Emission intensity as a function of time with Hg lamp turned off, the emission being stimulated by two-photon absorption only.

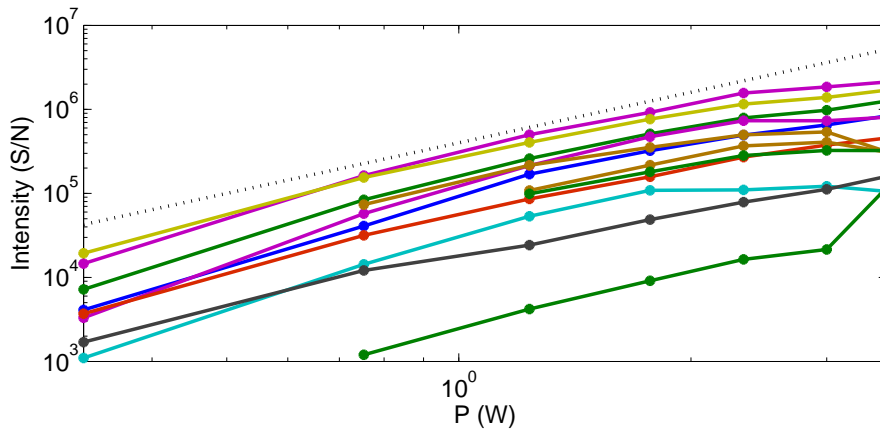


Figure 4.14: Emitted intensity (S/N) versus laser power for individual QD aggregates of varying initial size. The dotted line has a slope of 2.

is trapped by the exciting laser beam we monitored the emitted intensity as a function of laser power, P . For a two-photon absorption the emitted intensity should scale as $\propto P^2$. Figure 4.14 shows the intensity of the emitted light from various trapped QD aggregates as a function of P . The different aggregates have different initial intensities; probably because of their different sizes. Regardless of initial aggregate size, all traces exhibit a scales with a

slope of 2; characteristic of two-photon absorption. However, some of the intensity traces flattens at high laser powers which could be the result of saturated absorption. In other words, that all QDs in the aggregate are turned *on* and there are no QDs to contribute with extra emitted intensity.

As shown in this section QDs absorb the trapping laser light through a two-photon process. This should be taken into account when estimating the polarizability, α , of individual QDs. However, the force resulting from absorption \mathbf{F}_{abs} only has a component in the propagation direction of the laser light and the α 's estimated in this chapter only takes the lateral directions into consideration. Since \mathbf{F}_{abs} does not alter κ in the lateral directions, \mathbf{F}_{abs} does not change α . However, when a QD is excited the polarization is changed and this must affect the trapping strength and, thereby, the polarizability.

Absorption leads to excitation of electrons within the QD, and the electrons in the conduction band are nearly free to respond to an applied electric field [118]. Hence, the third-order non-linear optical properties of CdSe and CdSe/ZnS core-shell QDs in solution give rise to non-linear corrections of the index of refraction [119]. The corrected index of refraction, n_c , can be written

$$n_c = n + \gamma I, \quad (4.8)$$

where n is the linear refractive index and γ is the non-linear refractive index. For CdSe illuminated with a wavelength of $1.06 \mu\text{m}$ γ is found experimentally to be $-1.47 \times 10^{-30} \text{ W}\mu\text{m}^{-2}$ [110]. In the focus where the laser intensity $I = I_0$ we have, from equation (4.3) that $I = P/2\pi\sigma$. From this we have that the corrected refractive index, normalized with n , is:

$$\frac{n_c}{n} \sim 1 + 1.5 \times 10^{-7}. \quad (4.9)$$

Thus the correction is very small compared to the standard deviations of κ and the inaccuracy of σ . Hence, this correction of n is not important for the estimate of α .

It is well-known that for optical trapping of dielectric objects, there is a linear relationship between κ and P . As shown in figure 4.15, this is also true for optical trapping of two-photon excited QDs thus supporting that this nonlinear phenomenon is only a weak perturbation that does not alter trapping properties considerably.

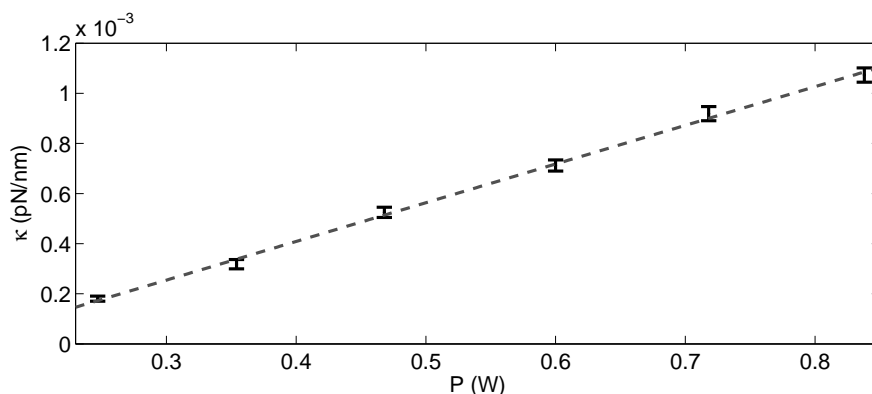


Figure 4.15: Trapping strength versus laser power for individual QDs. The error bars are SEM. The dotted line is a linear fit to the data and it has a slope of $1.5 \cdot 10^{-3}$ pN/nm/W.

4.5.3 Discussion

We have shown that QDs are readily excited through two-photon excitation by a relatively weak CW infrared laser beam which was also used to trap the QDs. This implies that only one CW laser is needed for experiments where QDs are to be used for visualization, manipulation, or force transducers. Another advantage of using a near-infrared laser instead of, e.g., an Hg lamp for excitation is that the bleaching is slower when the QDs are excited only through two-photon excitation. Our results imply that absorption does not need to be taken into account when exact calculations and estimations of the trapping forces are done. In other words, QDs can be considered as simple Rayleigh scatters in an infra-red light field. However, as in all other precise force measurements with optical tweezers, exact force calibration should be done prior to all experiments.

4.6 Conclusion

Colloidal QDs are optimal to visualize biological systems, e.g., as markers for individual proteins [42, 120] or for in vivo studies [43, 49]. In this chapter we provided the most important aspects necessary for the use of QDs as handles for optical manipulation, force transducers, and markers for two-photon fluorescence microscopy.

We have shown three-dimensional optical control of individual QDs using

an infrared CW laser at low laser powers. Analysis of the Brownian motion of trapped QDs, of many different sizes and colors, has allowed us to infer the optical forces applicable on a QD to be on the order of tens of femtoNewton for typical excursions. Additionally, we used the quantitative information regarding the interaction between the electromagnetic field and the QD to calculate an estimate of the polarizability of a colloidal QD. Our findings allow for simultaneous visualization and photonic manipulation of QDs or of molecular systems labeled only with QDs.

Furthermore, we reported two-photon absorption in the optical trap which allows the QD to be used as a single probe particle. The QD can serve both as a handle for manipulation and controlled force transduction and at the same time for visualization through linear as well as two-photon absorption of the trapping laser light.

In section 4.2 the setup used for 3D optical trapping of individual QDs was described. It relies on parallel Hg light and trapping beam and the use of custom made filter cubes to reflect the light into the sample. However, alternative setups could be imagined that did not rely on a filter cube for each color of QD. Instead, the sample could be illuminated with TIRF, as described in chapter 3 or the related method that allows for illumination deeper in the sample [121]. Such an assay would be appropriate for assays with QDs of different colors. However, the knowledge of the two-photon absorption in the trap allows for an even simpler setup with one laser; both for trapping and visualization. In other words, a setup where QDs light up in the dark when trapped.

These results together with the additional information given in section 1.4, provide a basis for experimental design of future investigations using QDs, e.g., for single molecule or nano-scale systems investigations.

CHAPTER 5

RNA polymerase traffic on DNA

The natural path to follow after the characterization of QDs was to consider a biological application. In the application sketched here the QDs are used for visualization not as force transducers. The ultimate goal of the work presented in this chapter, was to track individual RNAPs on the DNA. The DNA traffickers should carry QDs as small torches as they moved along the DNA. To set up such an experiment, RNAPs with an affinity for streptavidin-coated QDs is needed as well as the right geometry for holding the DNA etc. Some of the preliminary investigations is presented in this chapter. Unfortunately, we had some troubles, in particular, with the activity of the RNAP which led us astray. Szabolcs Semsey, Marit Sletmoen from NTU, Trondheim, and Mette Eriksen from the Optical Tweezers laboratory participated in this project.

5.1 Introduction

Biological ensemble assays are often used to determine concentrations of a given biomolecule, e.g., a specific gene transcript, under different conditions. This includes foot-printing, transcriptions assays, and reporter assays; as presented in section 2.2. The drawback of these kinds of measurements is that only average properties are revealed.

To know dynamics and interactions on the molecular level single molecule assays may be favorable. Such investigations are most often simplified *in vitro* versions of the real biological systems. However, they still capture essential components of the biological processes of a wild type system. The strength of these minimal systems is that we can learn about mechanisms that are unsynchronized among the biomolecules. In other words, spatial

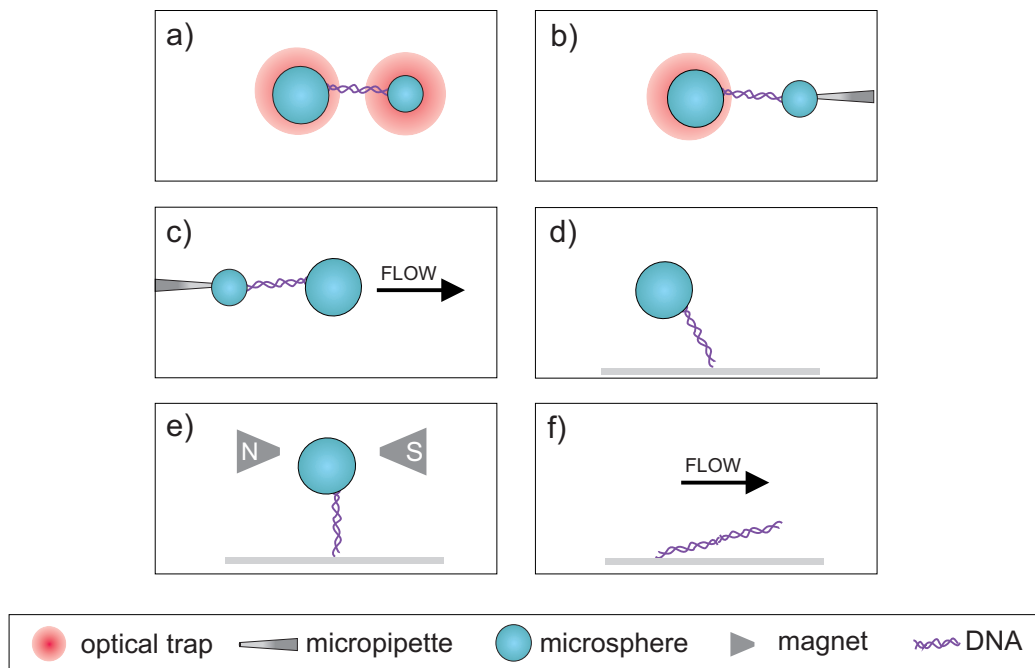


Figure 5.1: Some of the many different geometries of single molecule assays. a) top view of DNA attached to two handle particles (most often micron-sized plastic beads). The DNA is attached to the handles either chemically or through a protein interacting with the DNA. The handles are held by a dual optical trap to measure the forces, e.g., how the DNA is shortened or stretched. b) top view of a similar setup where one handle is attached to the tip of an immobile pipette c) top view of a flow separating the handles. Here the displacement of the handles, which is related to the force, is measured through video microscopy. d) side view of a DNA tethered to a glass cover slip again either chemically or through a DNA bound protein. Movements are investigated through video microscopy. e) side view of a similar setup where the handle is magnetic, the DNA can be coiled or uncoiled to investigate how the torsional stress affects DNA bound proteins. f) side view of a flow forcing tethered DNA to stretch along the surface. Here DNA bound proteins are fluorescently labeled and investigated with fluorescent microscopy; most often TIRF.

and temporal inhomogeneities can be revealed.

The RNAP:RNA:DNA complex is very stable and is, therefore, an excellent candidate for single molecule analysis. The most commonly used RNAPs for single molecule assays are the multi-subunit *E. coli* RNAP and the simpler viral T7 RNAP. The last one is used for the project described in this chapter.

A large variety of geometries have been used to contribute to the knowl-

edge of the movement of a molecular motor and an overview of some of them is given in figure 5.1. The first assays to investigate transcription activity on a single molecule level came from tethered particle motions [34, 122]. Here an RNAP molecule was immobilized onto the surface of a microscope cover slip and a particle (0.2 μm - 1.2 μm) was tethered to the protein through DNA. The DNA was transcribed and the particle was pulled to the surface, as sketched in figure 5.1d. In this case the motion of the particle reflects both the Brownian motions as well as the confinement due to the DNA bound protein. Centroid tracking of the particle can give sub-pixel accuracy (~ 10 nm), however, position measurements with optical tweezers give even better resolution. Furthermore, Brownian noise is reduced by applying an external force, e.g., optical tweezers or magnetic tweezers; see figures 5.1a, 5.1b, and 5.1e. In this way the motion is not tracked passively but significant external mechanical force is applied to the system [11, 123]. These perturbations of the system might complicate data interpretation and a lot of care must be taken to reveal intrinsic properties of the biological system. In recent years, a lot of effort has been put into combining TIRF or related methods, e.g., like the one described in Reference [121], with a geometry as sketched in figure 5.1f. Either in assays where DNA was anchored to the surface by its two extremities (molecular combing) [124, 125] or in assays that used flows to give the same feat.

Micron-sized plastic or glass beads, gold or silver nano-particles, fluorescent beads, fluorophores and QDs are used as reporter particles. These particles have been visualized with microscopes using a variety of modalities, e.g., brightfield, fluorescence microscopy, back-focal plane detection, TIRF, atomic force microscopy, Förster resonance energy transfer etc.

Fluorescence microscopy has been combined with optical trapping for applications like tying knots on DNA [126] or following molecular motors along a filament [127, 128, 129, 130, 131]. In addition the bleaching and other properties of the trap have been investigated [112, 120, 132]. Furthermore, experiments are reported, where the 1D diffusion of enzymes, marked with QDs, are tracked [133].

Here we want to specify the requirements for a system that allows for tracking of individual RNAPs as they travel along DNA. These RNAPs are tracked with individual QDs. The use of QDs facilitates enzyme tracking with high spatial and time resolution [133] with no restriction from photobleaching; as described in section 1.4. Even though the fluorescence blinking leads to gaps in the trajectory it does not affect the measured diffusion [50]. Moreover, the blinking can be used to prove that a specific event only involved a single QD; as discussed in detail in chapter 4. Equipping the RNAP with a QD could cause the measured track to be dominated by the diffusion of

the QD. This is probably the case when the complex is freely diffusing in the media. However, when an RNAP is transcribing the 1D diffusion of the RNAP is found from equation (3.40) and a transcription velocity of tens of bp to be $\sim 10^{-6} \times D_{QD}$, where D_{QD} is the diffusion constant of QDs. Hence, the movements of the RNAP is easily resolved from the movement of the complex when diffusing along the DNA. Therefore with a system like this, we expect that many transcription regulating mechanisms could be investigated.

The requirements for direct observation of individual occurrences of transcription will be discussed in this chapter and the construction of a QD bound T7 polymerase will be presented. Section 5.2 introduces a simulation of RNAP traffic on DNA. This is useful for designing a system appropriate for the investigation of a specific traffic event like collisions between the traffickers. Section 5.3 discuss the thermal noise of DNA extended between two beads. In section 5.4, the construction of an RNAP:QD complex is described and the activity of this complex is measured. Finally in section 5.5 we present the use of QDs as tracker particles in a geometry where DNA is anchored to the surface.

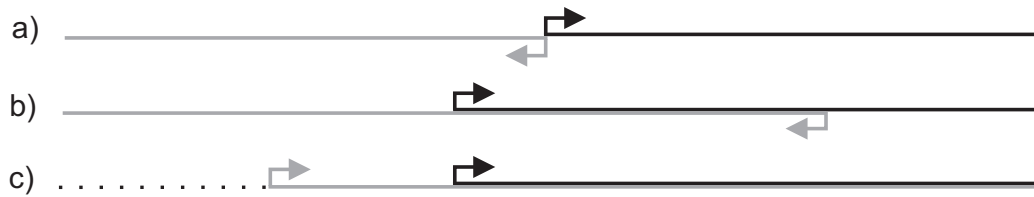


Figure 5.2: The different genetic constellations that leads to interference. The lines denotes genes and the arrows denotes promoters. a) overlapping promoter sequences either convergent, tandem or divergent with transcripts that overlap; at least partially. b) convergent promoters of genes overlapping; at the least partially. c) tandem promoters directed in the same direction; potentially with overlapping transcripts.

5.2 Simulation of polymerase traffic

The traffic along DNA is regulated in many ways and in all the different states of the journey. Most often the initiation is enhanced or hindered; e.g., when a transcription factor binds to its operator site. However, some regulating mechanism affects the transcription process after initiation; like road-blocking, as described in chapter 2, or when the transcription product interferes with the product of another RNAP. In this section effects, resulting from the interference between RNAPs, will be investigated.

Transcription interference

Transcription interference is widely used to describe the gene regulating mechanisms caused by traffic problems like accumulations and collisions. The result of interference is that one transcription process directly suppresses, or even enhances, another transcription process [134]. This does not include the following special cases: repressor bindings, promoter modifications, obstacles on the DNA different from RNAPs, small RNA regulation, etc. Transcription interference describes the RNAP-RNAP interaction on the DNA or the interference of transcription traffic along DNA. As a result, the definition of interference applies to the three cases presented in figure 5.2 [134].

Collisions occur when two polymerases can transcribe on opposite strands at the same time. This results from the presence of two convergent promoters on a DNA template. Such genetic structures are found in a variety of organisms, e.g., *E. coli* and even humans [135, 136]. Collisions refers to RNAP-RNAP collision where an RNAP travels along the DNA and bumps into another RNAP [135, 136, 137, 138, 139]. However, RNAPs have been reported to collide with other traffickers, e.g., the replication apparatus [140]. There

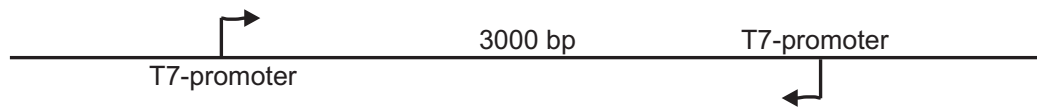


Figure 5.3: Sketch of the DNA strand with two opposing T7 promoters that is modeled with the parameters given in table 5.1.

could be different mechanical causes of the interference collisions: RNAPs collide and one or both disengage from the DNA template, or RNAPs stall when they meet other RNAPs on the opposite strand. This could be a direct physical result of the machinery or an effect of the super-coiling in front of the polymerases, that could be referred to as hyper-super-coiling. Any of these mechanisms would explain a drop in transcription. So far the destiny of collided RNAPs is unknown. However, there are several possible outcomes of a collision:

- Both RNAPs dissociate from the DNA template resulting in complete loss of expression for both genes.
- One RNAP dissociates, i.e., is knocked off, resulting in the loss of expression of one gene. The other stays.
- Both RNAPs stall and remain bound to the DNA.
- One RNAP pushes the other back towards the promoter.
- The RNAPs pass each other by some unknown mechanism.

None of these outcomes need to be exclusive. Moreover, the outcomes could be one when an RNAP is bound to a promoter and another when both are transcribing.

Sneppen et al. approach the problem of finding the magnitude of interferences analytically [141]. They find the effect of interference on the expression of a specific gene from the equilibrium rate functions. This model explains the experimental data reported [141] for a convergent system as sketched in figure 5.2b. However, this can not be generalized to all systems. In particular, it does not apply to the systems with distances between the promoters of more than a few hundred bp or promoters of equal strength. That is promoter sites with an equal rate of sending off RNAPs. Hence, inspired by the Java applet presented on the Cmol homepage <http://cmol.nbi.dk/models/dna/rnap.html> a stochastic simulation of RNAP traffic is presented in this section.

The RNAP spends more time on the promoter site than on any other sites on the DNA. Therefore, interference is likely to occur at the promoter. An

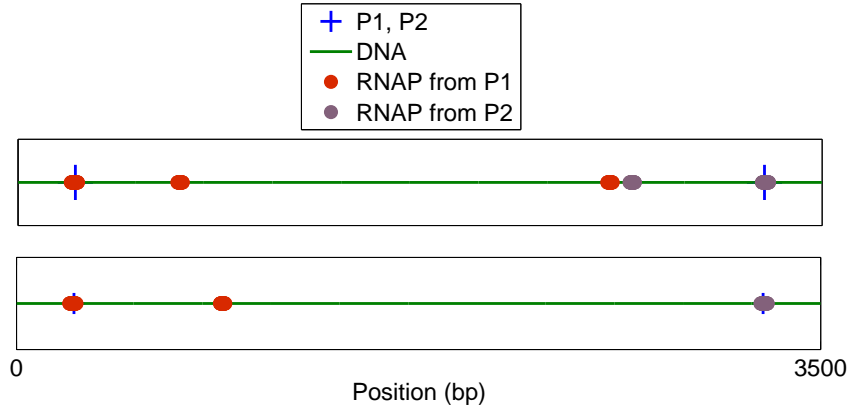


Figure 5.4: Snapshots from a stochastic simulation. In the upper panel two ECs are about to collide and in the following frame (lower panel) they are both removed from the template and the space is free for subsequent ECs to take over.

RNAP that attaches to a promoter is termed a sitting duck complex (SDC). With some probability, this transforms to an elongating complex (EC) and starts transcription. The rate of this transformation reflects the promoter strength [141]. All in all, this is a two step process though it actually is at least a three step process: bound closed complex, open complex, and initiation of elongation. However, here it is reduced to:



The system simulated here is shown in figure 5.3. RNAPs attach and travel along DNA from oppositely directed promoters. From this simulation we extract the stochastic rate of SDC-EC collisions and EC-EC collisions.

5.2.1 Methods

The distance between the promoters is L_{PP} and it is assumed that an EC-EC collision results in the disengagement of both ECs and that an EC-SDC collision results in the disengagement of the SDC but does not affect the EC [141]. For each time step dt , the probability of formation of an SDC or an EC is evaluated by a dynamic Monte Carlo algorithm. $[t, t + dt]$ time steps are evaluated and dt is $1 \text{ bp}/v$, where v is the velocity of an EC. In dt an SDC is formed at a promoter site with probability k_{on} if not occupied or occluded. An SDC initiates elongation with probability k_f . At last, any EC is moved $v \cdot dt$ steps. See figure 5.4 for a snapshot of a simulation.

Parameter	Value	Reference
[RNAP]	10 nM	
L_{PP}	3000 bp	
SDC	32 bp	[141]
EC	24 bp	[141]
k_{on}	0.29 s^{-1}	[8]
k_f	0.36 s^{-1}	[8]
v	40 bp/s (<i>in vivo</i>)	[142]

Table 5.1: The parameters and their values used for the stochastic simulation.

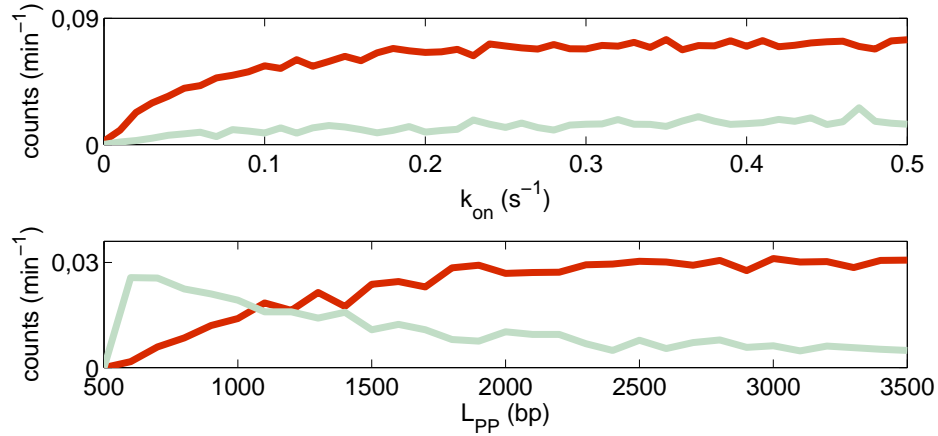


Figure 5.5: Rate of collisions versus binding rate and inter-promoter distance, respectively. Curves are the mean of 10 runs of simulation for EC-EC collisions (red curves) and EC-SDC collisions (gray curves). a) collision rates for different values of k_{on} . b) collision rates for different values of L_{PP} .

5.2.2 Results

The promoters are of equal strength as sketched in figure 5.3 with the parameters presented in table 5.1. The result is that the expected waiting time between two EC-EC collisions is ~ 10 min. This waiting time can easily be tuned by changing the parameters, e.g., the concentration of RNAPs. In figure 5.5 the rate of collisions is shown for different values of the parameters k_{on} , which depend on the concentration of RNAPs, and the distance L_{PP} .

5.2.3 Discussion

This simulation provides a tool for investigations of the rates of occurrences for specific system. Here we found the collisions as a function of different variables, e.g., the promoter strength or RNAP concentration. However, this simulation needs to be compared to experimental results to justify the assumptions made. In particular, it is interesting to know more about the outcome of the collision and the fate of the ECs. These results are, therefore, only indicative when measuring the rates of collisions on a template of thousands of bp.

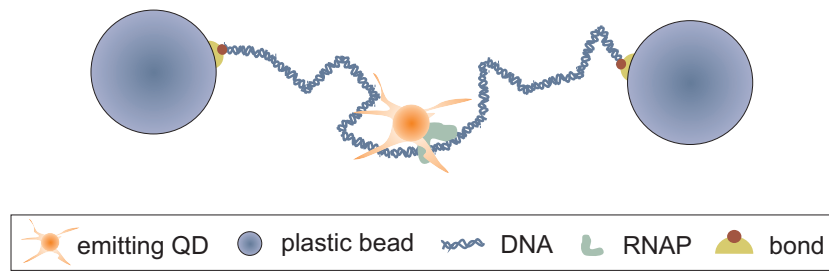


Figure 5.6: Sketch of an assay where the DNA is partially extended between two particles. The attachment of the DNA to the beads are mediated by chemical bonds (**bond**) like anti-digoxigenin:digoxigenin or biotin:streptavidin. Not to scale.

5.3 Conformations of DNA extended between two beads

Despite the high luminescence of QDs, care must be taken to choose a template where the thermal noise is low enough to track individual RNAPs attached with QDs, as discussed in section 5.1. Therefore we set out to investigate the thermal motion of DNA in the geometry depicted in figures 5.1a and 5.1b. Here two polystyrene beads holds the DNA as depicted in figure 5.6. The advantage of this geometry is that the thermal fluctuations of the DNA is minimized. This is important because it is a challenge to track a single QD with the EMCCD within a large volume. However, tension on the DNA might affect the work of the enzyme in question. Therefore, these two aspects should be balanced in the optimal manner. To this end, the force-extension relation of the DNA strand is measured. This is used to calculate the volume that confines the DNA; i.e., the volume within which one can expect to find the QDs.

5.3.1 Methods

DNA template

The DNA template was synthesized in the laboratory of Szabolcs Semsey at ELTE, Budapest. Later Mette Eriksen re-synthesized this DNA template in the laboratory of Michael Sørensen at BioCenter. Szabolcs Semsey is the designer of this DNA template.

3 77-mer: 5' TTT TGA ATT CAA AAA ACC CCT CAA GAC CCG TTT
AGA GGC CCC AAG GGG TTC TCA TGC TGA AAA CGT GGT GTA

CCG GC 3'

4 41-mer: 5' TTT TTT AAG CTT GGA CCT ATC TGC CCG TTC GTC
CCG TCG TT 3'

These 2 primers were used to synthesize the DNA template. It was inserted between the HindIII and EcoRI sites of plasmid pGEM47 (Promega) as sketched in appendix C.1. The construct (pLJP1) was sequenced with these primers:

1 26-mer: 5' Bio-TGT GAT GCT CGT CAG GGG GGC GGA GC 3'

2 25-mer: 5' Dig-CAA ATA GGG GTT CCG CGC ACA TTT C 3'

The resulting DNA template is a $\sim 4,000$ bp piece of λ DNA with one promoter and one terminator and 3,000 bp between them. A sketch of this DNA template is shown in appendix 5.7. This is used for the experiments reported in this section and in section 5.5.



Figure 5.7: A sketch of the DNA template used for these experiments. **Bio-tag** denotes the biotin-labeled end and **Dig-tag** denotes the digoxigenin labeled end.

DNA stretching experiments

For the DNA stretching experiment streptavidin-coated beads (Bangs Laboratories) with a diameter of $3.1 \mu\text{m}$ are washed, as described in appendix D.2, and incubated with the DNA template. The DNA attached beads are mixed with anti-digoxigenin-coated polystyrene beads with a diameter of $1 \mu\text{m}$ (Spherotech) in a TE-buffer and transferred to a microfluidic chamber as described in detail in [3, 143] and appendix D.2. The tethers are created as shown in figure 5.8. Custom-made Labview and Matlab procedures are used for precise force-measurements exactly as described in [3, 144].

5.3.2 Results

As mentioned, we want to balance the benefit of reducing the thermal noise with the cost of tension in the DNA template. As demonstrated in figure 5.9 the cost of stretching the DNA to lengths of less than 90% of contour length L is less than 10 pN. In this regime the force is mostly entropic and the DNA tether can be considered as an entropic spring. Thus, with an end to end distance r_{ee} of less than 90% of L we do not change the tension in the DNA considerably.

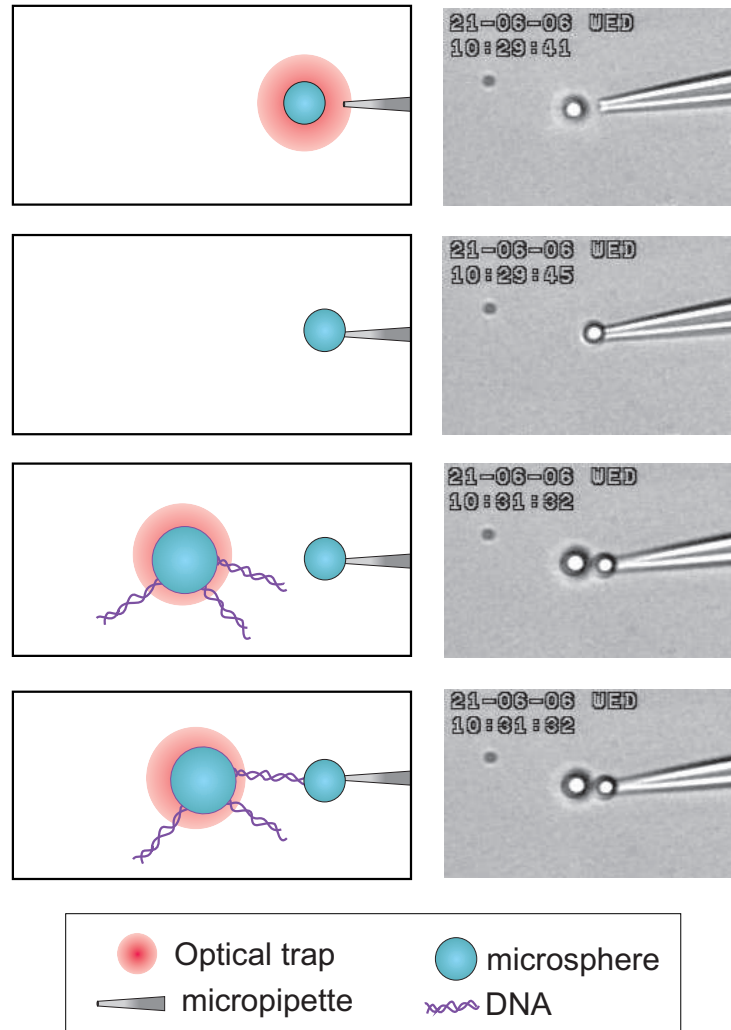


Figure 5.8: Sketch of the tether pulling assay [143]. The frames are progressing in time from top to bottom. In the first frame a small anti-digoxigenin-coated bead is optically trapped and placed on the tip of a micro-pipette (second frame). Then a larger streptavidin-coated bead with attached double stranded DNA strands is trapped (third frame) and a DNA tether is created between the two beads (fourth frame). For more information of the experimental methods see appendix D.2.

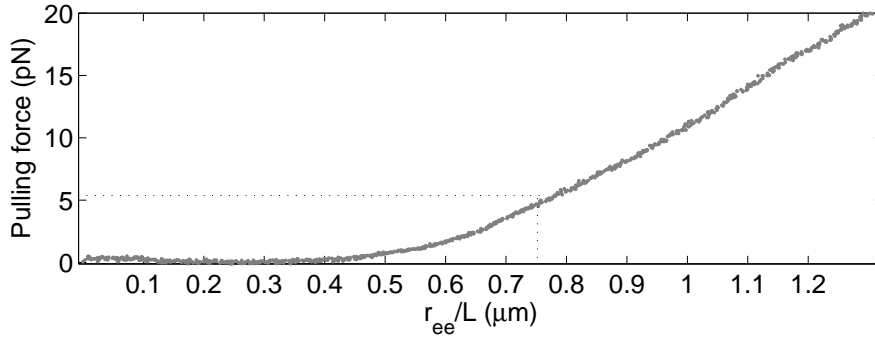


Figure 5.9: Force versus extension of DNA. Note that the first part of this curve reflects the low energy cost of stretching the DNA to somewhat less than the contour length $L \sim 1.36 \mu\text{m}$. The dotted line shows that the force needed to extract the DNA to 75% of L is 5 pN.

5.3.3 Discussion

This knowledge is used to find the spatial configurations of the freely joined polymer by a 3D trajectory in space. This is a theoretical treatment of a real chain divided into N Kuhn segments of l_k , so that each Kuhn segment can be thought of as if they are freely joined with each other to give the contour length $L = N \cdot l_k$ [145].

A double stranded DNA template of 4,000 bp consists of about $13 \times l_k$. If the DNA is extracted to 75% of the contour length, $r_{ee} = 10 \times l_k$, then the surplus DNA is $3 \times l_k$. Hence, this is the upper limit of the radius of the confined volume $R_c \sim 300 \text{ nm}$.

Another way to estimate an upper limit of R_c is to consider the polymer as a parabola. The arc length L is then:

$$L = \frac{1}{2} \sqrt{r_{ee}^2 + 16R_c^2} + \frac{r_{ee}^2}{8R_c} \ln\left(\frac{4R_c + \sqrt{r_{ee}^2 + 16R_c^2}}{r_{ee}}\right). \quad (5.2)$$

In figure 5.10 R_c is given as a function of r_{ee} . From this we have that when $r_{ee} = 75\% \times L$, then $R_c \sim 330 \text{ nm}$.

In summary, if the DNA is stretched to 75% of L then the QDs should be confined to a volume with a radius of less than 500 nm. Hence, the QD moves less than 500 nm away from the focus. This corresponds to exerting a force of 5 pN to the DNA as reported in [8]. The elongation velocity has been measured for different force loads (both assisting and resisting) and it is found to be, for T7 RNAP, nearly constant over the range from -15 to 15 pN [20]. Hence, 5 pN is within the range of tolerable force loads and this,

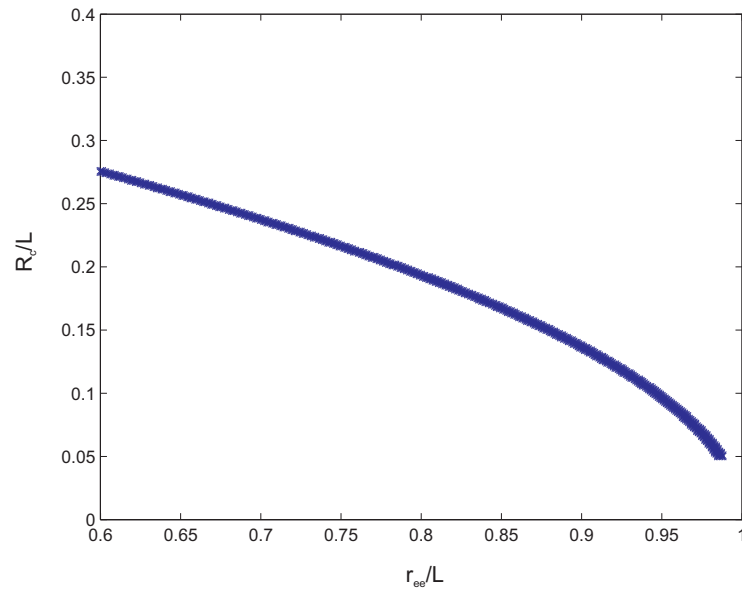


Figure 5.10: R_c , as a function of r_{ee} ; both normalized with regard to the contour length L . The relation is given in equation (5.2).

probably, does not affect the transcription of the RNAP. Hence, it should be possible to track QD attached RNAPs without changing their transcription rate.

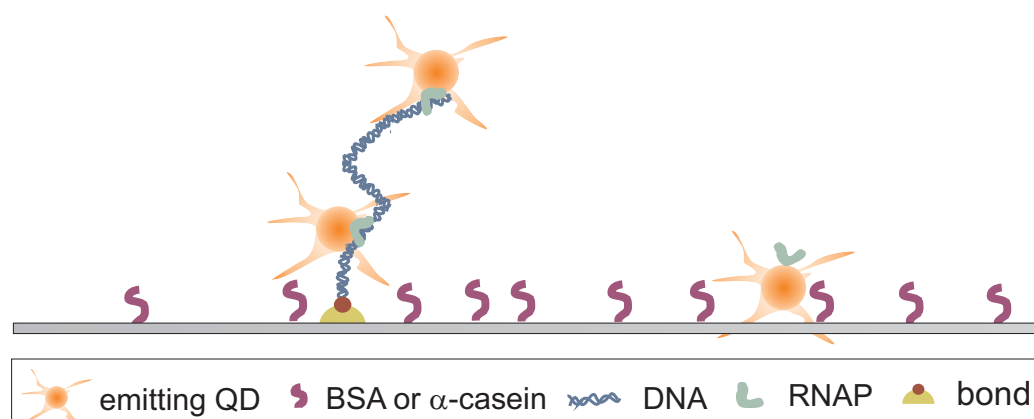


Figure 5.11: Sketch of the activity test. A DNA of length ~ 220 nm with one T7 promoter and no terminator is anchored to a surface. The attachment of the DNA is mediated by the chemical bond (**bond**) anti-digoxigenin:digoxigenin. QD:RNAP complexes is expected to build up on the DNA.

5.4 Construction of quantum dot labeled polymerases

T7 is a phage that attacks nearly all *E. coli* strains. It consists of a $\sim 40,000$ bp DNA and a capsid to protect it. The RNAP of this phage has a very low error rate and a molecular weight of 99 kDa. T7 RNAP is extremely promoter-specific and only transcribes genes downstream of a T7 promoter; as described in section 1.2. Therefore, this single-unit RNAP is often used for *in vitro* experiments. For details on the T7 RNAP molecular structure and conformation see References [16, 146, 147, 148, 149, 150, 151, 152, 153].

The RNAP is stimulated by BSA or spermidine and needs Mg^{2+} as a co-factor. The T7 family of RNAPs is structurally and evolutionarily distinct from the multi-subunit family of RNAPs, e.g., from *E. coli* and eukaryots. Nevertheless, many common functional features are shared with these more complex enzymes. Hence, the T7 RNAP is a model system for investigation of DNA traffic.

To attach a QD, an RNAP is constructed with a bio-tag at the N-end just next to the His-tag (T7-Bio-His6). T7 RNAP is expressed in *E. coli* together with a plasmid carrying a bio-tag (BirA). This specific biotinylation minimizes the interference between the bio-tag and the active site of the enzyme.

This bio-tag should be used to attach streptavidin-coated QDs. Marit Sletmoen tried an alternative biotinylation method, relying on unspecific binding of biotin; as described in appendix C.3. However, in this section we will only consider the specific biotinylation of RNAP.

The activity of this QD:RNAP is investigated through a TPM assay with DNA strands (~ 200 nm) as depicted in figure 5.11. This template has a promoter (pointing towards the cover slide surface) and no terminator. Hence, the RNAPs can not escape the DNA once it has attached. The accumulation of RNAPs on the template is investigated by measuring the emitted intensity of bright QD spots over time.

5.4.1 Methods

The construction of the T7-bio-His6 were carried out in the laboratory of Szabolcs Semsey at ELTE, Budapest. This system resembles the ones described in References [142, 154]. Mette Eriksen re-expressed biotinylated T7 RNAPs in the laboratory of Michael Sørensen at BioCenter [155].

Cloning

Biothis1 49-mer: 5' ATC ACC ATG GGT AGC AGC GGC CTG AAC GAC ATC TTC GAA GCT CAG AAA A 3'

Biothis2 59-mer: 5' ATC TTC GAA GCT CAG AAA ATT GAA TGG CAC GGC AGC TCT CAT CAT CAT CAT CAT CAT AG 3'

Biothis3 63-mer: 5' A TAG CTC GAG CAT ATG AGA ACC GCG CGG CAC CAG ACC ACT GCT ATG ATG ATG ATG ATG ATG AG 3'

These 3 primers were used to synthesize the biotinylation tag. It was inserted between the XhoI and NcoI sites of plasmid pBH161.

The construct (pT7Bio) was sequenced with this primer:

RNAP100 75 25-mer: 5' A GCT AAA CGC TCA CCG TAA TGG TCA 3'

Purification of T7-bio-His6:

Strain: *E. coli* BL21(DE3) Star (invitrogen) +pBirA (Avidity) +pT7Bio. Synthesized in the Semsey laboratory [156].

This strain is grown overnight in LB media with ampicillin and chloramphenicol (37° C). 4 ml of this culture is transferred in 400 ml Terrific Broth+ampicillin supplemented with 8 ml 20% glucose (37° C). At a cell density of OD600= 0.7, 6 ml of 100 mM IPTG and 50 μ M D-biotin is added. This is incubated for 3 h at 30° C.

This solution is centrifuged in 2 tubes (200ml each) and the cells are resuspended in 8 ml 20 mM Tris-HCl, pH 7.9. Then 500 μ l 20 mg/ml Lysozyme

is added and the solution is incubated on ice for 30 min. 8 ml Lysis Buffer (20 mM Tris-HCl, pH 7.9, 1 M NaCl, 0.1% Tween 20, 5 mM Imidazole) is added and again it is incubated on ice for 30 min.

This is centrifuged for 45 min at 15000 rpm and 1 ml Ni-NTA is added to each tube. Afterwards, it is incubated on ice for 1 h. Then the column is loaded and washed with 20 mM Tris-HCl, pH 7.9, 0.5 M NaCl, 0.05% (v/v) Tween 20, 20 mM Imidazole.

At last this is eluted with 20 mM Tris-HCl, pH 7.9, 0.5 M NaCl, 0.05% (v/v) Tween 20, 200 mM Imidazole. This procedure is described in detail in appendix C.2 and in particular in Reference [155].

Affinity of T7-bio-His6 to streptavidin

The affinity to biotin where tested with a SofLink for streptavidin (Promega). T7 RNAP is mixed with the SoftLink and incubated for 30 min. Then this solution is loaded to a physical matrix, or column, and the *flow-through* and the *matrix-bound* proteins are separated. Then the column is washed with 20 mM Tris-HCl, pH 7.9, 0.5 M NaCl, 0.05% (v/v) Tween 20, 200 mM Imidazole.

Activity of QD marked T7-bio-His6

For these experiments Mette Eriksen synthesized a DNA template of 651 bp: The construct plasmid pGEM4Z (Promega) was sequenced with these primers:

1 33-mer: 5' GGA ATT GTG AGC GGA TAA CAA TTT CAC ACA 3'

2 25-mer: 5' Dig-CAA ATA GGG GTT CCG CGC ACA TTT C 3'

This template is sketched in figure 5.12 and further details are given in appendix C.1.

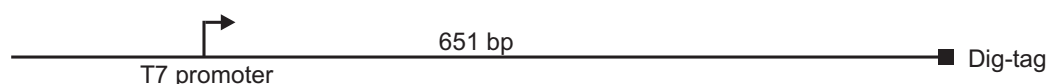


Figure 5.12: A sketch of the DNA template. **Dig-tag** denotes the digoxigenin labeled end.

Flow chambers are incubated overnight with anti-digoxigenin solution (20 $\mu\text{g/ml}$). Then rinsed with TE (10 mM Tris-HCl and 1 mM EDTA) buffer with 2 mg/ml α -casein (Sigma) and incubated with 0.1 nM DNA in TE buffer. Then the chamber is flushed with a reaction buffer (40 mM Tris-HCl, 6 mM MgCl_2 and 10 mM DTT) with 2 mg/ml α -casein. 100 $\mu\text{g/ml}$ BSA and 500 μM nucleotides is added to the reaction buffer before proteins and streptavidin-coated QDs ($\lambda = 605 \text{ nm}$) are diluted to a final concentration of $\sim 500 \text{ nM}$ and 10^{-4} , respectively. This solution is flushed into the chamber and

5.4.2 Results

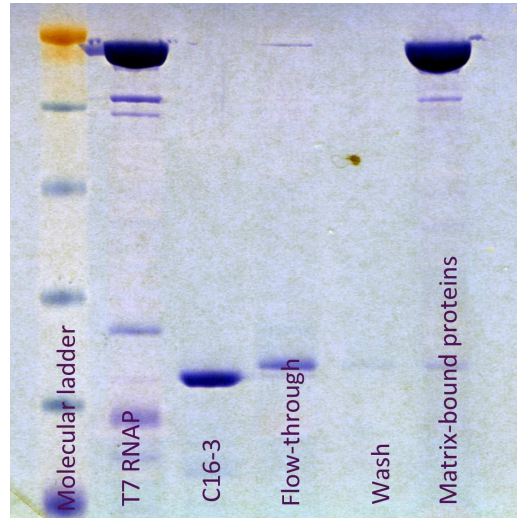


Figure 5.13: Results of the gel-electrophoresis where the affinity of T7-bio-His6 RNAP (T7 RNAP) to streptavidin is tested. The protein C16-3 is used as control and the *flow-through* signifies that this protein does not bind to the matrix. In contrast, the T7 RNAP binds to the matrix and the wash does not contain any of the two proteins; as expected. This work is done by Szabolcs Semsey.

investigated under the microscope. The sample preparation is described in more detail in appendix D.3. A surface of DNA tethers and QD:RNAP were investigated in the dark and individual spots were randomly chosen. The intensity of these spots were monitored over time through series of intensity images collected with the EMCCD. The images were analyzed as described in section 4.5.1.

The affinity of the biotinylated RNAP to streptavidin is tested and the results are shown in figure 5.13. Here it is seen that the band from the matrix-bound proteins is identical to the band from the T7 RNAP (second lane from the left). The control protein C16-3 did not bind to the matrix and the final wash did not contain any proteins. From these results we can conclude that the T7-bio-His6 RNAP has a high affinity to streptavidin. Therefore, it should easily bind to streptavidin-coated QD.

The activity of the T7-bio-His6 RNAP is tested by gel-electrophoresis as shown in figure 5.14. Since the second lane from the left in figure 5.14 has a band of the length of the template in the first lane, it is concluded that the T7 RNAP is active. These results have been reproduced by Mette Eriksen in

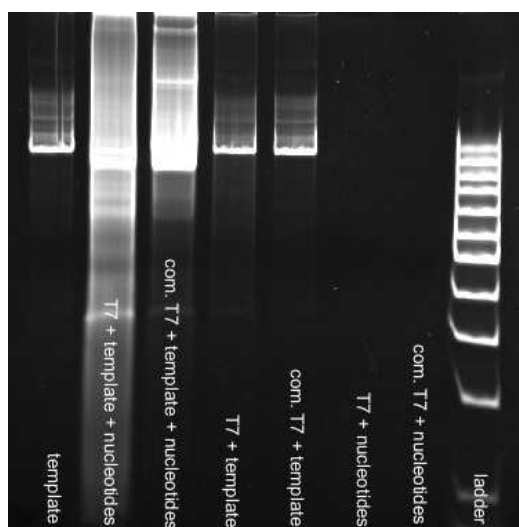


Figure 5.14: Results of the gel-electrophoresis where T7-bio-His6 RNAP (T7) is compared to a commercially available T7 RNAP (com. T7). A clear band from the added DNA (template) is seen and the ladder gives the molecular weight of the divers bands.

the laboratory of Michael Sørensen at BioCenter. The specific biotinylation is advantageous, since it ensures a larger control of the molecular structure.

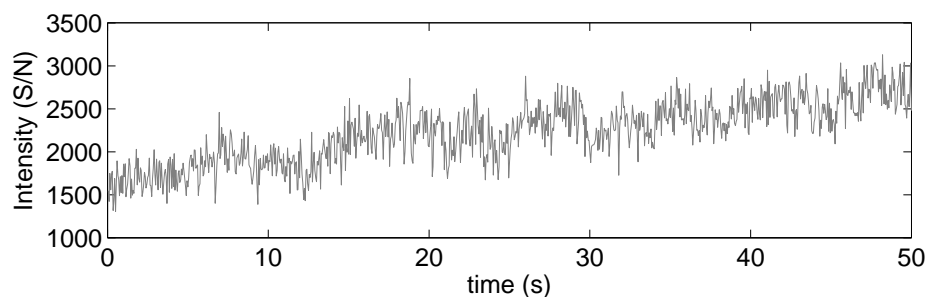


Figure 5.15: Emitted intensity (S/N) versus time for spots on the surface. The curve is the average intensity of 18 randomly chosen spots.

In figure 5.15 the average intensity over time is presented for 18 individual spots on the surface. From this it is concluded that over a time span of 50 s the average intensity of the spots increases by a factor 1.6.

With an RNAP concentration of 500 nM, the on rate k_{on} is limited by the firing rate k_f and an RNAP attaches to the DNA every third second;

as given by table 5.1. Furthermore, the T7 RNAP can transcribe 650 bp DNA in 10-20 s and the elongating complex has a dissociation time of tens of minutes [142]. Given this, the DNA templates should all be fully occupied by RNAP:QD complexes after 100 s. However, there is no way to estimate the average occupancy on a DNA strand since there is no way to discriminate DNA attached QDs from QDs unspecifically attached to the surface.

5.4.3 Discussion

We successfully synthesized a T7 RNAP with a specific bio-tag for QD attachment. We tested the affinity of this bio-tag and the activity of the modified RNAP. Furthermore, we set up a preliminary assay to test whether the binding of RNAP to a QD changes the conformation of the RNAP to an extent where it is no longer active. Unfortunately, the results of this assay were not conclusive. This rather short DNA (~ 200 nm) template is utilized to suppress thermal fluctuations. However, it is exactly thermal fluctuations that allowed us to distinguish DNA attached QDs from QDs unspecifically attached to the surface in the work that will be presented in section 5.5. These experiments should be repeated, possibly with longer or fluorescently labeled DNA. This is to discriminate between DNA bound QDs and unspecifically bound QDs. Furthermore, these experiments could be supported by bulk assays where RNAPs that are both bound to QDs and active are collected in a way similar to what is presented in Reference [142] and in the supplementary material of Reference [133].

It has been shown that fluorescent RNAPs can be followed individually during transcription [131]. Recently a QD:RNAP complex was presented as a measure of the position of RNAPs on the DNA [154]. Since the RNAPs were labeled with QDs after binding of the RNAP to the DNA, no activity or even ability to find the T7 promoter were proven in this assay. To my knowledge, there are no reports on activity of a QD:RNAP complex. Therefore, it would be interesting to repeat these experiments.

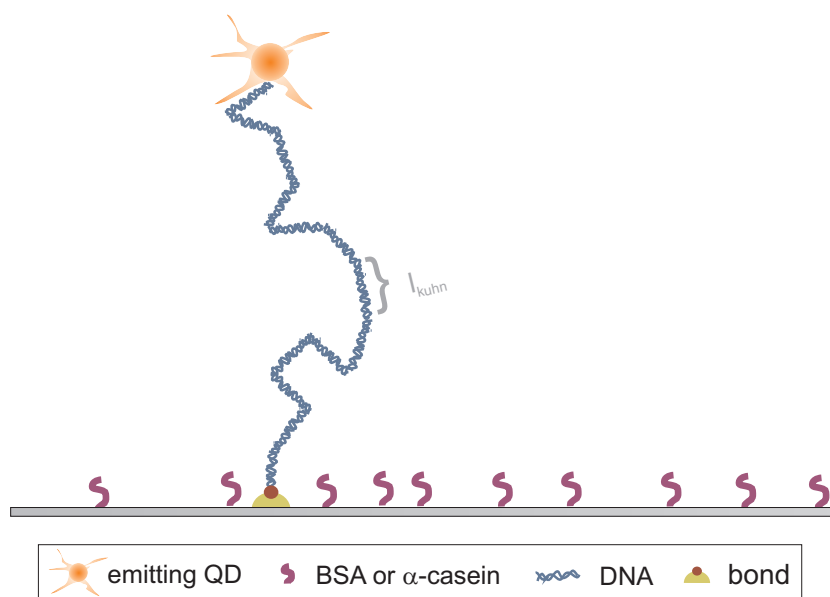


Figure 5.16: Sketch of a TPM assay with a QD as the reporter particle. The attachment of the DNA is mediated by the chemical bond (**bond**) anti-digoxigenin:digoxigenin. Not to scale.

5.5 Tethered particle method with quantum dots

We did many tries to see the RNAP:QD complex in the assay, described in section 5.3, where the DNA forms a RNAP highway between two beads. These tries were unsuccessful, partially, because the RNAPs were polluted with a DNA degrading enzyme. We realized this much too late. This is why we tried to take one step back and consider the geometry shown in figure 5.1d, where a bead is anchored to a surface. However, in this case we used a QD as tracker particle and to my knowledge it is the smallest tracker particle ever used to investigate tethered particle motions. Figure 5.16 sketches the tethered particle method (TPM) where a double stranded DNA is anchored to a surface and the other end of the molecule is bound to an otherwise free reporter particle. In this case, the reporter is a QD. The exploited Brownian motion of a DNA-tethered QD probes the conformational changes of the tether as done earlier by References [157, 158, 159, 160] and many more. TPM magnitude needs to be calibrated as a function of the particular DNA length and particle size. These are important initial experiments to understand and extract possible movements of a binding protein etc. So far no TPM using QDs are reported so this system still needs to be calibrated. In particular, the thermal motion of a QD anchored to a surface with a double

stranded DNA of length $1.36 \mu\text{m}$ is considered.

5.5.1 Methods

Sample chambers are prepared with an anti-digoxygenin-coating to bind to the digoxigenin end of the DNA described in 5.3.1. After incubation with 0.1 nM DNA in TE (10 mM Tris-HCl and 1 mM EDTA) buffer the samples are incubated with streptavidin-coated QDs in TE buffer that binds to the biotin-end of the DNA. Then this solution is interchanged with TE buffer with 2 mg/ml α -casein and the samples are sealed with vacuum grease. More details about the sample preparation are given in appendix D.4.

The samples are investigated under the microscope and intensity images are collected with the EMCCD with a rate of $10/\text{s}$. These image sequences are analyzed with the particle tracker routine Spottracker2D [161], available as plug-in for the open source ImageJ. The coordinates of the QD is extracted through a tiff-stack. Afterwards, these coordinates are analyzed and exposed to the following selection criteria by Rob Phillips and co-workers [160]:

The first criteria regards the symmetric in-plane motion about the anchor point. The second moments of the positions give us the co-variance matrix:

$$c_{x,y} = N^{-1} \sum_1^N x_k y_k - \bar{x} \bar{y}, \quad (5.3)$$

where x and y are the positions in the two directions in the projected plane, \bar{x} and \bar{y} are average displacements around the anchor point, and N is the total number of frames. The eigenvalues of this matrix (λ_1, λ_2) are equal for a perfectly symmetric motion. For the symmetry criterion to be fulfilled $\sqrt{\lambda_{max}/\lambda_{min}} \leq 1.1$ [160].

The root-mean-square displacement (RMS) is a function of the total sampling time or time lag τ :

$$\text{RMS}_\tau = \sqrt{\langle (x - \bar{x})^2 + (y - \bar{y})^2 \rangle_\tau}. \quad (5.4)$$

A constant RMS is an excursion characteristic of a Brownian motion around an anchor point as is the case of the tethered QD. The second criteria sets a lower limit on the RMS displacement to remove excursions of multi-tethered QDs or unspecifically bound QDs. Therefore, $\text{RMS} \in \{100 \text{ nm} : L\}$ is considered ($L \sim 1.36 \mu\text{m}$).

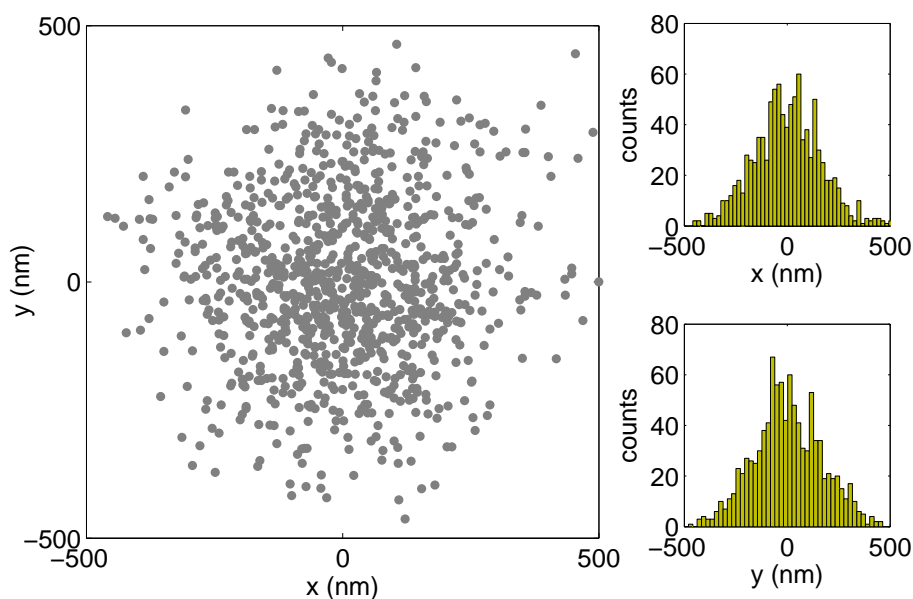


Figure 5.17: Analysis of intensity images of a QD tethered to the surface. The sampling rate is 10/s and the 2D projected position on each frame is plotted to the left. The distributions of positions in the two directions are shown to the right.

5.5.2 Results

The TPM data was evaluated using the criteria mentioned above and analyzed as shown in figure 5.17. This is an example of a data set; to the left is the centroid positions and to the right the position distributions.

The average RMS were found for 18 different excursions as shown in figure 5.18. From this figure it is seen that $\langle \text{RMS}_\tau \rangle$ reaches a plateau of 238 nm for $\tau > 150$ s.

5.5.3 Discussion

The $\langle \text{RMS}_\tau \rangle$ is considerably smaller than reported for polystyrene beads; when the length of DNA is taken into account. For comparison the results of Rob Phillips and co-workers are shown in table 5.2. From this it is seen that $\langle \text{RMS}_\tau \rangle$ lowers for smaller particles. Hence, QDs are exploiting the regime of very small reporter particles. Furthermore, the blinking of QDs does not seem to have any effect of the understanding of the behavior on the scales of seconds.

The proximity of the tethered particle to the anchoring surface affects

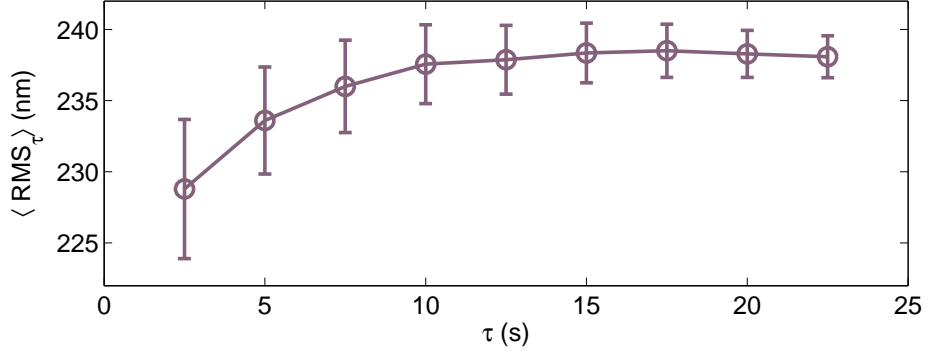


Figure 5.18: The average RMS_τ for TPM with QD reporters ($L = 1.36 \mu\text{m}$) versus τ . Error bars are SEM. It reaches a constant level for $\tau > 15$ s; $\langle \text{RMS}_\tau \rangle = 238$ nm. The SEM is less than 10% in good accordance with the results from Reference [160].

	$R = 8$ nm	$R = 100$ nm	$R = 245$ nm	$R = 485$ nm
$L \sim 850$ nm	ND	280 nm	320 nm	480 nm
$L \sim 1,360$ nm	238 nm	ND	ND	ND

Table 5.2: In this table the $\langle \text{RMS}_\tau \rangle$ is stated for different sizes of tracker particles and different lengths of DNA. Data from this section and from Reference [160]. ND is not determined.

not only the interpretation of the tethered particle's motion but also the conformation of the macro-molecules at interest. The excursion of the tracker particle dominates the DNA when

$$R < \sqrt{2/3 N \cdot l_k^2}, \quad (5.5)$$

where R is the radius of the tracker particle [157]. For the QDs used here R is approximately 8 nm, see section 4.4. Furthermore, the right term is recognized as the RMS in the 2D projection given in equation (5.10). As $8 \text{ nm} \ll 295 \text{ nm}$, this is in the limit where movements of the tracker particle is dominated by the DNA and not the other way around.

The DNA polymer can be approximated with a floppy chain where the possible end to end distance, r_{ee} , can be anything between 0 and L . Here we will not consider self-occlusion. When the DNA tether of contour length $L > 13 \times l_k$, one could assume that it falls within the limit where $l_k \ll L$. This corresponds to the situation where the tethered QD is like a free moving QD restricted to the half sphere of radius L . The probability distribution of

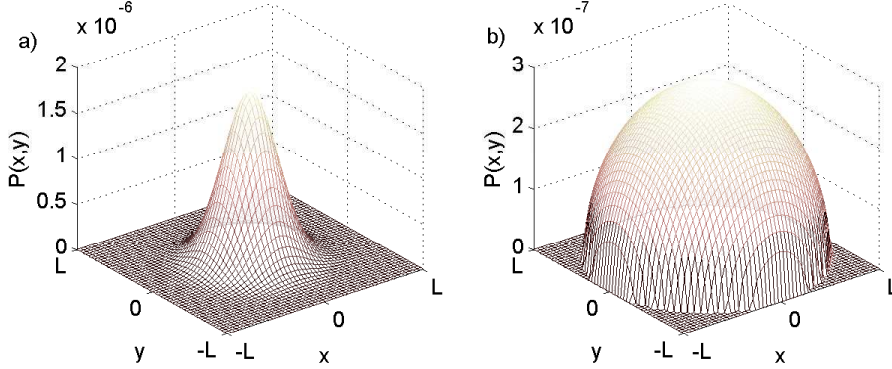


Figure 5.19: Two possible probability distributions of the projected position of the QD on the xy -plane. a) shows the Gaussian distribution which is the continuous limit of the binomial distribution. b) is the limit where the QD performs a random walk within the half sphere of radius L . Note that $\mathcal{P}(0,0)$ differs with a factor of 10 between the two distributions.

the QD position, or the r_{ee} , in a half sphere is:

$$\mathcal{P}(r_{ee}) = \frac{\int_{-r_{ee}}^{r_{ee}} \pi(r^2) dr}{\int_{-L}^L \pi(L^2 - r^2) dr}. \quad (5.6)$$

This probability distribution is shown in figure 5.19b. To determine the mean square displacement in 3D we solve the following integral:

$$\langle r_{ee}^2 \rangle = \frac{\int_{-L}^L \pi r^2 (L^2 - r^2) dr}{\int_{-L}^L \pi (L^2 - r^2) dr} = \frac{L^2}{5}. \quad (5.7)$$

The radial RMS = $\sqrt{\langle r_{ee}^2 \rangle}$, so for the projection in the x, y plane:

$$\text{RMS}_{x,y} = \sqrt{\frac{2}{3} \cdot \frac{L^2}{5}} = 475 \text{ nm}. \quad (5.8)$$

This is an overestimation of RMS and signifies that this limit does not cover our case. The QD is not moving as a free particle in the half sphere; as given in inequality 5.5.

Instead, the DNA should be regarded as a semi-flexible chain of l_k 's. Here the probability distribution is binomial as the configurations are random walks in space with step sizes of l_k [145]. In the continuous limit

$$\mathcal{P}(x, y) = \mathcal{P}(x)\mathcal{P}(y) = (2\pi\sigma^2)^{-1} \exp-(x^2 + y^2)/2\sigma^2, \quad (5.9)$$

where $\sigma^2 = (2/3)N \cdot l_k$. This probability distribution is shown in figure 5.19a. In the case where $N = 13$ we can regard this as continuous [145] and we get

$$\text{RMS}_{x,y} = \sqrt{\frac{2}{3}N \cdot l_k^2} = 294 \text{ nm.} \quad (5.10)$$

This is closer to the experimentally found value. However, more theoretical corrections, e.g., self-occlusion, must be considered to make the theoretically and experimentally found values for RMS to coincide.

In this section QDs as tracker particles for TPM assays were considered. To this end QDs were anchored to a surface with DNA ($L \sim 1.36 \mu\text{m}$) and the Brownian motion was observed. From this the $\langle \text{RMS}_\tau \rangle$ was found to be 238 nm which is considerably smaller than for other tracker particles. The results in this section, shows that QDs are excellent tracker particles as the movement of the QD itself does not dominate the excursions of the macro-molecule at interest.

5.6 Conclusion

The aim of the work presented in this chapter was to set up an assay to follow individual RNAPs on DNA. To this end biotinylated RNAPs were expressed *in vivo*. We showed that the RNAPs with bio-tag is active and have a large affinity to streptavidin. Therefore, they should bind to streptavidin-coated QDs. However, we did not measure the activity of QD-bound RNAPs conclusively. Thus, more work needs to be done before the model system of RNAP:QD is ready for use in investigations of RNAP traffic on DNA.

Different geometries, for assays following individual RNAPs on the DNA, were considered in this chapter. As it is well-known the geometry with a DNA strand held between two beads reduces thermal noise and gives high spatial resolution along the DNA template. This should, therefore, be the preferred geometry. However, we also considered the simpler TPM as this has the advantage that several DNA tethers can be observed at the same time. Thus, we calibrated a TPM assay for the smallest tracker particle reported for this kind of assays.

CHAPTER 6

Summary and outlook

This chapter provides a brief summary and discusses some additional research directions.

6.1 Summary

The work in this thesis was concerned with optical manipulation of small particles. This includes dielectric spheres in a standing wave evanescent field and quantum dots in the optical trap. The forces acting on the small particles in the optical fields are characterized and quantized. Ultimately to use them as force transducers on the pN scale. This is desirable for many biophysical applications.

A theoretical calculation of the forces exerted on a dielectric sphere in a standing wave evanescent field was carried out in chapter 3. The forces were decomposed into the gradient force and the scattering force and they were considered individually. The gradient force has a component in the direction of the evanescent field and one in the direction perpendicular to the wavefront. The scattering force only has a component in the direction along the wavefront. Considering the trapping efficiencies, we realized that the trapping would be strongest in the region of maximum intensity.

In recent years several optical trapping assays with nano-particles have been carried out in our laboratory. In the course of these, we trapped quantum dots as described in chapter 4. We found the trapping strength through investigations of the Brownian motion for many sizes of quantum dots. In addition, two-photon absorption in the trap was reported.

Furthermore, this thesis was concerned with questions about genetic reg-

ulation. First the *lac* operon in *E. coli* was considered in chapter 2. Lactose controls transport and metabolism pathways via two feedback loops connected by a common transcription factor. The auto-regulation of this transcription factor were measured experimentally and a mathematical model was made to explain the data. Furthermore, we argued that the auto-regulation ensures the cell a high sensitivity to lactose. We argue that in a fluctuating lactose environment the auto-regulated system performs better than the constitutive systems.

In chapter 5 another application of quantum dots were considered. The use of quantum dots for tracking individual polymerases on the DNA. We successfully constructed a specifically biotinylated RNA polymerase. It was shown that this tag had a high affinity to streptavidin appropriate for binding to quantum dots. In addition we carried out a calibration of a tethered particle method for a quantum dot and a piece of DNA of about 1 μm .

6.2 Outlook

Auto-regulation in the *lac* operon

The stochastic evaluation of the model presented in this thesis should be finished to have a consistent model of auto-regulation. Such a model could easily be changed to describe other systems of self-regulation.

Forces in the evanescent fields

As suggested in this thesis the theoretical results presented here should be compared to experimental results. These experiments could be done with a setup as the one described in chapter 3 and an ultra-fast camera. However, a lot of more sophisticated experimental results are already available from the laboratories of Pavel Zemanek and Kishan Dholakia.

Optical trapping of quantum dots

The first characterization of quantum dots as force transducers is done. Furthermore, the publications make our results available for other, potentially interested, laboratories. However, some additional information could be provided. For instance details about the Allan variance, as investigated by Fabian Czerwinsky and co-workers [162]. We want to use the Allan variance to investigate the time series of the quantum dot positions in the optical trap and include it in the proceeding of the SPIE meeting 2010. Some preliminary results reveals that the thermal drift is dominant for time lags above

100-200 ms. This should be taken into account when calibrating the forces on a quantum dot in the optical trap. Furthermore, we want to reconsider the differences in trapping strengths in the two lateral directions, i.e., the directions perpendicular to light propagation. We have indications that the more elongated quantum dots have trapping strengths that differ in the two lateral directions. This would mean that these elongated quantum dots align in the trap in a direction perpendicular to the direction of the propagating light.

RNA polymerase traffic on DNA

We want to measure the activity of quantum dot attached polymerases. It is desirable to know whether this attachment changes the configuration of the RNA polymerase to an extent where it is no longer active. Ideally this will be done with a combined single molecule experiment and a bulk experiment. The first could be a tethered DNA ($L > 500$ nm) with a promoter and no terminator for the T7 RNA polymerase. This would allow quantum dot attached polymerases to light up on the DNA. The second experiment would rely on a physical matrix; similar to the one described in section 5.4.1. With the right matrix and preparations we wish to collect RNA polymerases that are both active and quantum dot labeled. To my knowledge this has not been reported earlier. However, similar results have been shown, e.g., for a restriction enzyme specific to DNA [133].

APPENDIX A

Evanescent field of a single plane wave

Here the evanescent field created by a single plane wave is briefly considered and the forces estimated for a weak scatterer in the Born approximation is calculated. The parameter from table 3.1 are used for the calculations.

Intensity

For comparison, we consider the forces in the case of a single plane wave evanescent field. The intensity $I(\mathbf{b})$ is given as equation (3.1): as shown in figure A.1. The total intensity in cylindrical coordinates is solved analytically by Rohrbach [83].

$$\begin{aligned}
 I(a, \mathbf{b}) &= \int_0^a \int_0^{2\pi} \int_{-\sqrt{a^2-r^2}}^{\sqrt{a^2-r^2}} r \cdot \exp(-(z + b_z)/d) dr d\phi dz \quad (\text{A.1}) \\
 &= 4ad^2 e^{-\frac{b_z}{d}} \pi \left(a \cosh\left(\frac{a}{d}\right) - d \sinh\left(\frac{a}{d}\right) \right) a^{-1}
 \end{aligned}$$

Gradient force

Now the gradient force term from equation (3.17) is reconsidered specifically for this example. The gradient force is calculated in cylindrical coordinates.

$$\begin{aligned}
 \mathbf{F}_{grad}(a, \mathbf{b}) &= I_0 \frac{n_m \alpha}{2cV} \int_V \left\{ \frac{\partial I}{\partial r}, \frac{1}{r} \frac{\partial I}{\partial \phi}, \frac{\partial I}{\partial z} \right\} dV \quad (\text{A.2}) \\
 &= I_0 \frac{n_m \alpha}{2cV} \int_V \left\{ e^{-\frac{z}{d}}, 0, -\frac{e^{-\frac{z}{d}} r}{d} \right\} dV \\
 &= I_0 \frac{2dn_m \alpha}{cV} e^{-\frac{b}{d}} \pi \left\{ \int_0^a \sinh\left(\frac{\sqrt{a^2-r^2}}{d}\right) dr, \right. \\
 &\quad 0, \\
 &\quad \left. -a \cosh\left(\frac{a}{d}\right) + d \sinh\left(\frac{a}{d}\right) \right\}
 \end{aligned}$$

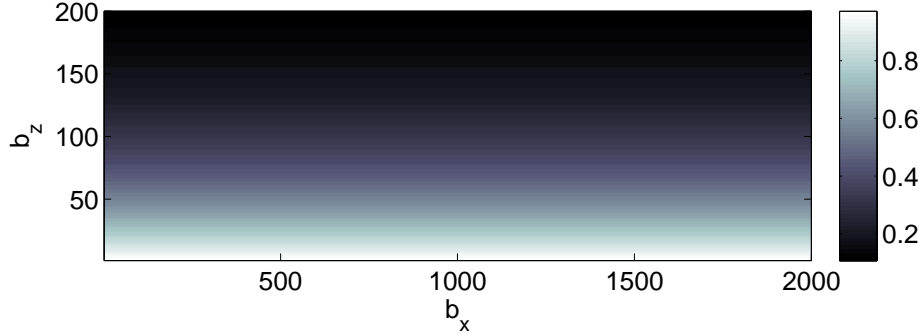


Figure A.1: A contour plot of the total scalar intensity $I(x, y, z)$ experienced by a sphere in the in position $\mathbf{b} = (b_x, b_y, b_z)$ in the x, z plane above the surface. The intensity is constant in the x -direction and y -direction. Parameters from table 3.1 is used for this plot and I is normalized with I_0 .

From this we see that \mathbf{F}_{grad} has a component in the radial r -direction which is dependent of the radius a and a component in the z -direction of the field. The force has no component in the azimuth ϕ -direction; which is obvious since the sphere is rotation symmetric.

Scattering force

The scattering intensity is the intensity of a Rayleigh particle [90] multiplied by the square of the form factor

$$I_{scat} = (1 + \cos^2 \theta) k^4 \cdot |\alpha|^2 \cdot \tilde{s}(\mathbf{g})^2 \quad (\text{A.3})$$

The effective cross sectional area of the particle in the TIRF evanescent field is given as

$$\begin{aligned} A'' &= \int_{-a}^a \int_{-\sqrt{a^2-x^2}}^{\sqrt{a^2-x^2}} \exp(-(z + b_z)/d), \, dz dx \\ &= \int_{-a}^a 2d e^{-\frac{b_z}{d}} \sinh\left(\frac{\sqrt{a^2-x^2}}{d}\right) dx \end{aligned} \quad (\text{A.4})$$

The scattering cross section C''_{sca} is found from

$$C''_{sca} = Q_{sca} \cdot A'' \quad (\text{A.5})$$

The scattering force is

$$\mathbf{F}_{scat} = I(x, y, z) \frac{n_m}{kC} C''_{sca} (1 - k \overline{\cos \theta_s}) \quad (\text{A.6})$$

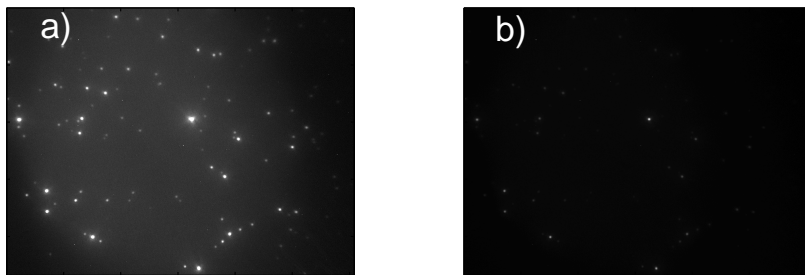


Figure A.2: Intensity images of fluorescent polystyrene beads ($a=30$ nm) illuminated in evanescent fields. a) SW-TIRF. b) TIRF. Note that the intensity is highest for SW-TIRF as predicted. Samples are prepared as described in section [3.4](#).

APPENDIX B

Setup

B.1 Simultaneous fluorescence microscopy and optical trapping

Some small electronic components and build-in lenses was removed from the back of the microscope to allow the laser and Hg light to enter the microscope in parallel, see figure [B.1](#) In short it has to consequences: The Hg light is more focused when it hits the sample and there is no internal shutter. Therefore, the shutter on the lamp should be utilized instead.

When aligning the laser one should be aware of the following: Firstly, here is now two mirrors in the microscope; both the mirror inserted in the lamp house and the mirror in the filter-cube or in the bright-field cube. This makes the alignment more difficult whilst the mirrors in the microscope are non-movable and not necessarily aligned to one another. However, following the directions of Steve M. Block [\[163\]](#) ensures a perfectly aligned trap that allows for both trapping and fluorescence microscopy; as shown in figure [B.2](#).

Secondly, the alignment should result in a trap centered in the field of view of the microscope both in x , y , and z -direction. Meaning that the trap needs to be in the field of view for all zooms, all cubes, and for fluorescence imaging. Furthermore, the telescope should ensure that the tracker particles and fluorophores are in focus.

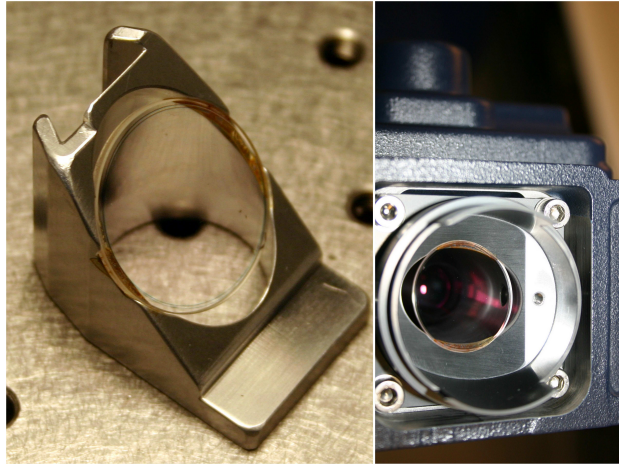


Figure B.1: To the left is our quasi-filter cube that is placed with next to the other filter cubes. This dichroic mirror reflects the laser and is necessary for trapping in bright-field mode. To the right is the modified lamp house where another dichroic mirror is inserted in the optical path of the Hg light. This reflects the laser light so that the laser light and the Hg light enters the microscope in parallel.

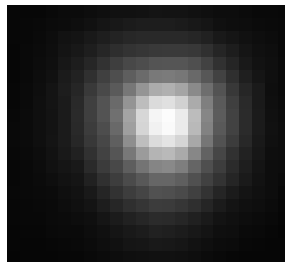


Figure B.2: An optically trapped fluorescent bead.

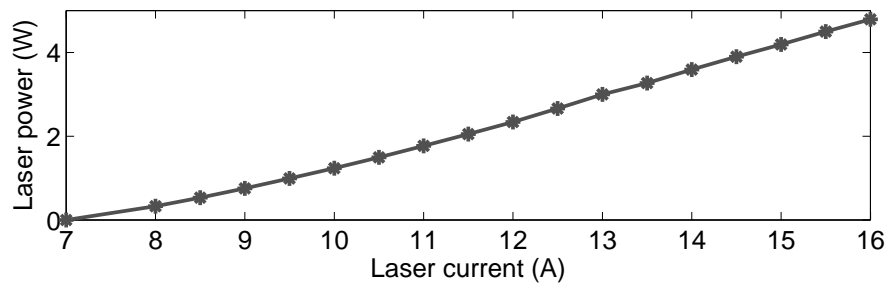


Figure B.3: The current set on the laser (laser.exe) relates to the laser power as shown here.

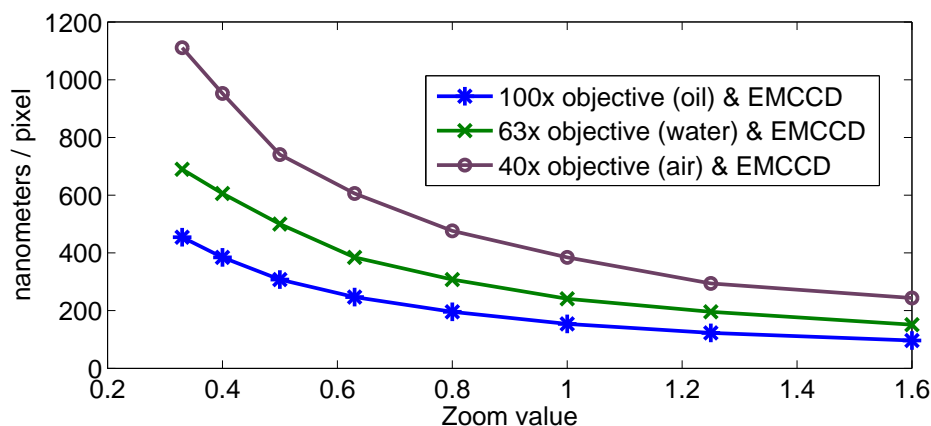


Figure B.4: Conversion factors for different zoom values and objectives.

B.2 Things to be aware of when using the EM-CCD

Here are some few instructions on how to use the new CCD camera with electron multiplier (EM). Good luck with the fabulous camera.

Turning the EMCCD on and off

To turn on the EMCCD: First, turn on the computer then start the Solis software and you will here a shutter open, if not click the shutter icon and open the internal shutter. Furthermore, look at the Andor instructions to the right of the computer screen.

To turn off the EMCCD: First, make sure that gain and cooling are turned off then close the Solis software. If the cooling was used wait at least 5 minutes (to heat up the chip) before shutting down the computer.

Using bright field microscopy

When using bright field microscopy you can use the camera for imaging only at low laser powers (<10) or until the pixels are saturated, in which case a warning will be given. Normally you do not need to turn on the neither the cooling nor the EM-gain when using bright field microscopy.

Using the cooling

You can cool to -80 degrees at least but for many purposes this is more than actually necessary. However, when you cool you should be aware of the following: First, the camera cools a little faster if you are using it at the same time and if the curtains are open (so that heat can escape). Secondly, when you go to lunch you do not need to take of the cooling but for longer periods it is preferable to turn it of. Again: If cooling wait at least 5 minutes (to heat up the chip) before shutting down the computer.

Using the EM-gain

The EM-gain should in principle only be used with fluorescence and cooling and never with the laser. The reason of this, is first of all that you do not want to saturate the EMCCD pixels and, secondly, you have no interest in amplifying thermal noise. In contrast to the cooling, the EM-gain should be turned off whenever you do not use it.

APPENDIX C

Preparation of DNA and T7 polymerase

C.1 DNA

pLJP1

The plasmid pGEM47 (Promega) carries resistance to ampicillin and a T7 promoter as depicted in figure [C.1](#).

DNA template of activity assays

The DNA is 651 bp \sim 220 nm in length and has a T7 promoter and a digoxigenin labeled end.

For control experiments pGEM-4Z (Promega) was synthesized with this primer, instead of primer 1:

3 25-mer: 5' TAT AGT GTC ACC TAA ATC CAA TTC AC 3'

This DNA template has a digoxigenin labeled end but no T7 promoter. The gel indicated that this is around 100 bp shorter than the first template.

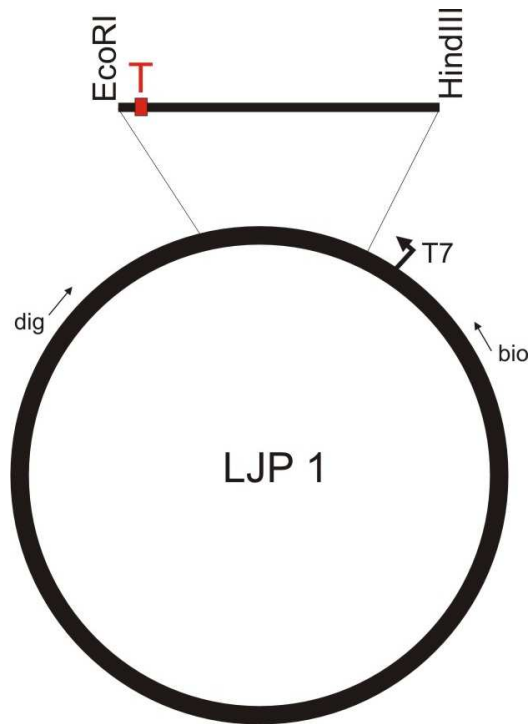


Figure C.1: A sketch of the plasmid pLJP1 constructed in the laboratory of Szabolcs Semsey, ELTE, Budapest. The arrow denotes the T7 promoter sequence and **T** a terminator sequence.

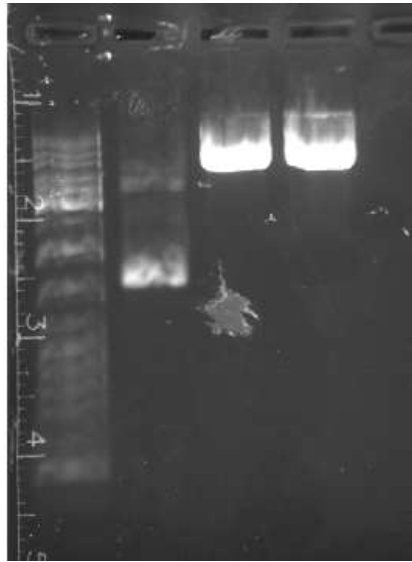


Figure C.2: The final template after sequencing of LJP1. To the far left is the DNA ladder and then 3 different DNA samples where only the two last are good. The length of these corresponds to 4,000 bp.

C.2 *In vivo* biotinylation of T7 polymerase

This system is designed by Szabolcs Semsey and the construction is done with the help of Szabolcs Semsey in his laboratory, ELTE, Budapest. Recently, this was repeated by Mette Eriksen with the help of Jesper Tholstrup and Michael Sørensen. This was carried out in the laboratory of Michael Sørensen, BioCenter, University of Copenhagen.

The overall plan and the procedure

The overall plan is to grow an *E. coli* that carries two different plasmids. The pBM161 plasmid has the T7 gene and the bio-tag the other pBirA has the BirA gene. Szabolcs got the protocol and the parental strain, without the bio-tag, directly from the author of the article. They inserted the bio-tag (a lock-and-key construction) on it and this was checked by a company (Szabolcs send three DNA samples and they were all OK).

Both plasmids and the cells own DNA has the repressor *LacI* operator just upstream of the T7+bio-tag gene and the BirA. This means that the expression of this proteins is inhibited by the binding of the repressor to the operator site. However, IPTG is the inducer of the two genes. IPTG binds to the repressor protein and the transcription from the promoter can be initiated.

The result is that the first sample should not have a high expression of the proteins both the second should.

The insertion of plasmids in the cells

We want an *E. coli* cells expressing the two plasmids. We want the cells to take up the DNA and then plate them on LB media with agar containing ampicillin and chloramphenicol, because each plasmid carries a resistance towards one of these antibiotics. However, their conditions are a little harsh when growing with the two antibiotics, so there may not be so many cells.

The procedure resembles the one of insertion of plasmids in cells described in the DNA protocol. The *E. coli* XL-1 blue are moved from -80 to ice. These cells are the remaining from last so they are all ready incubated with this special ethanol. Likewise, empty tubes are put on ice. We want to prepare to cells solutions, sample 1 with the T7+bio plasmid and the BirA plasmid and sample 2 with the parent T7 plasmid and the BirA plasmid. Both samples are prepared in the following way:

- 26 μ l cells in the cold tube.
- 1 μ l of each plasmids.



Figure C.3: The cells carrying the parental plasmid with the inserted bio-frame and the pBirA.

- 30 minutes incubation on ice.
- Heat shock in 42 degrees heat bath for 45 s.
- 2 minutes on ice.
- Grow for 1/2 an hour with 300 μ l SOC media.
- Spread on 100 μ l on plates with 3 different antibiotics composition; ampicillin, chloramphenicol, and both.
- Incubate overnight at 37 degrees.

We had cells growing on both plates containing both antibiotics (see photo, for the one with the bio-tag).

From these a solution was prepared to grow overnight in LB media containing 80 mg/ml ampicillin (used in the range from 50-100) and 20 mg/ml chloramphenicol (used in the range from 20-30). One or two colonies from each of the plates are grown overnight with about 5 ml of the media, described above.

The collection of two samples

Then 5 ml of overnight culture is grown in 122 ml LB media to log phase (1/2 OD). Then *sample 1* is collected:

- 1 ml is spined down, the supernatant is discarded and the cells are frozen.

Then the rest of the cells are incubated with an IPTG solution. This solution is prepared in the following way:

- 0.4 M in water sterilized by filtering.
- 130 μ l of this is added to the cell solution (so that the final IPTG concentration is 0.4 mM) and incubated in a shaker at 37° C for 4 hours.

The *sample 2* is collected from this in the same manner as above.

- 1 ml is spined down, the supernatant is discarded and the cells are frozen.

When we later repeated this, we changed the procedure a little. We did not want to express the genes from this but just to evaluate whether there T7 polymerases are expressed. First of all we do not extra biotin to biotinylate the protein. Furthermore, we prepared 4 samples from the overnight culture; 2 carrying the plasmid with the T7 gene and the bio-tag and 2 with only the parental plasmid. The solutions are mixed as follows:

- 2 ml LB media containing 80 mg/ml ampicillin and 20 mg/ml chloramphenicol.
- 100 μ l overnight culture.

This is put in a shaker at 37 degrees until log phase.

Purification and denaturation of the proteins

The denaturation cell samples, *sample 1* and *sample 2*, are put is done by two chemicals: SDS disrupts the non-covalent bonds of the protein and the other chemical breaks the covalent bonds.

Anions (e^-) of the chemical binds to the main peptide at a ratio of one amino acid for each two amino acid residues. The electrostatic repulsion causes them to form rods, thereby securing that the conformation of the protein is not a factor of separation in the gel electrophoresis.

Preparations for a protein gel

We want to make a protein gel to clarify whether the T7 polymerase and the BirA protein is expressed. We use a stain of the proteins, merely to localize them. So the samples are mixed with blue stain and boiled for 10 minutes and spined for 5. Then the pellet is thrown away and in the supernatant are the soluble proteins.

We know that the molecular weight of the T7 polymerase is about 100 kDa and that the molecular weight of the BirA is about 35 kDa (www.avidity.com).

C.3 *In vitro* biotinylation of T7 polymerase

This work was done by the visiting researcher Marit Sletmoen, University of Trondheim, with the help of Jesper Tholstrup and Michael Sørensen. This was carried out in the laboratory of Michael Sørensen, BioCenter, University of Copenhagen.

Materials:

- T7 RNA Polymerase R0884 from Sigma-Aldrich. - BiotinTag, Microbiotinylation Kit.
- B-TAG from Sigma-Aldrich. (The kit contained in total 5 vials of reactants and 5 columns. The 3 remaining columns and vials are stored at 4° C in the sample preparation room at NBI).

The procedure suggested by the producers of the kit was followed but some modifications were made as described in the following:

Procedure

The numbering refers to the steps defined in the protein labeling procedure proposed by the producers of the biotinylation kit. Modifications made in each step are described

- 0.1 M sodium phosphate buffer, pH 7.2, was prepared.

Preparation of protein-solution

2 In the protein labeling protocol it is stated that the protein should be dissolved in 0.1 M Phosphate Buffer. The T7 RNA Polymerase provided by Sigma is supplied in a solution of 50% glycerol, 100 mM NaCl, 50 mM Tris-HCl, pH 7.9, 1 mM dithiothreitol, 0.1% w/v TRITON x-100, and 0.1 mM EDTA. Under point 3D, notes, point 1 in the protein labeling procedure proposed by the producers of the biotinylation kit it is stated that "Protein solutions should not be prepared in buffers containing amines such as Tris and glycine, or sodium azide since they inhibit the labeling reaction. If the buffers contain amines or sodium azide, dialyze against 0.1 M sodium phosphate, pH 7.2 or against PBS, pH 7.4." Due to the small volume of the sample (50 μ), dialysis was judged not to be a preferable technique. The buffer of the sample was therefore changed by the use of the column provided in the kit. The protein solution was placed on a prepared column, and eluted with 50 μ l 0.1 M Phosphate Buffer as explained under point 6 below.

- 3 . The content of one vial of BAC-SulfoNHS (B 4430) was dissolved with 30 μ l DMSO. 0.1 M sodium phosphate buffer, pH 7.2 was then added to give a final volume of 1 mL, and vortexed well. The resulting concentration of the BAC-SulfoNHS solution is 5 mg/ml.
- 4 10 μ l of the BAC-SulfoNHS solution was immediately added to the protein solution with gentle stirring.
- 5 The solution was incubated with gentle stirring for 30 min at room temperature.

Preparation of the column:

- 1 1 liter of 0.01 M Phosphate Buffered Saline (PBS) (0.01 M phosphate buffer, 0.138 M NaCl, 2.7 mM KCl, pH 7.4) solution was prepared using a powder package provided in the kit. This serves as equilibration buffer of the microspin G-50 column and for elution of the labeled protein from the column.
- 2 The resin in the column was resuspended by vortexing.
- 3 The cap of the column was loosened and the bottom closure removed.
- 4 The column was placed in a 1.5 mL Eppendorf tube (cap was removed) for support.
- 5 The column was spun for 1 minute at 700 g.
- 6 The column was equilibrated in PBS, pH 7.4: 0.2 mL PBS, pH 7.4 was added to the column. The column was then spun for 1 min at 700 g. The step was repeated once.

Change of buffer of T7-polymerase solution:

The prepared column was used to change the buffer of the T7-polymerase solution. The T7-polymerase solution was added to the column and subsequently 50 μ l phosphate buffer was added. The column was spun for 1 minute at 700 g. The proteins were expected to go through the column and were collected.

A few μ l of the solution expected to contain the proteins were retained for further activity testing.

The same column was used for the protein isolation. Prior to protein isolation the column was cleaned by repeating step 6 three times.

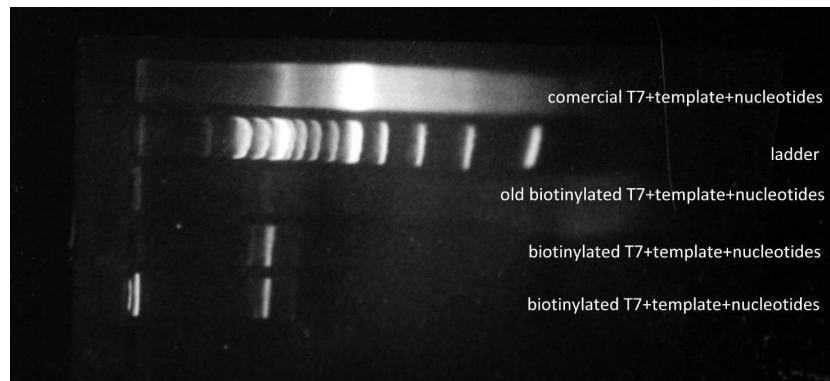


Figure C.4: Results of the gel-electrophoresis where the activity of the biotinylated T7 RNAPs. A clear band from the added DNA (template) is seen, but no bands reflecting the presence of produced RNA are seen. The ladder gives the molecular weight of the diverse bands. The upper lane is a sample containing non-biotinylated T7 RNAP, DNA, and RNA produced by the T7 RNAP. The middle lane shows T7-bio-His6 RNAP (old biotinylated T7). The band contains some short fragments of polymer and the template DNA band is very weak. This leads to the conclusion that the RNAP, at this point, was polluted with a DNA-degrading enzyme.

Isolation of labeled protein:

- 8 Each of four 1.5 mL tubes were numbered 1-4.
- 9 The column was placed in tube number 1 and the biotinylation reaction mixture was added.
- 10 The column was spun for 1 minute at 700 g. This gave fraction 1.
- 11 The column was eluted with PBS, pH 7.4. The column was spun for 1 minute at 700 g. This step was repeated twice more giving tube 2-4.

The fractions containing the protein were not added together but were kept separated, since the amount of activity might be different in the different fractions.

In the samples prepared in February 2009, glycerol was added to give a final concentration of glycerol in the samples equal to 20%. In the samples prepared in April 2009, 100% glycerol was added to the tubes to give a final concentration of glycerol equal to 50%.

Test of the activity of the biotinylated T7-polymerases

The activity of the polymerases were tested in an assay where DNA were added and the amount of RNA produced were determined using gel electrophoresis.

APPENDIX D

Sample preparations

D.1 Optical trapping of quantum dots

Samples

1 μL QDs are diluted to 10^{-5} of the original concentration in QD-buffer. The QDs are stable over many days in this buffer in contrast to water where they tend to agglomerate. One should be aware, however, that the QD solution should be briefly vortexed before each use.

Sample chambers are prepared with a coverslip (# 1 (for $63\times$ objective) or 1.5 (for $100\times$ objective)) and thick glass slide is mounted with double-sticky tape and vacuum grease. This gives a stable chamber.

QD-buffer

50 mM Sodium Borate with % BSA. Adjust pH to 8.2.

Trapping QDs

One should be aware of the following: That the fan of the camera results in a high peak around 100 Hz in one of the horizontal directions but that this is equalized out on the power spectrum. Furthermore, that some of the immersion oils are fluorescent, which results in large background fluorescence and a poor S/N. However, non-fluorescent oils with appropriate refractive indexes are available.

Analysis of the QD images

The signal to noise ration can be calculated be finding the average pixel intensity on a QD and compare it to the average intensity of the surroundings. To enlarge this ratio the sensitivity of the camera or the integration time can be changed. Some points to be aware of when using the EMCCD is shown in section [B.2](#).

Data was analyzed with ImageJ (<http://rsb.info.nih.gov/ij/>) and custom made Matlab routines which are available upon request.

D.2 Stretching DNA

Washed streptavidin beads

- 20 μL Streptavidin-coated beads of 3.1 μm .
- 200 μL washing buffer.

The beads are washed 3 times [164] to remove all streptavidin that is not attached to the beads. The beads are then resuspended in TE-buffer.

Hairy streptavidin beads

- 20 μL 3.1 μm washed streptavidin beads.
- 29 μL TE-buffer.
- 1 μL DNA solution 2

All this is mixed and incubating for 30 min with Lana's knocking-on-the-tube method: knocks on the tube once in a while. Then spin for 5 minutes. Remove supernatant and resuspend in TE-buffer for a final amount of 50 μl .

Anti-digoxigenin beads

These beads are coated as described in Reference [164, 165].

Sample preparation

- 2 μL Anti-digoxigenin-coated beads.
- 1 μL Hairy streptavidin-coated beads.
- 247 μL TE-buffer with α -casein.

In a simple flow chamber tethers are produced and a force-extension series is measured. The flow chambers are produced as described in [143] and pipettes are pulled with *step1* and *heater2* put to 60. The sample solution changes for every new stock of anti-digoxigenin coated beads.

D.3 Activity of T7 polymerase attached with quantum dots

These sample solutions are inspired by Reference [131] and it is important to use purified water that is both DNase and RNase free.

TE buffer, pH 8.0

10 mM Tris-HCl
1 mM EDTA

TE buffer with α -casein or BSA

TE buffer with 2 mg/ml α -casein (Sigma) or BSA.

RNAP reaction buffer, pH 7.9

40 mM Tris-HCl
6 mM MgCl₂
10 mM DTT

Surface-blocking solution

RNAP reaction buffer with 2 mg/ml α -casein (Sigma) or BSA.

4× RNAP reaction buffer:

100-200 nM RNAP.
100 μ g/ml BSA.
0.1-0.6 mM NTP.

Protein solution:

0.5 μ l of each nucleotide.
0.5 μ l QDs (0.5 μ l in 1000 μ l water, filtered).
2.5 μ l 4× RNAP reaction buffer.
5 μ l proteins.

Protocol

20 μ l	20 μ g/ml anti-digoxigenin solution in PBS	Incubated > 1 hour.
20 μ l	TE buffer with α -casein	Incubated > 30 min.
10 μ l	0.1 nM DNA in TE buffer	Incubated > 5 min.
20 μ l	Surface-blocking solution	Incubated > 30 min.
10 μ l	Protein solution	Sealed with vacuum grease.

D.4 Tethered particle method with quantum dots

TE buffer, pH 8.0

10 mM Tris-HCl
1 mM EDTA

TE buffer with α casein

TE buffer with 2 mg/ml α -casein (Sigma).

RNAP reaction buffer, pH 7.9

40 mM Tris-HCl
6 mM MgCl₂
10 mM DTT

Surface-blocking solution

RNAP reaction buffer with 2 mg/ml α -casein (Sigma).

Protocol

Flow chambers are assembled with to cover slides and a layer of para-film.

20 μ l	20 μ g/ml anti-digoxigenin solution in PBS	Incubated > 1 hour.
20 μ l	TE buffer with α -casein	Incubated > 30 min.
10 μ l	0.1 nM DNA in TE buffer	Incubated > 5 min or more.
20 μ l	10 ⁻³ QDs in TE buffer with α -casein	Incubated > 10 min.
20 μ l	Flush 3 \times with TE buffer with α -casein	Sealed with vacuum grease.

Bibliography

- [1] Nelson, D. L. & Cox, M. M. *Principles of Biochemistry* (W. H. Freeman and Co., 2005).
- [2] Sneppen, K. & Zocchi, G. *Physics In Molecular Biology* (Cambridge Uni Press (CUP), 2005).
- [3] Hansen, T. M., Reihani, N., Oddershede, L. & Sørensen, M. A. Correlation between mechanical strength of messenger RNA pseudoknots and ribosomal frameshifting. *Proc. Nat. Acad. Science* **104**, 5830–5835 (2007).
- [4] Hallatschek, O., Hersen, P., Ramanathan, S. & Nelson, D. R. Genetic drift at expanding frontiers promotes gene segregation. *Proc. Nat. Acad. Science* **104**, 19926–19930 (2007).
- [5] Lopez, P., Guillerez, J., Sousa, R. & Dreyfus, M. The low processivity of T7 RNA polymerase over the initially transcribed sequence can limit productive initiation in vivo. *J. Mol. Biol.* **269**, 41–51 (1997).
- [6] Ikeda, R. & Richardson, C. Interactions of the RNA-polymerase of bacteriophage-T7 with its promoter during binding and initiation of transcription. *Proc. Nat. Acad. Science* **83**, 3614–3618 (1986).
- [7] Place, C., Oddos, J., Buc, H., McAllister, W. & Buckle, M. Studies of contacts between T7 RNA polymerase and its promoter reveal features in common with multisubunit RNA polymerases. *Biochem.* **38**, 4948–4957 (1999).
- [8] Skinner, G., Baumann, C., Quinn, D., Molloy, J. & Hoggett, J. Promoter binding, initiation, and elongation by bacteriophage T7 RNA polymerase - A single-molecule view of the transcription cycle. *J. Biol. Chem.* **279**, 3239–3244 (2004).

- [9] Harada, Y. *et al.* Single-molecule imaging of RNA polymerase-DNA interactions in real time. *Biophys. J.* **76**, 709–715 (1999).
- [10] Guajardo, R., Lopez, P., Dreyfus, M. & Sousa, R. NTP concentration effects on initial transcription by T7 RNAP indicate that translocation occurs through passive sliding and reveal that divergent promoters have distinct NTP concentration requirements for productive initiation. *J. Mol. Biol.* **281**, 777–792 (1998).
- [11] Yin, H. *et al.* Transcription against an applied force. *Science* **270**, 1653–1657 (1995).
- [12] Wuite, G., Smith, S., Young, M., Keller, D. & Bustamante, C. Single-molecule studies of the effect of template tension on T7 DNA polymerase activity. *Nature* **404**, 103–106 (2000).
- [13] Forde, N., Izhaky, D., Woodcock, G., Wuite, G. & Bustamante, C. Using mechanical force to probe the mechanism of pausing and arrest during continuous elongation by *Escherichia coli* RNA polymerase. *Proc. Nat. Acad. Science* **99**, 11682–11687 (2002).
- [14] Dalal, R. V. *et al.* Pulling on the nascent RNA during transcription does not alter kinetics of elongation or ubiquitous pausing. *Mol. Cell* **23**, 231–239 (2006).
- [15] Landick, R. Active-site dynamics in RNA polymerases. *Cell* **116**, 351–353 (2004).
- [16] Steitz, T. & Yin, Y. Transition of T7 RNA polymerase from transcription initiation to elongation and its functioning as a molecular motor. *Biophys. J.* **86**, 330A (2004).
- [17] Abbondanzieri, E. A., Greenleaf, W. J., Shaevitz, J. W., Landick, R. & Block, S. M. Direct observation of base-pair stepping by RNA polymerase. *Nature* **438**, 460 – 465 (2005).
- [18] Bai, L., Shundrovsky, A. & Wang, M. Sequence-dependent kinetic model for transcription elongation by RNA polymerase. *J. of Mol. Bio* **344**, 335–349 (2004).
- [19] Guajardo, R. & Sousa, R. A model for the mechanism of polymerase translocation. *J. Mol Biol.* **265**, 8–19 (1997).

- [20] Thomen, P., Lopez, P. & Heslot, F. Unravelling the mechanism of RNA-polymerase forward motion by using mechanical force. *Phys. Rev. Lett.* **94** (2005).
- [21] Shaevitz, J. W., Abbondanzieri, E. A., Landick, R. & Block, S. M. Backtracking by single RNA polymerase molecules observed at near-base-pair resolution. *Nature* **426**, 684–687 (2003).
- [22] Izhaky, D., Forde, N., Woodcock, G., Wuite, G. & Bustamante, C. Single-molecule studies of the dynamics of *E. coli* RNA polymerase. *Biophys. J.* **82**, 245 (2002).
- [23] Davenport, R., Wuite, G., Landick, R. & Bustamante, C. Single-molecule study of transcriptional pausing and arrest by *Escherichia coli* RNA polymerase. *Science* **287**, 2497–2500 (2000).
- [24] Herbert, K. *et al.* Sequence-resolved detection of pausing by single RNA polymerase molecules. *Cell* **125**, 1083–1094 (2006).
- [25] Shundrovsky, A., Santangelo, T., Roberts, J. & Wang, M. A single-molecule technique to study sequence-dependent transcription pausing. *Biophys. J.* **87**, 3945–3953 (2004).
- [26] Galburt, E. A. *et al.* Backtracking determines the force sensitivity of RNAP II in a factor-dependent manner. *Nature* **446**, 820–823 (2007).
- [27] Wang, M. *et al.* Force and velocity measured for single molecules of RNA polymerase. *Science* **282**, 902–907 (1998).
- [28] Larson, M. H., Greenleaf, W. J., Landick, R. & Block, S. M. Applied force reveals mechanistic and energetic details of transcription termination. *Cell* **132**, 971–982 (2008).
- [29] Ashkin, A. Acceleration and trapping of particles by radiation pressure. *Phys. Rev. Lett.* **24**, 156–159 (1970).
- [30] Ashkin, A. & Dziedzic, J. M. Observation of radiation-pressure trapping by particles by alternating light beams. *Phys. Rev. Lett.* **54**, 1245–1248 (1985).
- [31] Svoboda, K. & Block, S. M. Biological applications of optical forces. *Ann. Rev.* **23** (1994).
- [32] Lang, M. J. & Block, S. M. Lbot-1: Laser-based optical tweezers. *Am. J. Phys.* **71**, 201–215 (2003).

- [33] Neuman, K. C. & Block, S. M. Optical trapping. *Rev. Sci. Instrum.* **75**, 2787–2809 (2004).
- [34] Yin, H., Landick, R. & Gelles, J. Tethered particle motion method for studying transcript elongation by a single RNA polymerase molecule. *Biophys. J.* **67**, 2468–2478 (1994).
- [35] Neuman, K. C., Chadd, E. H., Liou, G. F., Bergman, K. & Block, S. M. Characterization of photodamage to *Escherichia coli* in optical traps. *Biophys. J.* **77**, 2856–2863 (1999).
- [36] Rasmussen, M. B., Oddershede, L. B. & Siegumfeldt, H. Optical tweezers cause physiological damage to *Escherichia coli* and *Listeria bacteria*. *Appl. Environ. Microbiol.* **74**, 2441–2446 (2008).
- [37] Tolic-Nørrelykke, I., Munteanu, E., Thon, G., Oddershede, L. & Berg-Sørensen, K. Anomalous diffusion in living yeast cells. *Phys. Rev. Lett.* **93** (2004).
- [38] Selhuber-Unkel, C., Yde, P., Berg-Sørensen, K. & Oddershede, L. B. Variety in intracellular diffusion during the cell cycle. *Phys. Biol.* **6** (2009).
- [39] Ashkin, A. & Dziedzic, J. Internal cell manipulation using infrared-laser traps. *Proc. Nat. Acad. Science* **86**, 7914–7918 (1989).
- [40] Fischer, M., Richardson, A. C., Reihani, S. N. S., Oddershede, L. B. & Berg-Sørensen, K. Active-passive calibration of optical tweezers in viscoelastic media. *Rev. Sci. Instrum.* **81** (2010).
- [41] Born, M. & Wolf, E. *Principles of Optics* (Cambridge Uni Press, 2003).
- [42] Michalet, X. *et al.* Properties of fluorescent semiconductor nanocrystals and their application to biological labeling. *Single mol.* **2**, 261–276 (2001).
- [43] Dubertret, B. *et al.* In vivo imaging of quantum dots encapsulated in phospholipid micelles. *Science* **298**, 1759–1762 (2002).
- [44] Marder, M. P. *Condensed Matter Physics* (John Wiley and Sons, 2000).
- [45] Pelton, M., Smith, G., Scherer, N. F. & Marcus, R. A. Evidence for a diffusion-controlled mechanism for fluorescence blinking of colloidal quantum dots. *Proc. Nat. Acad. Science* **104**, 14249–14254 (2007).

- [46] Michalet, X. *et al.* Quantum dots for live cells, in vivo imaging, and diagnostics. *Science* **307**, 538–544 (2005).
- [47] Christensen, E. A. & Lagerholm, C. Applications of quantum dots for single molecule imaging in cells and substrate-supported planar membranes. Scientific poster: <http://www.arnspang.dk/London.pdf>.
- [48] Chan, W. C. W. & Nie, S. M. Quantum dot bioconjugates for ultrasensitive nonisotopic detection. *Science* **281**, 2016–2018 (1998).
- [49] Larson, D. *et al.* Water-soluble quantum dots for multiphoton fluorescence imaging in vivo. *Science* **300**, 1434–1436 (2003).
- [50] Dahan, M. *et al.* Diffusion dynamics of glycine receptors revealed by single quantum dot tracking. *Science* **302**, 442–445 (2003).
- [51] Ballou, B., Lagerholm, B., Ernst, L., Bruchez, M. & Waggoner, A. Noninvasive imaging of quantum dots in mice. *Bioconjugate Chem.* **15**, 79–86 (2004).
- [52] Krishna, S., Semsey, S. & Sneppen, K. Combinatorics of feedback in cellular uptake and metabolism of small molecules. *Proc. Nat. Acad. Science* **104**, 20815–20819 (2007).
- [53] Babu, M. & Teichmann, S. Evolution of transcription factors and the gene regulatory network in *Escherichia coli*. *Nucl. Acids Res.* **31**, 1234–1244 (2003).
- [54] Pyles, E. & Lee, J. Mode of selectivity in cyclic AMP receptor protein-dependent promoters in *Escherichia coli*. *Biochem.* **35**, 1162–1172 (1996).
- [55] Santillan, M. & Mackey, M. Influence of catabolite repression and inducer exclusion on the bistable behavior of the *lac* operon. *Biophys. J.* **86**, 1282–1292 (2004).
- [56] Muller-Hill, B. The function of auxiliary operators. *Mol. Microbiol.* **29**, 13–18 (1998).
- [57] Abo, T., Inada, T., Ogawa, A. & Aiba, H. SsrA-mediated tagging and proteolysis of LacI and its role in the regulation of *lac* operon. *EMBO J.* **19**, 3762–3769 (2000).

- [58] Semsey, S., Krishna, S., Sneppen, K. & Adhya, S. Signal integration in the galactose network of *Escherichia coli*. *Mol. Microbiol.* **65**, 465–476 (2007).
- [59] Jacob, F. & Monod, J. Genetic regulatory mechanisms in synthesis of proteins. *J. Mol. Biol.* **3**, 318–& (1961).
- [60] Sellitti, M., Pavco, P. & Steege, D. *Lac* repressor blocks *in vivo* transcription of *lac* control region DNA. *Proc. Nat. Acad. Science* **84**, 3199–3203 (1987).
- [61] Wong, P., Gladney, S. & Keasling, J. Mathematical model of the *lac* operon: Inducer exclusion, catabolite repression, and diauxic growth on glucose and lactose. *Biotechnol. Prog.* **13**, 132–143 (1997).
- [62] Vilar, J., Guet, C. & Leibler, S. Modeling network dynamics: the *lac* operon, a case study. *J. Cell Biol.* **161**, 471–476 (2003).
- [63] Ozbudak, E., Thattai, M., Lim, H., Shraiman, B. & van Oudenaarden, A. Multistability in the lactose utilization network of *Escherichia coli*. *Nature* **427**, 737–740 (2004).
- [64] van Hoek, M. & Hogeweg, P. The effect of stochasticity on the *lac* operon: An evolutionary perspective. *PLOS Comput. Biol.* **3**, 1071–1082 (2007).
- [65] Rosenfeld, N., Elowitz, M. & Alon, U. Negative autoregulation speeds the response times of transcription networks. *J. Mol. Biol.* **323**, 785–793 (2002).
- [66] Jauffred, L. *et al.* Modelling the auto-regulation in the *lac* operon. *XXX XX*, XX–XX (XXX).
- [67] Kalisky, T., Dekel, E. & Alon, U. Cost-benefit theory and optimal design of gene regulation functions. *Phys. Biol.* **4**, 229–245 (2007).
- [68] Yildirim, N. & Mackey, M. Feedback regulation in the lactose operon: A mathematical modeling study and comparison with experimental data. *Biophys. J.* **84**, 2841–2851 (2003).
- [69] Ackers, G., Johnson, A. & Shea, M. Quantitative model for gene-regulation by lambda-phage repressor. *Proc. Nat. Acad. Science* **79**, 1129–1133 (1982).

- [70] Gillespie, D. Exact stochastic simulation of coupled chemical-reactions. *J. Phys. Chem.* **81**, 2340–2361 (1977).
- [71] Mandelstam, J. Turnover of protein in starved bacteria and its relationship to the induced synthesis of enzyme. *Nature* **179**, 1179–1181 (1957).
- [72] Jobe, A. & Bourgeoi, S. *Lac* repressor-operator interaction .6. natural inducer of lac operon. *J. Mol. Biol.* **69**, 397–& (1972).
- [73] Hippel, P., Revzin, A., Gross, C. & Wang, A. Nonspecific DNA binding of genome regulating proteins as a biological-control mechanism .1. *Lac* operon - equilibrium aspects. *Proc. Nat. Acad. Science* **71**, 4808–4812 (1974).
- [74] Santillan, M. Bistable behavior in a model of the *lac* operon in *Escherichia coli* with variable growth rate. *Biophys. J.* **94**, 2065–2081 (2008).
- [75] Gilbert, W. & Mullerhi, B. Isolation of *lac* repressor. *Proc. Nat. Acad. Science* **56**, 1891–& (1966).
- [76] Strogatz, S. H. *Nonlinear dynamics and Chaos* (Addisn-Wesley Publishing, 1994).
- [77] Gordon, A. J. E. *et al.* Transcriptional infidelity promotes heritable phenotypic change in a bistable gene network. *PLOS Biol.* **7**, 364–370 (2009).
- [78] Stephan, J. *Optische Überauflösung durch strukturierte Beleuchtung mittels Interferenz evaneszenter Wellen.* Master's thesis, Albert-Ludwigs-Universität, Freiburg (2008).
- [79] Chung, E., Kim, D. & So, P. T. C. Extended resolution wide-field optical imaging: objective-launched standing-wave total internal reflection fluorescence microscopy. *Opt. Lett.* **31**, 945–947 (2006).
- [80] Chung, E., Kim, D., Cui, Y., Kim, Y.-H. & So, P. T. C. Two-dimensional standing wave total internal reflection fluorescence microscopy: Superresolution imaging of single molecular and biological specimens. *Biophys. J.* **93**, 1747–1757 (2007).
- [81] Gustafsson, M. G. L. Surpassing the lateral resolution limit by a factor of two using structured illumination microscopy. *J. Microsc.* **198**, 82–87 (2000).

- [82] Shao, L. *et al.* I5s: Wide-field light microscopy with 100-nm-scale resolution in three dimensions. *Biophys. J.* **94**, 4971–4983 (2008).
- [83] Rohrbach, A. *Optische Anregung und Detektion biologischer Fluoreszenzobjecte hinter dielektrischen Grenzflächen.* Ph.D. thesis, Ruprecht-Karls-Universität, Heidelberg (1998).
- [84] Čižmár, T., Garcés-Chávez, V., Dholakia, K. & Zemánek, P. Optical conveyor belt for delivery of submicron objects. *Appl. Phys. Lett.* **86** (2005).
- [85] Jakl, P., Cizmar, T., Sery, M. & Zemanek, P. Static optical sorting in a laser interference field. *Appl. Phys. Lett.* **92** (2008).
- [86] Karasek, V. *et al.* Long-range one-dimensional longitudinal optical binding. *Phys Rev. Lett.* **101** (2008).
- [87] Rohrbach, A. & Stelzer, E. H. K. Optical trapping of dielectric particles in arbitrary fields. *J. Opt. Soc. Am. A* **18**, 839–853 (2001).
- [88] Rohrbach, A., Kress, H. & Stelzer, E. H. K. Reply to comment on 'trapping force, force constant, and potential depths for dielectric spheres in the presence of spherical aberrations'. *Appl. Opt.* **43**, 1827–1829 (2004).
- [89] Rohrbach, A. Stiffness of optical traps: Quantitative agreement between experiment and electromagnetic theory. *Phys. Rev. Lett.* **95**, 168102 (2005).
- [90] Hulst, H. C. V. D. *Light Scattering by Small Particles* (Dover Publications Inc, 1957).
- [91] Einstein, A. The motion of elements suspended in static liquids as claimed in the molecular kinetic theory of heat. *Ann. Physik* **17**, 549–560 (1905).
- [92] Dienerowitz, M., Mazilu, M. & Dholakia, K. Optical manipulation of nanoparticles: a review. *J Nanophotonic.* **2** (2008).
- [93] Bosanac, L., Aabo, T., Bendix, P. M. & Oddershede, L. B. Efficient optical trapping and visualization of silver nanoparticles. *Nano Lett.* **8**, 1486–1491 (2008).
- [94] Hansen, P. M., Bhatia, V. K., Harrit, N. & Oddershede, L. Expanding the optical trapping range of gold nanoparticles. *Nano Lett.* **5**, 1937–42 (2005).

- [95] Hajizadeh, F. & Reihani, S. N. S. Optimized optical trapping of gold nanoparticles. *Opt. Express* **18**, 551–559 (2010).
- [96] Selhuber-Unkel, C., Schubert, I. Z. O., Sönnichsen, C. & Oddershede, L. B. Quantitative optical trapping of single gold nanorods. *Nano Lett.* **8**, 2998–3003 (2008).
- [97] van der Horst, A. *et al.* Manipulating metal-oxide nanowires using counter-propagating optical line tweezers. *Opt. Express* **15**, 11629–11639 (2007).
- [98] Pan, L., Ishikawa, A. & Tamai, N. Detection of optical trapping of CdTe quantum dots by two-photon-induced luminescence. *Phys. Rev. B* **75**, 161305 (2007).
- [99] Oddershede, L., Greco, S., Nørrelykke, S. F. & Berg-Sørensen, K. Optical tweezers: a probe for biological surfaces. *Probe Microsc.* **2**, 129–137 (2001).
- [100] Hansen, P. M. *Cellular mechanics studied by novel nano-tools and reconstituted model systems*. Ph.D. thesis, The Niels Bohr Institute, University of Copenhagen (2006).
- [101] Richardson, A. *Development of optical trapping techniques for in vivo investigations*. Ph.D. thesis, The Niels Bohr Institute, University of Copenhagen (2008).
- [102] Berg-Sørensen, K., Oddershede, L., Florin, E.-L. & Flyvbjerg, H. Unintended filtering in a photodiode detection system for optical tweezers. *J. Appl. Phys.* **96**, 3167–3176 (2003).
- [103] Jauffred, L. *An investigation of elastic bacterial tethers with optical tweezers*. Master's thesis, The Niels Bohr Institute, University of Copenhagen (2006).
- [104] Svoboda, K. & Block, S. M. Optical trapping of metallic Rayleigh particles. *Opt. Lett.* **19**, 930–932 (1994).
- [105] Reihani, S. N. S. & Oddershede, L. B. Optimizing immersion media refractive index improves optical trapping by compensating spherical aberrations. *Opt. Lett.* **32**, 1998–2000 (2007).
- [106] Jauffred, L., Richardson, A. C. & Oddershede, L. B. Three-dimensional optical control of individual quantum dots. *Nano Lett.* **8**, 3376 – 3380 (2008).

- [107] Lagerholm, B. C., Averett, L., Weinreb, G. E., Jacobson, K. & Thompson, N. L. Analysis method for measuring submicroscopic distances with blinking quantum dots. *Biophys. J.* **91**, 3050–3060 (2006).
- [108] Hansen, P. M., Tolic-Nørrelykke, I. M., Flyvbjerg, H. & Berg-Sørensen, K. tweezercalib 2.0: Faster version of matlab package for precise calibration of optical tweezers. *Comp. Phys. Commun.* **174**, 518–520 (2006).
- [109] Segelstein, D. J. *The complex refractive index of water*. Master's thesis, University of Missouri-Kansas City (1981).
- [110] Sheik-Bahae, M., Hutchings, D., Hagan, D. & Stryland, E. V. Dispersion of bound electronic nonlinear refraction in solids. *IEEE Journ. of Quantum Electr.* **27**, 1296 – 1309 (1991).
- [111] Kraus, M. Personal communication about quantum dot sizes. Tech. Rep., Invitrogen (2008).
- [112] Jauffred, L. & Oddershede, L. Two-photon quantum dot excitation during optical trapping. *Nano Lett.* **10**, 1927–1930 (2010).
- [113] Wang, Y. M., Austin, R. H. & Cox, E. C. Single molecule measurements of repressor protein 1D diffusion on DNA. *Phys. Rev. Lett.* **97**, 048302 (2006).
- [114] Blanton, S., Dehestani, A., Lin, P. & Guyot-Sionnest, P. Photoluminescence of single semiconductor nanocrystallites by two-photon excitation microscopy. *Chem. Phys. Lett.* **229**, 317–322 (1994).
- [115] Schmidt, M., Blanton, S., Hines, M. & Guyot-Sionnest, P. Size-dependent two-photon excitation spectroscopy of CdSe nanocrystals. *Phys. Rev. B* **19**, 12629 (1996).
- [116] Pu, S.-C. *et al.* The empirical correlation between size and two-photon absorption cross section of CdSe and CdTe quantum dots. *Small* **2**, 308–313 (2006).
- [117] Wang, T. *et al.* Thiol-capped CdTe quantum dots with two-photon excitation for imaging high autofluorescence background living cells. *J. Fluoresc.* **19**, 615–621 (2009).
- [118] Boyd, R. *Nonlinear Optics* (Academic Press, 2003).

- [119] Gerdova, I. & Haché, A. Third-order non-linear spectroscopy of CdSe and CdSe/ZnS core shell quantum dots. *Opt. Commun.* **246**, 205–212 (2005).
- [120] M Capitano, F. V., D Maggi & Pavone, F. S. FIONA in the trap: the advantages of combining optical tweezers and fluorescence. *J. Opt. A: Pure Appl. Opt.* **9**, S157–S163 (2007).
- [121] Tokunaga, M., Imamoto, N. & Sakata-Sogawa, K. Highly inclined thin illumination enables clear single-molecule imaging in cells. *Nature Meth.* **5**, 159–161 (2008).
- [122] Schafer, D., Gelles, J., Sheetz, M. & Landick, R. Transcription by single molecules of RNA-polymerase observed by light-microscopy. *Nature* **352**, 444–448 (1991).
- [123] Wen, J.-D. *et al.* Following translation by single ribosomes one codon at a time. *Nature* **452**, 598–U2 (2008).
- [124] Allemand, J., Bensimon, D., Jullien, L., Bensimon, A. & Croquette, V. pH-dependent specific binding and combing of DNA. *Biophys. J* **73**, 2064–2070 (1997).
- [125] Michalet, X. *et al.* Dynamic molecular combing: Stretching the whole human genome for high-resolution studies. *Science* **277**, 1518–1523 (1997).
- [126] Arai, Y. *et al.* Tying a molecular knot with optical tweezers. *Nature* **399**, 446–448 (1999).
- [127] Lang, M., Fordyce, P., Engh, A., Neuman, K. & Block, S. Combined fluorescence & force microscopy. *Biophys. J.* **84**, 301A (2003).
- [128] Miyata, H. *et al.* Mechanical measurements of single actomyosin motor force. *Biophys. J.* **68**, S286–S290 (1995).
- [129] Ishijima, A. *et al.* Simultaneous observation of individual ATPase and mechanical events by a single myosin molecule during interaction with actin. *Cell* **92**, 161–171 (1998).
- [130] Lang, M., Fordyce, P., Engh, A., Neuman, K. & Block, S. Simultaneous, coincident optical trapping and single-molecule fluorescence. *Nature Meth.* **1**, 133–139 (2004).

- [131] Kim, J. H. & Larson, R. G. Single-molecule analysis of 1D diffusion and transcription elongation of T7 RNA polymerase along individual stretched DNA molecules. *Nucl. Acids Res.* **35**, 3848–3858 (2007).
- [132] van Dijk, M., Kapitein, L., van Mameren, J., Schmidt, C. & Peterman, E. Combining optical trapping and single-molecule fluorescence spectroscopy: Enhanced photobleaching of fluorophores. *J. Phys. Chem. B* **108**, 6479–6484 (2004).
- [133] Biebricher, A., Wende, W., Escude, C., Pingoud, A. & Desbiolles, P. Tracking of single quantum dot labeled EcoRV sliding along DNA manipulated by double optical tweezers. *Biophys. J.* **96**, L50–L52 (2009).
- [134] Shearwin, K., Callen, B. & Egan, J. Transcriptional interference - a crash course. *Trends Genet.* **21**, 339–345 (2005).
- [135] Crampton, N., Bonass, W. A., Kirkham, J., Rivetti, C. & Thomson, N. H. Collision events between RNA polymerases in convergent transcription studied by atomic force microscopy. *Nucl. Acids Res.* **34**, 5416–5425 (2006).
- [136] Callen, B., Shearwin, K. & Egan, J. Transcriptional interference between convergent promoters caused by elongation over the promoter. *Mol. Cell* **14**, 647–656 (2004).
- [137] Hongay, C. F., Grisafi, P. L., Galitski, T. & Fink, G. R. Antisense transcription controls cell fate in *Saccharomyces cerevisiae*. *Cell* **127**, 735–745 (2006).
- [138] Zhou, Y. & Martin, C. T. Observed instability of T7 RNA polymerase elongation complexes can be dominated by collision-induced “bumping”. *J. Bio. Chem.* **281**, 24441–24448 (2006).
- [139] Prescott, E. M. & Proudfoot, N. J. Transcriptional collision between convergent genes in budding yeast. *Proc. Nat. Acad. Science* **99**, 8796–8801 (2002).
- [140] Liu, B. & Alberts, B. Head-on collision between a DNA-replication apparatus and RNA-polymerase transcription complex. *Science* **267**, 1131–1137 (1995).
- [141] Sneppen, K. *et al.* A mathematical model for transcriptional interference by RNA polymerase traffic in *Escherichia coli*. *J. Mol. Biol.* **346**, 399–409 (2005).

- [142] Thomen, P. *et al.* T7 RNA polymerase studied by force measurements varying cofactor concentration. *Biophys. J.* **95**, 2423–2433 (2008).
- [143] Trpcevski, D. *Optical Stretching of DNA as a Diagnostic Tool in Nanotoxicology*. Master's thesis, The Niels Bohr Institute, University of Copenhagen (2006).
- [144] Jauffred, L., Callisen, T. H. & Oddershede, L. B. Visco-elastic membrane tethers extracted from *Escherichia coli* by optical tweezers. *Biophys. J.* **93**, 4068–4075 (2007).
- [145] Boal, D. *Mechanics of the Cell* (Cambridge University Press, 2002), 1 edn.
- [146] Durniak, K. J., Bailey, S. & Steitz, T. A. The structure of a transcribing T7 RNA polymerase in transition from initiation to elongation. *Science* **322**, 553–557 (2008).
- [147] Yin, Y. & Steitz, T. The structural mechanism of translocation and helicase activity in T7 RNA polymerase. *Cell* **116**, 393–404 (2004).
- [148] Steitz, T. The structural basis of the transition from initiation to elongation phases of transcription, as well as translocation and strand separation, by T7 RNA polymerase. *Curr. Op. Struct. Biol.* **14**, 4–9 (2004).
- [149] Cheetham, G., Jeruzalmi, D. & Steitz, T. Structural basis for initiation of transcription from an RNA polymerase-promoter complex (vol 399, pg 80, 1999). *Nature* **400**, 89 (1999).
- [150] Cheetham, G., Jeruzalmi, D. & Steitz, T. Transcription regulation, initiation, and “DNA scrunching” by T7 RNA polymerase. *Cold Spring Harbor Symp. Quantitative Biol.* **63**, 263–267 (1998).
- [151] Cheetham, G., Jeruzalmi, D. & Steitz, T. Structural basis for initiation of transcription from an RNA polymerase-promoter complex. *Nature* **399**, 80–83 (1999).
- [152] Cheetham, G. & Steitz, T. Insights into transcription: structure and function of single-subunit DNA-dependent RNA polymerases. *Curr. Opinion Struct. Biol.* **10**, 117–123 (2000).
- [153] Cheetham, G. & Steitz, T. Structure of a transcribing T7 RNA polymerase initiation complex. *Science* **286**, 2305–2309 (1999).

- [154] Ebenstein, Y. *et al.* Lighting up individual DNA binding proteins with quantum dots. *Nano Lett.* **9**, 1598–1603 (2009).
- [155] Eriksen, M. *T7 phage RNA polymerase -Oprensning, aktivitetstest og koncentrationsbestemmelse* (2010).
- [156] He, B. *et al.* Rapid mutagenesis and purification of phage RNA polymerases. *Protein Expres. and Purif.* **9**, 142–151 (1997).
- [157] Segall, D., Nelson, P. & Phillips, R. Volume-exclusion effects in tethered-particle experiments: Bead size matters. *Phys. Rev. Lett.* **96** (2006).
- [158] Nelson, P. C. *et al.* Tethered particle motion as a diagnostic of DNA tether length. *J. Phys. Chem. B* **110**, 17260–17267 (2006).
- [159] Beausang, J. F. *et al.* DNA looping kinetics analyzed using diffusive hidden Markov model. *Biophys. J.* **92**, L64–L66 (2007).
- [160] Han, L. *et al.* *Mathematics of DNA Structure, Function and Interactions, Chapter: Calibration of Tethered Particle Motion Experiments* (Springer New York, 2009).
- [161] Sage, D., Neumann, F., Hediger, F., Gasser, S. & Unser, M. Automatic tracking of individual fluorescence particles: Application to the study of chromosome dynamics. *IEEE Transac. Image Proc.* **14**, 1372–1383 (2005).
- [162] Czerwinski, F., Richardson, A. C. & Oddershede, L. B. Quantifying noise in optical tweezers by Allan variance. *Opt. Express* **17**, 13255–13269 (2009).
- [163] Block, S. M. *Cells: A Laboratory Manual*, vol. 3 (Cold Spring Harbor Laboratory Press, 1997).
- [164] Salomo, M. *et al.* The elastic properties of single double-stranded DNA chains of different lengths as measured with optical tweezers. *Colloid. Polym. Phys.* **284**, 1325–1331 (2006).
- [165] Salomo, M. *et al.* Kinetics of TmHU binding to DNA as observed by optical tweezers. *Microsc. Res. Tech.* **70**, 938–943 (2007).